Die approbierte Originalversion dieser Dissertation ist in der Hauptbibliothek der Technischen Universität Wien aufgestellt und zugänglich.
http://www.ub.tuwien.ac.at

The approved original version of this thesis is available at the main library of the Vienna University of Technology.
http://www.ub.tuwien.ac.at/eng

TECHNISCHE UNIVERSITÄT WIEN
Vienna University of Technology

INSTITUT FÜR MECHANIK UND MECHATRONIK
Mechanics & Mechatronics

Dissertation

Model predictive control for an insulated cool box with redundant refrigeration circuits

ausgeführt zum Zwecke der Erlangung des akademischen Grades
eines Doktors der technischen Wissenschaften
eingereicht an der Technischen Universität Wien,
Fakultät für Maschinenwesen und Betriebswissenschaften

von

Dipl.-Ing. Elisabeth Luchini
Matr.Nr.: 0801304

unter der Leitung von

Univ.Prof. Dipl.-Ing. Dr.techn. Stefan Jakubek
Institut für Mechanik und Mechatronik
Abteilung für Regelungstechnik und Prozessautomatisierung

begutachtet von

Ao.Univ.Prof. DI Dr.techn. Martin Kozek
Institut für Mechanik und Mechatronik

Univ.Prof. DI Dr.techn. René Hofmann
Institut für Energietechnik und Thermodynamik

Ich bin immer noch verwirrt,
aber auf einem höheren Niveau.
E. Fermi

Danksagung

Diese Dissertation entstand während meiner Anstellung als Projektassistentin an der TU Wien am Institut für Mechanik und Mechatronik, Abteilung für Regelungstechnik und Prozessautomatisierung in Zusammenarbeit mit der Firma Liebherr-Transportation Systems GmbH & Co KG, Korneuburg.

An erster Stelle möchte ich mich bei meinem Mitbetreuer Martin Kozek, welcher mir während meiner Zeit als Doktorandin immer mit Ratschlägen zur Seite gestanden ist, bedanken. Durch die intensive Zusammenarbeit der letzten vier Jahre durfte ich sehr viel von ihm lernen. Auch abseits wissenschaftlicher Themen hat er stets ein offenes Ohr, hilfreiche Tipps und spannende Erzählungen, welche diese Zeit für mich zu einer ganz besonderen gemacht hat, an die ich immer positiv und mit einem Lächeln im Gesicht zurückdenken werde.

Mein Dank gilt auch meinem Hauptbetreuer Prof. Stefan Jakubek der mir ebenfalls mit seiner fachlichen Unterstützung und begeisternden Art ermöglicht hat die Inhalte dieser Arbeit mit Freude und Motivation zu erstellen.

Auch dem Projektparnter soll hier gedankt werden. Durch die Firma Liebherr konnte diese Arbeit erst zustande kommen. Insbesonderen bei den Kollegen vom LVF-CV Team, welche sich immer Zeit genommen haben und mir mit Rat und Tat zur Seite standen.

Natürlich möchte ich auch noch meiner Familie und meinem Partner für ihre Unterstützung danken. Ganz besonders meinen Eltern die mich in meinen Entscheidungen stets bestärkt und an mich geglaubt haben; und meiner Schwester die mir in allen Lebenslagen zur Seite steht.

Eidesstattliche Erklärung

Ich erkläre an Eides statt, dass die vorliegende Arbeit nach den anerkannten Grundsätzen für wissenschaftliche Abhandlungen von mir selbstständig erstellt wurde. Alle verwendeten Hilfsmittel, insbesondere die zugrunde gelegte Literatur, sind in dieser Arbeit genannt und aufgelistet. Die aus den Quellen wörtlich entnommenen Stellen, sind als solche kenntlich gemacht. Das Thema dieser Arbeit wurde von mir bisher weder im In- noch Ausland einer Beurteilerin/einem Beurteiler zur Begutachtung in irgendeiner Form als Prüfungsarbeit vorgelegt. Diese Arbeit stimmt mit der von den Begutachterinnen/Begutachtern beurteilten Arbeit überein.

Wien, am 16. Oktober 2018 Elisabeth Luchini

Kurzfassung

Die Inhalte der vorliegenden Dissertation sind im Laufe eines Kooperationsprojektes zwischen dem Institut für Mechanik und Mechatronik (Abteilung für Regelungstechnik und Prozessautomatisierung) und der Firma Liebherr-Transportation Systems GmbH & Co KG, Korneuburg als Industriepartner entstanden.

Ausfallsicherheit und Energieeinsparung beim Lebensmitteltransport ist ein aktuelles Thema, welches in dieser Arbeit behandelt wird. Der Schwerpunkt liegt auf der Entwicklung neuer Methoden für redundante und energieeffiziente Temperaturregelung, welche mit modellprädiktiver Regelungsstrategie umgesetzt wurde und der Beobachtung von nicht messbaren Störungen sowie Alterung des Kühlanhängers.

In dieser Dissertation wird ein modellprädiktives Regelungskonzept für die Temperaturregelung eines Kühlanhängers mit redundanten Kälteaggregaten präsentiert. Die Auflösung widersprüchlicher Optimierungsziele, wie die genaue Einhaltung der Temperatur, die Minimierung des Energieverbrauchs und des Verschleißes, stellt eine große Herausforderung dar.

Da die Dynamiken der Teilsysteme sehr unterschiedlich sind, ist ein hierarchisches Regelungskonzept vorteilhaft. Das komplexe nichtlineare Optimierungsproblem wurde in mehreren Teilproblemen aufgeteilt. Für die Temperaturregelung des Kühlanhängers wird eine lineare modellprädiktive Regelung verwendet, welcher in der Lage ist widersprüchliche Ziele zu lösen, indem Wettervorhersagen berücksichtigt aber auch Beschränkungen eingehalten werden. Bei der komplexen Regelung der Kälteaggregate ist eine gemischt-ganzzahlige Optimierung notwendig. Um Faktoren wie die Sonneneinstrahlung und die Alterung des Kühlanhängers berücksichtigen zu können wurde ein Beobachter entwickelt, welcher in der Lage ist die Störeinträge zu separieren.

Abstract

The content of this thesis originated in the course of a research project between the Institute of Mechanics and Mechatronics (Division of Control and Process Automation) and Liebherr-Transportation Systems GmbH & Co KG as industrial partner.

A current issue of potentials for reliability and saving energy in food transportation is discussed in this work. The research was focused on the development of new methodologies for redundant and energy-efficient temperature control and disturbance observation. In this context a model predictive control strategy and an observer for unmeasured disturbances and aging of the insulated cool box has been developed.

In this PhD Thesis a model predictive control concept for temperature control of an insulated cool box with redundant refrigeration systems is presented. Conflicting optimization goals naturally arise, where the strict adherence of the temperature, the minimization of energy consumption and wear poses major challenges.

As the dynamics of the subsystems are different a hierarchical control concept is advantageous. The complex nonlinear optimization problem has been split into a set of subproblems. For the temperature control of the insulated cool box a linear model predictive control is utilized, which is able to solve conflicting goals by taking weather predictions into account and by consideration of constraints. For the more complex control of the refrigeration systems a mixed-integer optimization is necessary. To be able to consider other factors as the solar irradiation and the aging of the insulated cool box an observer was designed, which is able to separate these disturbance impacts.

Contents

1 Overview **1**
- 1.1 Introduction . . . 1
- 1.2 Motivation . . . 2
- 1.3 Problem description . . . 2
- 1.4 Scientific questions . . . 3

2 System description **4**
- 2.1 Overall system . . . 4
- 2.2 Vapor compression cycle system . . . 4
- 2.3 Refrigeration system . . . 6
- 2.4 Insulated cool box . . . 12
- 2.5 Combined Linear Dynamics . . . 14

3 Numerically efficient control allocation **15**
- 3.1 State of the art . . . 15
- 3.2 Problem description . . . 16
- 3.3 On-line optimization of discrete variables . . . 20
- 3.4 Off-line computation of continuous variables . . . 24
- 3.5 Illustrative example . . . 25
- 3.6 Simulation results . . . 27
- 3.7 Summary . . . 31

4 Hierarchical model predictive control **32**
- 4.1 State of the art . . . 32
- 4.2 Hierarchical control concept . . . 34
- 4.3 Concept 1: Cooling capacity constraint . . . 35
- 4.4 Concept 2: Predicted temperature constraint . . . 45
- 4.5 Comparison of the concepts . . . 60
- 4.6 Summary . . . 62

5 Observer and estimation **63**
- 5.1 State of the art . . . 63
- 5.2 Observer and estimation concept . . . 65

5.3 Concept 1: Disturbance compensation with Luenberger observer 65
5.4 Concept 2: Full state observer with nonlinear estimation 74
5.5 Comparison of both concepts 87
5.6 Summary 89

6 Discussion and conclusion **90**
6.1 Scientific contributions 90
6.2 Discussion 91
6.3 Conclusion 92

Bibliography **94**

A Intersample bound **103**

Curriculum Vitae **104**

Nomenclature

List of abbreviations

AC	air conditioning
CA	control allocation
COP	coefficient of performance
EXV	electronic expansion valve
FDI	fault detection and isolation
HVAC	heating, ventilating and air conditioning
ICB	insulated cool box
ICE	internal combustion engine
LS	least squares
MI	mixed-integer
MILP	mixed-integer linear programming
MI-MPC	mixed-integer model predicitve control
MIO	mixed-integer optimizer
MIO3	mixed-integer optimizer with three large compressors
MIO6	mixed-integer optimizer with six compressors
MIQP	mixed-integer quadratic programming
MPC	model predictive control
MSE	mean square error
PDF	probability density function
pi	prediction interval
PI	proportional-integral controller
RC	refrigeration circuit
RMSE	root-mean-squared error
RS	refrigeration system
SSE	sum squared error
UIO	unknown input observer
VCC	vapor compression cycle

List of symbols

$*$	convolution operator
$\boldsymbol{A}$	system matrix of the combined dynamics
$\boldsymbol{A}_a$	augmented system matrix
$\boldsymbol{A}_A$	system matrix of the dynamic RC model
a	first position of a step change in $\boldsymbol{U}(k)$
A_{ICB}	surface are of the ICB
A_P	system matrix of the plant
$\boldsymbol{B}$	input matrix of the combined dynamics
$\boldsymbol{B}_a$	augmented input matrix
$\boldsymbol{B}_A$	input matrix of the dynamic RC model

b second position of a step change in $\boldsymbol{U}(k)$

B_P input matrix of the plant

$\boldsymbol{c}$ all counts of compressor switching for $\boldsymbol{\varrho}_{\mathrm{act}}$

$\boldsymbol{C}$ output matrix of the combined dynamics

$\boldsymbol{C}_a$ augmented output matrix

$\boldsymbol{C}_A$ output matrix of the dynamic RC model

c_l count of compressor switching for $\boldsymbol{\varrho}_{\mathrm{act}_l}$

C_P output matrix of the plant

$\boldsymbol{D}_A$ direct input-output matrix of the dynamic RC model

d_{amb} random disturbance effecting ϑ_{amb} in ° C

d_A direct input-output matrix of P_0 to P

d_{ICB} random disturbance effecting ϑ_{ICB} in ° C

d_n random disturbance in ° C

d_P direct input-output gain of the plant

$\boldsymbol{E}$ disturbance matrix of the combined dynamics

E energy consumption in J

$\boldsymbol{E}_a$ augmented disturbance matrix

$\boldsymbol{E}_P$ disturbance matrix of the plant

e_{model} Output error of the model

$e_{\vartheta_{\mathrm{ICB}}}$ prediction error of the plant's output ϑ_{ICB}

E_m disturbance matrix of the measured disturbances of the plant

E_o disturbance matrix of the non-measured disturbances of the plant

$\boldsymbol{F}_P^T$ distrubance input matrix of the plant

$\boldsymbol{F}_u$ prediction matrix based on ΔU

$\boldsymbol{F}_x$ prediction matrix based on current $\boldsymbol{x}_{\mathrm{MPC}}$

$\boldsymbol{F}_z$ prediction matrix based on ΔZ

f_α nonlinear function which describes the α deterioration

f_h function of the compressor status

$f_{\boldsymbol{\Psi}}$ function depending of the continuous variables

F-test statistical test with F-distribution

F_{crit} critical value of the F-test

$G_{\mathrm{A,P}}$ transfer function of P

$G_{\mathrm{A,u}}$ transfer function of u

$g_{\mathrm{AA}(t)}$ weighting function of the continuous anti-aliasing low-pass filter

G_{AA} pulse transfer function of the anti-aliasing low-pass filter

G_{FB} feedback gain

G_{ICB} pulse transfer function of the plant

$g_{P,i}$ nonlinear static relation for $P_{0,i}$

$g_{u,i}$ nonlinear static relation for $u_{0,i}$

G_H observer gain matrix

g_P nonlinear static relation for P_0

G_S gain for the estimated disturbance

g_u nonlinear static relation for u_0

$\boldsymbol{h}$ hours of all compressors of the RS in h

$\boldsymbol{H}$ sum of the operating hours of all combinations ϱ_{act} in h

$h_{i,j}$ operating hours of compressor j of RC i in h

H_l sum of the operation hours of the l-th combination of ϱ_{act} in h

i index for the RC

I unit matrix

j index for the compressors

J_α cost function of the α estimation

J_{C} cost function of the continuous decision values

J_{D} cost function of the discrete decision values

J_{D1} cost function of compressor switching

J_{D2} cost function of operating hours

J_L cost function of the optimal observer poles selection

J_{O} cost function of other criteria (such as control settling time)

J_{P} cost function of power consumption

J_{W} cost function of wear

J_{glob} global model

J_{loc} local model

J_1 cost function of the MPC

J_2 cost function of the MI-MPC

K samples of the large sampling time T_S

k samples of the small sampling time t_S

$K_{A,u}$ gain of the RS model

K_I gain of the integral part of the PI controller

K_{MPC} feedback matrix of the unconstrained case

K_P gain of the proportional part of the PI controller

$\boldsymbol{L}$ vector of observer poles

l index of the subset of the compressor combinations ϱ_{act}

$\mathcal{L}$ Lagrange function

L_1, L_2 observer poles

$\boldsymbol{M}$ integral effect of z for a small sample k

$\boldsymbol{M}_\Sigma$ cumulative effect of all $\boldsymbol{M}s$ over one large sample K

$\boldsymbol{M}_P$ integral effect of z on the ICB for a large sample K

mc_{p} thermal mass capacity of the ICB in $\frac{kgm^2}{s^2K}$

N simulatin time in sec

n_c control horizon of the CA

N_c control horizon of the MPC

n_i sum of all compressors in the RC i

n_l number of all compressor combinations in the subset $\boldsymbol{\varrho}_{\text{act}}$

$n_{n_{RC}}$ sum of all compressors in the RC n_{RC}

n_p prediction horizon of the CA

N_p prediction horizon of the MPC

n_{RC} number of RCs

n_s number of samples

n_κ number of permutations

$\boldsymbol{o}$ plane orthogonal to state trajectory

$o_1, ..., o_{n-1}$ parametrization of orthogonal plane $\boldsymbol{o}$

P total electrical power of the active RCs in kW

p number of parameters in the regression model

$\mathcal{P}$ Poincaré map

p_{D_i} discharge pressure of RC i in bar

P_i electrical power of the RC i in kW

$\boldsymbol{P}_L$ solution of the discrete-time Riccati equation with the augumented matrices of the MPC

P_{MPC} characteristic polynomial of the MPC

P_{obs} characteristic polynomial of the current observer

p_{S_i} suction pressure of RC i in bar

P^{κ} total electrical power of the permutation with index κ in kW

$P_{0,i}$ stationary electrical power consumption of RC i in kW

P_0 total stationary electrical power consumption in kW

P_{PI} electrical power consumption of the PI-controller solution

P_R solution of the discrete-time Riccati equation with the plant matrices of the MPC

$p(u)$ probability density function

$\dot{Q}_{\alpha}$ heat input which arises by α_1 in kW

$\dot{Q}_{\alpha_0}$ heat input which arises by α_0 in kW

$\dot{Q}_{\hat{\alpha}}$ heat input which arises by $\hat{\alpha}_1$ in kW

$\dot{Q}_{\mathrm{H},i}$ heating capacity of RC i in kW

$\dot{Q}_{\mathrm{H}}$ total heating capacity of the active RCs in kW

$\dot{Q}_{\mathrm{loss}}$ heat flow through the surface of the ICB in kW

$\dot{Q}_{\mathrm{req}}$ required cooling capacity in kW

$\dot{Q}_{\mathrm{sol}}$ solar irradiation in kW

$\dot{Q}_z$ total disturbance in kW

$\dot{Q}_z^{\mathrm{pred}}$ prediction of the disturbance in kW

$\hat{\dot{Q}}_z$ predicted total disturbance in kW

$\hat{\dot{\boldsymbol{Q}}}_z^r$ vector of all estimated $\hat{\dot{\boldsymbol{Q}}}_z$ values for day r

$\boldsymbol{R}_1$ weighting factor for the output error of the MPC

$\boldsymbol{R}_2$ weighting factor penaltize the change of the input variable of the MPC

$\boldsymbol{R}_3$ weighting factor for the deviation of the input signal of the MI-MPC

$\boldsymbol{R}_4$ weighting factor for P of the MI-MPC

$\boldsymbol{R}_5$ weighting factor for enforcing switching action of the MI-MPC

$\boldsymbol{R}_6$ weighting factor penaltize the compressor switching of the MI-MPC

R_O weighting factor for other criterions

R_P weighting factor for electrical power consumption

R_W weighting factor for wear

$\mathbb{S}$ locally differentiable transversal section of $\boldsymbol{x}(t)$

$\boldsymbol{s}$ compressor states of all compressors of the RS

$\boldsymbol{s}_i$ compressor states of all compressors of RC i

S switching count

$s_{i,j}$ compressor state of the compressor j of RC i

t continuous time

$T_{A,u}$ time constant of the RS model

t_{ch} time where a significant acceleration of the deterioration of the α-value happens

t_{crit} critical time where α_{crit} is reached in sec

t_{cst} control settling time in sec

T_{D_i} discharge temperature of RC i in K

t_{end} life time of the ICB in sec

t_{hist} start time of the used samples for J_{glob} and J_{loc}

t_{now} current time in sec

t_o sampling time of the observer in sec

T_S large sampling time in sec

t_S small sampling time in sec

T_{SH_i} superheat of RC i in K

t_0 start time in sec

$\boldsymbol{u}(k)$ optimal cooling capacity trajectory of the CA in kW

$\tilde{t}_{\mathrm{end}}$ reduced life time of the ICB in sec

$\boldsymbol{U}(K)$ optimal cooling capacity trajectory of the MPC in kW

$\boldsymbol{U}(k)$ upsampled $\boldsymbol{U}(K)$ for the the sampling time k in kW

$\boldsymbol{u}_\kappa$ range of possible cooling capacity from permutation κ

$\boldsymbol{u}_A$ input vector of the dynamic RC model

u total cooling capacities of the active RCs in kW

$\overline{u}$ average cooling capacity of the active RCs in kW

$\tilde{u}(t)$ low-pass filtered $u(t)$

u_i cooling capacity of RC i in kW

$u_{\max,\kappa}$ maximum possible cooling capacity from permutation κ

$u_{\min,\kappa}$ smallest possible cooling capacity from permutation κ

U_{MPC} output of the MPC in kW

u_{past} sum of all already implemented $u(k)$

u_{PI} cooling capacity of the PI-controller solution

u_{ss} steady state of u_P

u_0 total stationary cooling capacity in kW

$u_{0,i}$ stationary cooling capacity of RC i in kW

$U_1(K)$ first entry of $\boldsymbol{U}(K)$

$u_{\Delta\Sigma}$ Term of J_2 which enforces switching action

$u_{\sum}$ possible cooling capacity range of all permutations in kW

$u(t)$ continuous version of $u(k)$

$\boldsymbol{v}$ valve positions of all RCs in %

V terminal cost of the MPC

v_i valve position of RC i in %

w_S switching event

$\boldsymbol{X}$ regressor vector of the least squares estimation

$\boldsymbol{x}$ state vector of the combined dynamics

$\boldsymbol{x}_A$ state vector of the dynamic RC model

$\boldsymbol{x}_\alpha$ regressor vector of the α estimation

$\boldsymbol{x}_{\text{cl}}$ closed loop state vector

$\boldsymbol{x}_{\text{set}}$ set point of the combined dynamics

x_{MPC} augmented state vector

x_P state of the plant

$\hat{x}_P$ predicted state of the plant

$\tilde{x}_P$ error between the state and predicted state of the plant

x^q q-th intersection of $\boldsymbol{x}(t)$ with $\mathbb{S}$

x_{ss} steady state of x_P

$\boldsymbol{y}$ output vector of the combined dynamics

$\boldsymbol{Y}^{\text{ref}}$ reference output trajectory

$\boldsymbol{y}_A$ output vector of the dynamic RC model

$\hat{\boldsymbol{Y}}$ predicted output trajectory

$\hat{\boldsymbol{y}}$ predicted output

y output variable

y_P output of the plant

$\hat{y}_P$ predicted output of the plant

y_{set} set point temperature of the ICB

$y_{y_P(K)=y_{\text{set}}}$ combined dynamics output for $y_P(K) = y_{\text{set}}$ for all K

$\boldsymbol{z}$ disturbance vector of the plant

$\boldsymbol{z}_{\text{env}}$ measurable environmental conditions

z_m measured distruances

z_o unknown distruances

$\hat{\boldsymbol{z}}_m^p$ prediction of the ambient temperature in ° C

$\hat{\boldsymbol{z}}_o^p$ prediction trajectory of the disturbance in kW

$\hat{z}_o$ predicted unknown distruances

List of greek letters

α heat transfer coefficient

α_0 known heat transfer coefficient of a new ICB

α_1 deterioration of the heat transfer coefficient over time

α_{crit} critical α-value

α_{ch} α-value where a significant acceleration of the deterioration of α happens

α_{now} current α

$\alpha_{N_{\text{sim}}}$ α at the end of the simulation

$\hat{\alpha}_{1,\text{glob}}$ estimated deterioration of α_1 with global model

$\hat{\alpha}_{1,\text{loc}}$ estimated deterioration of α_1 with local model

$\hat{\alpha}_1$ predicted deterioration of the heat transfer coefficient over time

β confidence level

γ weighting factor for J_α

$\boldsymbol{\Gamma}$ integral effect of u_0 for a small sample k

Γ_P integral effect of u_0 on the ICB for a large sample K

$\boldsymbol{\delta}_{\text{ineq}}$ inequality constraints

δ_{eq} equality constraint

$\Delta\bullet$ delta formulation of $\bullet$ of the MPC

ϵ_1 binary variable in definiton of $u_{\Delta\Sigma}$

ϵ_2 binary number for J_α

$\boldsymbol{\eta}$ denotes the effect of the disturbances

$\boldsymbol{\theta}_\alpha$ parameters of the α estimation

$\boldsymbol{\theta}_L$ parameters of the observer poles

$\boldsymbol{\vartheta}_{\text{ICB}}^{\text{ref}}$ ICB set temperature trajectory in $^\circ$ C

ϑ_{ICB} ICB temperature in $^\circ$ C

$\vartheta_{\text{ICB}}^{\text{ref}}$ actual ICB set temperature in $^\circ$ C

$\hat{\boldsymbol{\vartheta}}_{\text{ICB}}$ predicted ICB temperature trajectory in $^\circ$ C

$\hat{\vartheta}_{\text{ICB}}$ predicted ICB temperature in $^\circ$ C

$\tilde{\vartheta}_{\text{ICB}}$ measured ICB temperature in $^\circ$ C

$\boldsymbol{\vartheta}_{\text{amb}}^{\text{pred}}$ predicted disturbance trajectory in $^\circ$ C

ϑ_{amb} ambient temperature in $^\circ$ C

$\tilde{\vartheta}_{\text{amb}}$ measured ambient temperature in $^\circ$ C

$\boldsymbol{\kappa}$ indices of the permutations which can provide $\dot{Q}_{req}$

κ index of the permutations

λ integer ratio of large and small sampling time

$\boldsymbol{\mu}_{\text{ineq}}$ Lagrange multiplier for inequality constraints

μ_{eq} Lagrange multiplier for equality constraints

ν degrees of freedom

$\boldsymbol{\varrho}$ vector of all discrete decision variables of the RS

$\boldsymbol{\varrho}_{\text{act}}$ subset of ϱ with the actual compressor combinations

$\boldsymbol{\varrho}_{\text{act},l}$ the l-th compressor combination of $\boldsymbol{\varrho}_{\text{act}}$

$\hat{\sigma}_e$ estimated residual

σ^2 variance of the random disturbance d_n

τ time variable

$\boldsymbol{\Phi}$ transition matrix for small sample k

Φ_P transition matrix of the ICB for large sample K

χ_{ar} set of constraints

$\boldsymbol{\Psi}$ vector of all continuous decision variables of the RS

$\boldsymbol{\Psi}_i$ vector of all continuous decision variables of the RC i

$\boldsymbol{\Psi}_{\text{constr},i}$ vector of time-varying system constraints of the RC i

$\boldsymbol{\omega}$ speed of all compressors of the RS in $rad \cdot s^{-1}$

$\boldsymbol{\omega}_i$ speed of all compressors of RC i in $rad \cdot s^{-1}$

$\boldsymbol{\omega}_{\text{FC},i}$ speed for the condenser fan of the RC i in $rad \cdot s^{-1}$

$\boldsymbol{\omega}_{FE,i}$ speed for the evaporator fan of the RC i in $rad \cdot s^{-1}$

$\omega_{i,j}$ speed of the compressor j of RC i in $rad \cdot s^{-1}$

List of sub-/superscripts

$\bullet^\star$ optimal value of $\bullet$

$\bullet_{,\mathrm{B}}$	method B	$\bullet_{\max}$	maximal value of $\bullet$
$\bullet_{,\mathrm{b}}$	method b	$\bullet_{\min}$	minimal value of $\bullet$
$\bullet_c$	without observer	$\bullet_o$	with observer

Chapter 1

Overview

1.1 Introduction

Food transport systems are widely used. There are at least one million refrigerated road vehicles in use in the world, [28]. Their refrigeration systems (RSs) consume a substantial amount of energy. There is also a rising trend towards higher consumption of several food products with a consequent increase in environmental impacts. Such a significant impact are greenhouse gas emissions, [93]. In UK the commercial food sector, including agriculture, food manufacture, transport and retail is responsible for 22 % of the total greenhouse gas emissions. Technologies and approaches in food transport refrigeration and their environmental affects are reviewed in [92]. The impacts are expressed in terms of greenhouse gas emissions arising from the fuel consumption of the vehicle and refrigeration system engines and refrigerant leakage to the environment. Norway is yet another example. In Norway, seafood is one of the largest exports, mostly in fresh, frozen or dried form, [97].
The transport of cooled or frozen goods requires effective control of the temperature inside the insulated cooling box (ICB) to prevent degeneration of perishable goods. Therefore, one of the objectives of technical development is to increase their energy efficiency and availability. In the case of using an internal combustion engine as primary energy source also the reduction of emissions is crucial.
In order to obtain low maintenance and energy costs and to maximize availability of the system, ICBs will be equipped with redundant refrigeration circuits (RCs) each utilizing one or more compressors. However, this approach leads to a multitude of both switched (compressor on/off state) and continuous (expansion valve, fan speed) control variables, calling for an mixed-integer (MI) optimization.
In many applications data links to weather predictions are available making model predictive control (MPC) of the ICB's temperature an attractive solution. MPC is an attractive method where conflicting targets and predictions of disturbances such as ambient temperature exist. Furthermore, operational and technological constraints can be easily incorporated in the optimization strategy.
Nevertheless, fast acting disturbances which are not detected by a dedicated sensor

- like the solar irradiation - disturb the optimal control of the MPC and act as an unknown input. Also the slowly deteriorating heat transfer coefficient of the ICB cannot be directly measured. The heat transfer coefficient is an important model parameter necessary for an accurate model in the MPC, and it also indicates the state of health of the ICB. Therefore, in this thesis different methods which are able to solve the above mentioned problems are proposed.

1.2 Motivation

Typically, an RS is designed for one specific operating point, but it operates most of the life time in conditions significantly different from design cases. Therefore, it is worth to analyze how to make these systems operate more efficiently by optimizing all operational modes. Using an RS with multiple RCs each with multiple compressors finer discretization can be achieved, which is an advantage at part-load conditions. Multiple RCs also provide a redundant system, which leads to a higher system availability but at the same time requires a more complex control strategy.
Additionally, the time constant of the ICB is typically in the range of 1.5 hours, and the RCs variables respond within minutes. The proposed solution to this problem is a hierarchical control structure where a linear MPC controls the temperature inside the ICB based on reference and disturbance trajectories. It operates at a low sampling frequency and covers a long prediction horizon to effectively cope with the large time constant of the ICB. An underlying control allocation (CA), which is operating at a high sampling frequency and a small prediction horizon, optimizes the control variables of the RS. This structure effectively solves the above-mentioned problems: 1) The optimization of the systems with largely differing time constants is now split into separate optimization problems. 2) The CA horizon is short, so feasible solutions are more likely and the computational load will be small. 3) Different contradicting optimization goals are incorporated in the control structure.

1.3 Problem description

One typical challenge is the hybrid nature of the refrigeration system; this means that both continuous and switching control variables have to be optimally set by the control scheme. Solving such a system is a computationally expensive problem. However, optimization of the control variables in the sense of reducing energy costs or wear is an important topic. Besides that the optimization of the temperature of the ICB and the optimization of the refrigeration system have time constants which differ by a major factor. Therefore a hierarchical concept with different sampling times and prediction horizons is advantageous. For the temperature control an MPC is a well known control method. Measured and predicted disturbances could be considered.

But another challenge is that the number of sensors is kept small due to economic reasons, so an estimation of solar irradiation from existing measurements is desirable. Since both effects, the unknown disturbances and the slowly deteriorating heat transfer coefficient α, act additively on the ICB's temperature, the custom disturbance observer can reconstruct the contributions of irradiation and aging have to be reconstructed.

1.4 Scientific questions

The following scientific questions will be treated and answered in the main part of this thesis:

1. Control allocation problem: A large number of both continuous and switched control variables in the RS have to be chosen such that a multitude of contradicting criteria are met.

2. Temperature control of the ICB utilizing a suitable control allocation method for the RS, constraint handling, and disturbance predictions have to be designed.

3. The methods developed as a solution to question one and two shall be extended with simultaneous estimation of disturbances and the heat transfer coefficient of the ICB using a suitable observer structure.

Chapter 2

System description

2.1 Overall system

Transport systems for perishable goods consist of an insulated cool box (ICB) which includes the goods and the refrigeration system which provides the necessary cooling capacity for cooling the ICB. The refrigeration system (RS) consists of a refrigeration circuit (RC) which includes at least a condenser, an evaporator, an electronic expansion valve and a compressor. The RS provides a cooling capacity u, which is the only control variable. Main disturbances of the ICB are the the heat flow through the surface $\dot{Q}_{\text{loss}}$, solar irradiation $\dot{Q}_{\text{sol}}$ and a slowly time-varying heat transfer coefficient, Fig. 2.1.

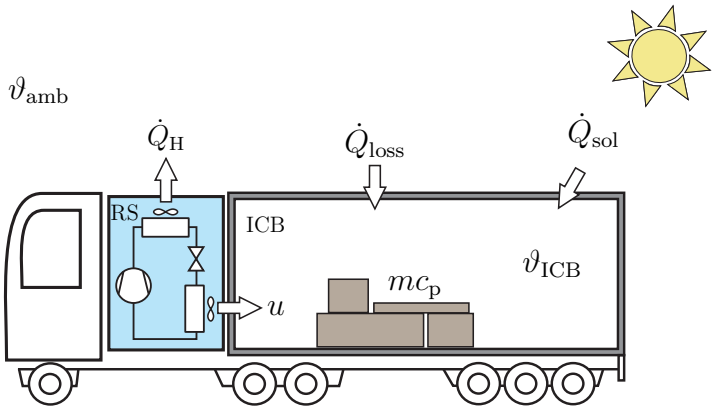

Figure 2.1: Model of the insulated cool box with refrigeration system.

2.2 Vapor compression cycle system

A single RC consists of four main elements: (a) Compressor, (b) condenser, (c) evaporator and (d) electronic expansion valve (EXV), Fig. 2.2. All components in the circuit are linked with pipes, demonstrating inherently nonlinear behavior. The vapor compression cycle (VCC) uses a refrigerant as the medium which absorbs and removes heat

from the space to be cooled and subsequently transfers that heat elsewhere. The ideal form of this thermodynamic cycle utilizes four processes: (1-2) isentropic compression; temperature and pressure of the refrigerant raises, (2-3) isobaric heat rejection and condensation, (3-4) isenthalpic expansion; temperature and pressure drops, (4-1) isobaric heat absorption and evaporation, Fig. 2.2.

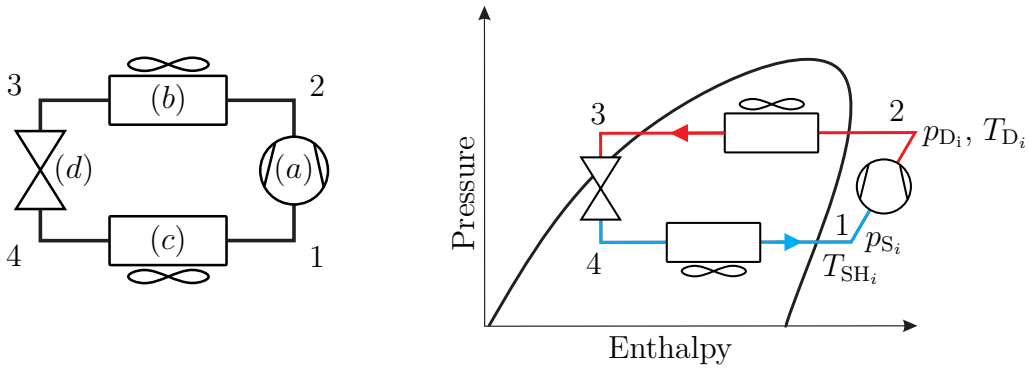

Figure 2.2: Left: Main elements of a single RC; Right: Pressure-enthalpy diagram with superheat T_{SH}, suction pressure p_{S}, discharge pressure p_{D} and discharge temperature T_{D}.

Effective control of these systems is essential in order to maximize efficiency and ensure safe operation, particularly during system startup and when responding to changes in heat load or external conditions. The dynamics of these systems evolve at different time scales. The dominant dynamics are typically those of the evaporator and condenser. Two heat exchanger modeling approaches are commonly used, [73, 74]: 1) Moving-boundary lumped-parameter methods, [36] where separate control volumes and lumped parameters for each fluid phase (i.e. subcooled liquid, two-phase, or superheated vapor) is employed. Time-varying boundaries for these control volumes are typically used. 2) Finite-volume distributed-parameter, [67]. These models discretize the heat exchanger using average parameter values within each volume and applying equations for the conservation of energy and mass. A comparison of both methods is made in [8].
The physical process of a VCC is in fact complex and not fully state controllable [5, 6]. In order to improve the operating stability of the complex RS, it is necessary to obtain a simple and accuracy mathematical model for system control. In [38], a control oriented model for combined compression ejector system is proposed. By analyzing the inner relationship between compressor and ejector, a hybrid model is built based on thermodynamic principles and a lumped parameter method. A comparison of three methods (a traditional gain scheduled PI-based controller, a predictive functional controller and a predictive functional controller with a neural network model) for controlling the superheat in a RS is given in [66].
In this work it is assumed that a suitable model of the RC exists. A suitable model of the RC in the sense of control design is typically of simple structure and low-order,

nevertheless it should cover the dominant nonlinearities and dynamics. Therefore, either a static look-up table or a Hammerstein-model is proposed in this work, as explained in more detail in Section 2.3.5.

2.3 Refrigeration system

2.3.1 Fundamental structure

The RS can consist of a variable number of parallel RCs denoted by the index $i \in [1,\ 2,\ \ldots,\ n_{\mathrm{RC}}]$, each RC can have multiple compressors.
Fig. 2.3 shows the structure of such a system, where each RC i provides a cooling capacity $\dot{Q}_i$ and heating capacity $\dot{Q}_{H,i}$. The electrical power consumed by all compressors n_i in each RC i is denoted by P_i. These variables depend on the ambient temperature ϑ_{amb}, the ICB temperature ϑ_{ICB} and all continuous variables $\boldsymbol{\Psi}_i$ (e.g. EXV position, compressor and fan speeds).

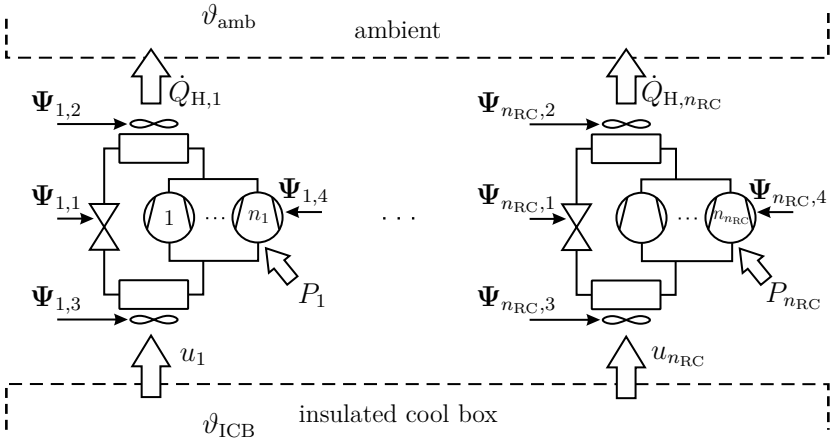

Figure 2.3: The structure of the refrigeration system with multiple refrigeration circuits each with multiple compressors.

2.3.2 Variables of the RCs

Each RC i includes a plurality of compressors denoted by the index $j \in [1,\ 2,\ \ldots,\ n_i]$. The compressor states $\boldsymbol{s}_i$ of the RC i are

$$\boldsymbol{s}_i = \begin{bmatrix} s_{i,1} & s_{i,2} & \ldots & s_{i,n_i} \end{bmatrix}. \tag{2.1}$$

The values of $s_{i,j}$ describe the state of the compressor j of the RC i and can vary between three discrete values

$$s_{i,j} = \begin{cases} 0 & \text{if compressor } j \text{ is off} \\ 1 & \text{if compressor } j \text{ is on} \\ -1 & \text{if compressor } j \text{ is not available} \end{cases} \tag{2.2}$$

The value $s_{i,j} = -1$ is a result of different system disturbances, such as a defect compressor, switching prohibition due to latency time or an iced up evaporator.
The states of all compressors in the RS are

$$\boldsymbol{s} = \begin{bmatrix} \boldsymbol{s}_1 & \boldsymbol{s}_2 & \dots & \boldsymbol{s}_{n_{\mathrm{RC}}} \end{bmatrix}. \tag{2.3}$$

Each compressor can have variable speed $\omega_{i,j}$, therefore, different cooling capacities become possible. The rotational speeds $\boldsymbol{\omega}_i$ of all compressors of the RC i are

$$\boldsymbol{\omega}_i = \begin{bmatrix} \omega_{i,1} & \omega_{i,2} & \dots & \omega_{i,n_i} \end{bmatrix}. \tag{2.4}$$

The compressor speeds of all compressors in the RS are

$$\boldsymbol{\omega} = \begin{bmatrix} \boldsymbol{\omega}_1 & \boldsymbol{\omega}_2 & \dots & \boldsymbol{\omega}_{n_{\mathrm{RC}}} \end{bmatrix}. \tag{2.5}$$

Further actuating variables for each RC i are the condenser fan speed $\omega_{\mathrm{FC},i}$, the evaporator fan speed $\omega_{\mathrm{FE},i}$ and the position of the EXV v_i, where the value of v_i describe the normalized valve opening position.
All these continuous variables of the RC i are collected in a decision vector $\boldsymbol{\Psi}_i$, Fig. 2.3,

$$\boldsymbol{\Psi}_i = \begin{bmatrix} v_i & \omega_{\mathrm{FC},i} & \omega_{\mathrm{FE},i} & \boldsymbol{\omega}_i \end{bmatrix}, \tag{2.6}$$

The decision vector for all RCs is

$$\boldsymbol{\Psi} = \begin{bmatrix} \boldsymbol{\Psi}_1 & \dots & \boldsymbol{\Psi}_{n_{\mathrm{RC}}} \end{bmatrix}. \tag{2.7}$$

If the compressors have only single speeds or discrete values for the speeds, then the compressor speed is a discrete value like the compressor states. The same applies to the condenser and evaporator fan speeds.
Depending on the operation mode and measurable environmental conditions $\boldsymbol{z}_{\mathrm{env}}$, such as ambient temperature and current temperature in the ICB

$$\boldsymbol{z}_{\mathrm{env}} = \begin{bmatrix} \vartheta_{\mathrm{amb}} & \vartheta_{\mathrm{ICB}} \end{bmatrix}, \tag{2.8}$$

the RS provides a cooling capacity u. The cooling capacity is the sum of all cooling capacities from the active RCs,

$$u = \sum_{i=1}^{n_{\mathrm{RC}}} u_i. \tag{2.9}$$

The heating capacity $\dot{Q}_{\mathrm{H},i}$ from each RC i is delivered to the ambient.
The total electrical power consumed by the compressors is

$$P = \sum_{i=1}^{n_{\mathrm{RC}}} P_i. \tag{2.10}$$

An RS with multiple RCs and compressors can generate different cooling capacities. Not only due to different capacities of the compressors but also utilizing multiple RCs a fine discretization of the cooling capacity can be realized. For example if two compressors in one RC are running, the cooling capacity is smaller than the cooling capacity of two compressors each running in a separate RC (assuming identical compressors and RCs). The reason is that the condenser and evaporator surface is doubled for the second case, in contrast to the first case which uses the same RC and therefore, has no additional surface.
The redundancy of the RCs also enables supply of the same u using several different combinations of switching and continuous variables. Hence, the redundant system leads to a higher system availability but at the same time requires a more complex control strategy.

2.3.3 Admissible operating regions

All actuating variables are subject to limitations, which are specified by the system architecture and the individual components. These limitations define the possible operating envelope of the RCs:

$$s_{i,j} \in \mathbb{Z}_0^+ : s_{i,j} = \{-1, 0, 1\} \tag{2.11}$$

$$\begin{aligned} v_i &\in \mathbb{R}_0^+ : 0 \leq v_i \leq 1 \\ \omega_{\mathrm{FC},i} &\in \mathbb{R}_0^+ : 0 \leq \omega_{\mathrm{FC},i} \leq \omega_{\mathrm{FC,max},i} \\ \omega_{\mathrm{FE},i} &\in \mathbb{R}_0^+ : 0 \leq \omega_{\mathrm{FE},i} \leq \omega_{\mathrm{FE,max},i} \\ \boldsymbol{\omega}_i &\in \mathbb{R}_0^+ : \mathbf{0} \leq \boldsymbol{\omega}_i \leq \boldsymbol{\omega}_{\mathrm{max},i}. \end{aligned} \tag{2.12}$$

To ensure that the RC operates in a secure range, further system constraints are defined. Typical constraints are defined for the superheat T_{SH_i}, the suction pressure p_{S_i}, the discharge pressure p_{D_i}, the discharge temperature T_{D_i} and the evaporator temperature T_{evap_i}, Fig. 2.2. It is however possible to include additional constraints.

$$\begin{aligned} T_{\mathrm{SH}_i} &\geq T_{\mathrm{SH,min},i} \\ p_{\mathrm{S}_i} &\geq p_{\mathrm{S,min},i} \\ p_{\mathrm{D}_i} &\leq p_{\mathrm{D,max},i} \\ T_{\mathrm{D}_i} &\leq T_{\mathrm{D,max},i} \\ T_{\mathrm{evap}_i} &\geq T_{\mathrm{evap,min},i} \end{aligned} \tag{2.13}$$

The constraints yield a reduced time-variant feasible operating envelope. As a result, also the actuating variables, eq. (2.12), are bounded by

$$\boldsymbol{\Psi}_{\text{constr,i}} = \begin{bmatrix} v_{\min,i} & \omega_{\text{FC},\min,i} & \omega_{\text{FE},\min,i} & \boldsymbol{\omega}_{\min,i} \\ v_{\max,i} & \omega_{\text{FC},\max,i} & \omega_{\text{FE},\max,i} & \boldsymbol{\omega}_{\max,i} \end{bmatrix}. \tag{2.14}$$

The system constraints, eq. (2.13), have monotonous characteristics, and thus the feasible operating envelope is limited to the region where no constraint is violated. The feasible operating envelope also varies depending on the number of active compressors. In this work applications with small latency time are focused. Therefore, the gradient of the temperature trajectory is small. The latency time is considered by the state of the compressor, eq. (2.2). In the case of large latency times minimal off-time and minimal on-time for each compressor would be necessary as additional constraints.

2.3.4 Redundancy

All sets of active components which achieve the same cooling capacity are termed a permutation. Hence, different cooling capacities are always provided by different permutations. Note that a specific permutation with the index $\kappa \in [0, n_\kappa]$, where n_κ is the number of possible permutations, can be realized by different actually active compressor combinations ϱ (for example in the case of identical compressors one active compressor will provide a certain cooling capacity regardless in which RC it is running). Consequently, the permutation contains no information which compressor of which RC should be used best.
Each permutation within the feasible operating envelope provides a range of cooling capacity which is defined by the smallest $u_{\min,\kappa}$ and largest $u_{\max,\kappa}$ possible cooling capacity. All permutations are sorted ascending by $u_{\min,\kappa}$, Fig. 2.4.
Depending on the constraints, eq. (2.13) and $\boldsymbol{z}_{\text{env}}$, the feasible operating envelope is time-variant, and thus also the possible cooling capacities. The range of cooling capacity $\boldsymbol{u}_\kappa = [u_{\min,\kappa}\ u_{\max,\kappa}]$ which can be provided with all permutations can be collected to the set

$$\boldsymbol{u}_\Sigma = \{\boldsymbol{u}_1\ \boldsymbol{u}_2 \dots \boldsymbol{u}_{n_\kappa}\} = \bigcup_\kappa \boldsymbol{u}_\kappa. \tag{2.15}$$

The system can provide cooling capacity ranges which are partially overlapping, Fig. 2.4. This degree of freedom is used to achieve different optimization targets (operational modes). The index set of possible permutations $\boldsymbol{\kappa}$ which can provide a given cooling capacity $\dot{Q}_{\text{req}}$ can be formulated as

$$\boldsymbol{\kappa} = \{\kappa \;\big|\; \dot{Q}_{\text{req}} \in \boldsymbol{u}_\kappa\}. \tag{2.16}$$

In $\boldsymbol{\kappa}$ permutations which are currently not available, eq. (2.2), are already considered, therefore, the corresponding permutations are not part of $\boldsymbol{\kappa}$.
In the case of discrete speed values for the compressors or fans, the number of continuous variables is reduced and the number of possible permutations will increase.

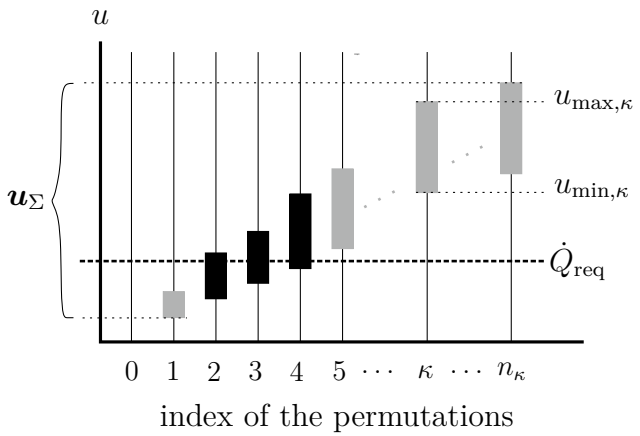

Figure 2.4: Cooling capacity range of all permutations for constant environmental conditions $\boldsymbol{z}_{\text{env}}$. The borders of permutation κ are denoted by the smallest $u_{\min,\kappa}$ and largest $u_{\max,\kappa}$ cooling capacity. The black bars show the permutations which can provide the required cooling capacity $\dot{Q}_{\text{req}}$.

2.3.5 Modeling RCs

Modeling an RC with all dynamic behavior requires a complex model, whereas control design requires a simple model. Therefore, a balance between complexity and accuracy must be considered.
The RS is modeled by nonlinear static relations g_u, g_P between the control variables $\boldsymbol{s}$ and $\boldsymbol{\Psi}$ and the stationary cooling capacity u_0 and the stationary electrical power consumption P_0, respectively. The nonlinear static part is followed by a linear dynamic state-space model which captures actuator dynamics. This is a so-called Hammerstein structure [58], see Fig. 2.5, which has also been used in [27] to model an RS.

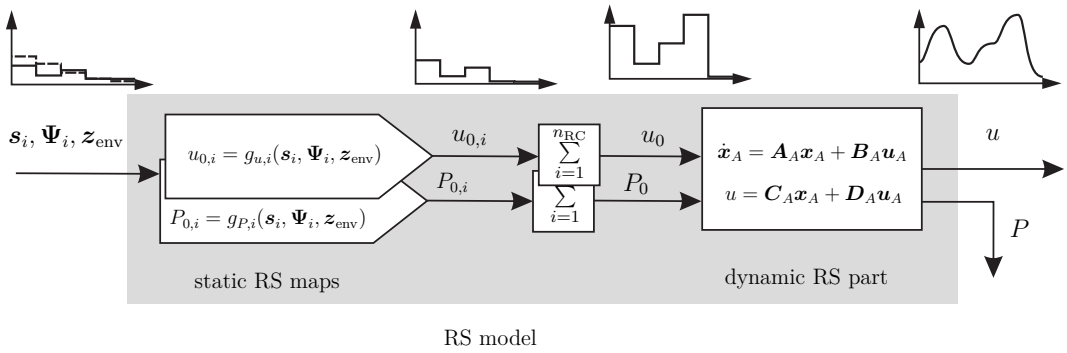

Figure 2.5: The RS is modeled by a Hammerstein system: A nonlinear static map is connected in series by a linear dynamic part.

Stationary RC model

For controlling a cooling load the transient behavior of the RS is not crucial. The reason for this assumption is that the time constant of an ICB compared to the RS is substantially larger. Accordingly the method replaces the complex models of the RS with look-up tables, therefore, a quasi static model of the RS is used.
The data of the look-up tables $g_{u,i}$ and $g_{P,i}$ are generated with an RC model in the modeling language Modelica and validated with measurement data. It is also possible to generate the look-up tables by measured data from different use cases, then the method is independent of complex RS simulations.
Each look-up table is a sampled representation of a function in different variables. The input variables are $\boldsymbol{s}_i$, $\boldsymbol{\Psi}_i$ and $\boldsymbol{z}_{\text{env}}$, see Fig. 2.5.
Each RC has it's own look-up tables. RCs with multiple compressors have look-up tables for all possible combinations of running compressors. As mentioned before, an RC with two running compressors has different characteristics then two parallel RCs each with one running compressor. The look-up tables provide exactly this information. In steady state the i-th RC provides $u_{0,i} = g_{u,i}(\boldsymbol{s}_i, \boldsymbol{\Psi}_i)$. The sum of all cooling capacities of the active RCs u_0 is

$$u_0 = \sum_{i=1}^{n_{\text{RC}}} u_{0,i} = \sum_{i=1}^{n_{\text{RC}}} g_{u,i}(\boldsymbol{s}_i, \boldsymbol{\Psi}_i) = g_u(\boldsymbol{s}, \boldsymbol{\Psi}). \tag{2.17}$$

The steady state electrical power consumed by the active compressors in the i-th RC is denoted by $P_{0,i} = g_{P,i}(\boldsymbol{s}_i, \boldsymbol{\Psi}_i)$. The sum of the power consumptions of the active RCs P_0 is

$$P_0 = \sum_{i=1}^{n_{\text{RC}}} P_{0,i} = \sum_{i=1}^{n_{\text{RC}}} g_{P,i}(\boldsymbol{s}_i, \boldsymbol{\Psi}_i) = g_P(\boldsymbol{s}, \boldsymbol{\Psi}). \tag{2.18}$$

Dynamic RC model

Furthermore, a linear dynamic part transforms u_0 and P_0 to the actual outputs u and P. The RS's linear continuous-time dynamics are given by

$$\begin{aligned} \dot{\boldsymbol{x}}_A &= \boldsymbol{A}_A \boldsymbol{x}_A + \boldsymbol{B}_A \boldsymbol{u}_A, \\ \boldsymbol{y}_A &= \boldsymbol{C}_A \boldsymbol{x}_A + \boldsymbol{D}_A \boldsymbol{u}_A, \end{aligned} \tag{2.19}$$

where $\boldsymbol{u}_A = [u_0 \quad P_0]^T$ is the output of the static RS maps, and the outputs of the RS are the actual cooling capacity u to the ICB and the actual power consumption P which is an input to the optimization. Note that the RS's dynamic description has an input-output gain of one, and no disturbance is assumed to act directly on the RS. Direct feedtrough described by $\boldsymbol{D}_A = [\boldsymbol{0} \;\; d_A]$ affects only the power P_0 to P.

2.4 Insulated cool box

The behavior of the ICB is approximated with a first order linear differential equation

$$mc_\mathrm{p}\frac{d\vartheta_\mathrm{ICB}}{dt} = -u + \alpha(t)A_\mathrm{ICB}(\vartheta_\mathrm{amb} - \vartheta_\mathrm{ICB}) + \dot{Q}_\mathrm{sol}, \tag{2.20}$$

with the total thermal capacity mc_p of the ICB and content, the time-varying heat transfer coefficient $\alpha(t)$, the surface area A_ICB of the ICB, the ambient temperature ϑ_amb, the ICB temperature ϑ_ICB, the cooling capacity u and the solar irradiation $\dot{Q}_\mathrm{sol}$, see Fig. 2.6. Note that the humidity inside the ICB is usually not considered by the control.

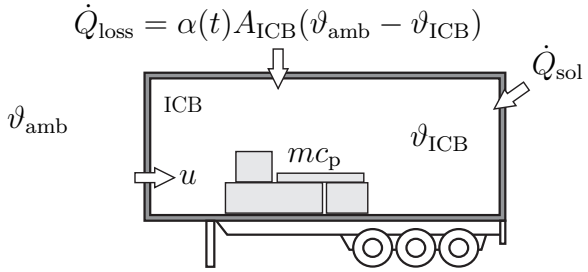

Figure 2.6: Model of the insulated cool box with refrigeration system.

The ICB model, eq. 2.20, can be rewritten as

$$\begin{aligned} mc_\mathrm{p}\frac{d\vartheta_\mathrm{ICB}}{dt} &= -u + \overbrace{\alpha_0 A_\mathrm{ICB}(\vartheta_\mathrm{amb} - \vartheta_\mathrm{ICB})}^{\dot{Q}_{\alpha_0}} \\ &+ \underbrace{\alpha_1(t)A_\mathrm{ICB}(\vartheta_\mathrm{amb} - \vartheta_\mathrm{ICB})}_{\dot{Q}_\alpha} + \dot{Q}_\mathrm{sol}, \end{aligned} \tag{2.21}$$

where α_0 is the known heat transfer coefficient of a new ICB and $\alpha_1(t)$ is the deterioration of α over time.
In eq. (2.21) the plant output is ϑ_ICB, the control variable is given by u, $\dot{Q}_{\alpha_0}$ is the heat input which arises by α_0, and the additional heat flow $\dot{Q}_\alpha$ depends on the deterioration of α. Typically only sensor signals for ϑ_ICB and ϑ_amb are available, and therefore the estimation of irradiation and deterioration of α is desirable. The total disturbance $\dot{Q}_z$ is defined as

$$\dot{Q}_z = \dot{Q}_\alpha + \dot{Q}_\mathrm{sol}. \tag{2.22}$$

However, both $\dot{Q}_\mathrm{sol}$ and $\dot{Q}_\alpha$ are simultaneously acting as an unknown disturbance $\dot{Q}_z$ with the same impact to the plant output and therefore cannot be separated by a standard disturbance observer. Nevertheless, $\dot{Q}_z$ can be estimated by a disturbance observer, and $\alpha(t)$ can be fit to $\dot{Q}_z$ using a parametric aging model. In consequence an estimate of $\dot{Q}_\alpha$ is available and $\dot{Q}_\mathrm{sol}$ can be reconstructed by $\dot{Q}_\mathrm{sol} = \dot{Q}_z - \dot{Q}_\alpha$.

The general plant's linear continuous-time dynamics are given by

$$\dot{x}_P = A_P x_P + B_P u + \boldsymbol{E}_P \boldsymbol{z},$$
$$y_P = C_P x_P + d_P u + \boldsymbol{F}_P^T \boldsymbol{z}, \tag{2.23}$$

where the input $u \in \mathbb{R}$ is the actual cooling capacity of the RS, the state and output of the plant $y_P = x_P = \vartheta_{\text{ICB}} \in \mathbb{R}$ is the actual temperature of return air of the ICB, and the disturbance $\boldsymbol{z} \in \mathbb{R}^2$ is typically constituted by ambient temperature ϑ_{amb} and irradiation $\dot{Q}_{\text{sol}}$. The coefficients $A_P \in \mathbb{R}, B_P \in \mathbb{R}, C_P = 1$ and $\boldsymbol{E}_P \in \mathbb{R}^{1\times 2}$ are the system-, input-, output- and disturbance coefficients, where $\boldsymbol{E}_P = \left[E_m, E_o\right]$ with the disturbance coefficient E_m of the measured disturbances and the disturbance coefficient E_o of the non measured disturbances, and $d_P \in \mathbb{R}, \boldsymbol{F}_P^T \in \mathbb{R}^{1\times 2}$ are the direct input-output gain and disturbance input vector. Note that in a thermodynamic system the input and the disturbance cannot affect the output instantaneously. Thus, $d_P = 0$ and $\boldsymbol{F}_P^T = \left[0, 0\right]$ hold in the plant model, eq. (2.23).

2.4.1 Composition of total disturbance

As seen in eq. (2.22) the heat inputs $\dot{Q}_\alpha$ and $\dot{Q}_{\text{sol}}$ have an additive effect on the measured output, where $\dot{Q}_\alpha$ is the heat input which arises by the deviation of α. The deviation of α is assumed to be very slow, therefore it can be seen as constant for the dynamics of the ICB on a short-term perspective, $\dot{Q}_{\text{sol}}$ changes very fast and during night time $\dot{Q}_{\text{sol}} \approx 0$. The knowledge of the different time constants enables to split up those two terms.

2.4.2 Model of α deterioration

For the life-cycle of the ICB the time-varying α is an important parameter. Over time the insulation of the ICB absorbs moisture, the increase of water content in the insulation material leads to an increase of α. The deterioration leads to a higher heat input and consequently the energy efficiency declines. Therefore, in long-term perspective the estimation of α is desirable.
In literature different models for deterioration of thermal insulation are discussed. In [29] different types of insulation panels and their aging over years are presented. A parametric model of the deterioration of α can be described as

$$\alpha(t) = \alpha_0 + f_\alpha(\boldsymbol{\theta}_\alpha, t), \tag{2.24}$$

where α_0 is the known heat transfer coefficient of a new ICB, $\boldsymbol{\theta}_\alpha$ are the unknown parameter of the α aging model and $f_\alpha(\boldsymbol{\theta}_\alpha, t)$ denotes the monotonously increasing deterioration.
The nonlinear model requires a complex optimization, nevertheless it describes the aging model more accurate than a linear model. Also other parametric aging models

can be used, e.g. different aging models depending on the type/operating conditions of the ICB are possible.

2.5 Combined Linear Dynamics

The combined linear dynamics of the RS and the ICB are defined in this Section. The previously derived models are combined into one linear state-space model of higher order and the already introduced static RS maps, Fig. 2.7.

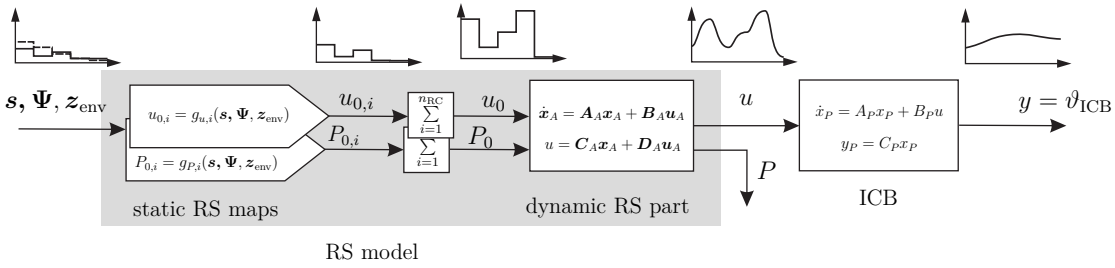

Figure 2.7: Combined dynamics of the RS and the ICB.

The combined dynamics of the RS and the ICB are described by the stacked state vector $\boldsymbol{x} = [\boldsymbol{x}_A^T \;\; x_P]^T$, and the corresponding state space system is given by

$$\begin{aligned} \dot{\boldsymbol{x}} &= \boldsymbol{A}\boldsymbol{x} + \boldsymbol{B}u_0 + \boldsymbol{E}\boldsymbol{z}, \\ \boldsymbol{y} &= \boldsymbol{C}\boldsymbol{x}, \end{aligned} \tag{2.25}$$

where $y = \vartheta_{\text{ICB}}$, and

$$\boldsymbol{A} = \begin{bmatrix} \boldsymbol{A}_A & 0 \\ B_P\boldsymbol{C}_A & A_P \end{bmatrix}, \quad \boldsymbol{B} = \begin{bmatrix} \boldsymbol{B}_A \\ 0 \end{bmatrix},$$

$$\boldsymbol{E} = \begin{bmatrix} \boldsymbol{0} \\ \boldsymbol{E}_P \end{bmatrix}, \quad \boldsymbol{C} = \begin{bmatrix} \boldsymbol{0} & C_P \end{bmatrix}.$$

The dynamics of the ICB are much slower than that of the RS. Depending on mc_{p}, it typically takes hours to cool down the ICB by 1°C. In contrast, the RS with compressor switching has to work at a higher frequency (typically one minute) to produce a desired cooling capacity.

Chapter 3

Numerically efficient control allocation

In this Chapter a strategy for a numerically efficient optimization for the CA problem is presented. This is achieved by solving the computationally most expensive part of the problem off-line and storing the result in look-up tables. The numerically efficient part of the optimization is made on-line. Therefore, important contradicting optimization goals such as power consumption, wear, disparity of operating hours between compressors, and the coefficient of performance (COP) can be considered. A hierarchic solution procedure for the above mentioned optimization goals is proposed. The solution procedure effectively eliminates ambiguity in the decision variables while respecting the system's constraints. The generic structure allows for application to RSs with any controller, multiple RCs and multiple compressors, regardless if the compressors are identical or not. The possibility to implement this strategy in an inexpensive micro-controller is an important advantage to methods where a complex mixed-integer optimization problem has to be solved on-line. The method and the results of this Chapter have been published in [42].

3.1 State of the art

One method of achieving higher efficiency of an RS is through cooling capacity control. Cooling capacity control methods commonly employed are optimal on-off control, hot gas bypass, suction pressure control, multiple compressor control and variable speed control. The most energy efficient method is the variable speed control and the multiple compressor strategy, [70].
Several studies have demonstrated the potential savings associated with the use of variable speed control. In [60] the potential electricity savings by using a variable speed compressor and a controller for air conditioning systems is shown. In [35] a feed-forward control for a variable speed refrigeration system is introduced. A PI controller manages the thermal capacity and superheat independently for saving energy and to improve

the COP.
An optimal on-off control strategy is developed in [34], based on the time domain analysis of the temperature variations. The strategy determines the optimal upper and lower temperature bounds by minimizing the temperature variations from the set-point, energy consumption and average compressor on-off cycling frequency. In [14] different on-off switching control methods are compared. It presents an on-off control method with low complexity and computational requirements. Based on a heuristic method, sub-optimal on-off control strategies for a chilled water cool storage system, where an optimal control problem is formulated to determine optimal control trajectories is developed in [30].
In [17] a comparison of different controllers for a variable speed compressor and an EXV is made. An example which utilizes the EXV as a continuous actuator for cooling capacity control is demonstrated in [105]. In [98] an EXV control-loop is used to achieve a reference superheat value.
Also multiple compressors in an RS are well known, which may be cycled on and off to vary the cooling capacity of the system. Depending on the load requirement the system increases or decreases the number of active compressors to match the system load changes, [64]. In [97] an optimal compressor operation for energy efficiency was developed. The objective was to minimize power consumption, provided that the total refrigeration load requirement was met. The optimization model is a simple static model, which integrates only the power and the cooling capacity. The paper presents only the formulation of the objective function, but gives no details about the implementation and results of the optimization. A linear programming model was developed to give the optimized operation for each compressor in the system.
Finding optimal solutions to nonlinear (hybrid) RSs with redundant components is a difficult and computationally extensive search problem. To solve this kind of problems mixed integer optimization is widely used, [7, 31]. With large latency time constraints it is necessary to solve an unit commitment problem, [83]. Furthermore, on-line implementation poses severe limitations on the use of optimal strategies and requires expensive hardware for successful implementation. Therefore, off-line optimization is advantageous.

3.2 Problem description

3.2.1 Closed-loop structure

Fig. 3.1 shows the structure of the closed-loop system. The topic of this Chapter is the gray optimization block, where the optimal discrete $\boldsymbol{\varrho}^\star$ (which compressors should run, etc.) and continuous $\boldsymbol{\Psi}^\star$ (valve position, fan speed, etc.) variables for the RCs are calculated such that the RS provides the cooling capacity $u \stackrel{!}{=} \dot{Q}_{\mathrm{req}}$. Solar radiation and deterioration of α is not considered in this Chapter. Depending on the deviation of the

ICB temperature ϑ_{ICB} from the ICB set temperature $\vartheta_{\mathrm{ICB}}^{\mathrm{ref}}$ a controller calculates the required cooling capacity $\dot{Q}_{\mathrm{req}}$. This controller can be a classical PI controller or also an MPC, [20]. The calculation of $\dot{Q}_{\mathrm{req}}$ is not part of this Chapter and can be implemented as shown in [32].

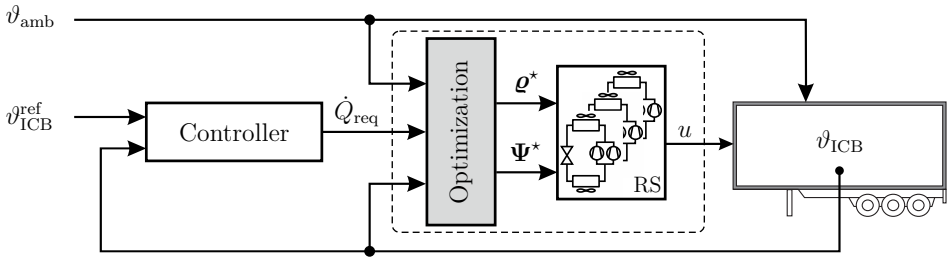

Figure 3.1: Closed-loop system with a controller, the optimization, the refrigeration system (RS) and the insulated cool box (ICB). The optimization block is the main part of this Chapter, where the optimal discrete $\boldsymbol{\varrho}^{\star}$ and continuous $\boldsymbol{\Psi}^{\star}$ variables for the RS are calculated.

3.2.2 Advantage over heuristic methods

Note that the redundancy of the RS defined in Fig. 3.1 enables supply of the same u using several different combinations of discrete and continuous decision variables, respectively. Hence, the choice of $\boldsymbol{\Psi}^{\star}$ and $\boldsymbol{\varrho}^{\star}$ is not unique.
Simple heuristics may resolve this fact, however, three main drawbacks will result: 1) optimality in the sense of minimum power consumption and wear or maximum COP cannot be guaranteed, 2) time-varying constraints will be difficult to consider, and 3) balancing trade-offs between optimization goals will be difficult if not impossible. Furthermore, practically important optimization goals are typically contradicting (e.g. minimizing just switching of compressors for reducing wear will lead to prolonged running in unfavorable operating points thus increasing power consumption), which makes finding a suitable trade-off even more complex.

3.2.3 Optimization problem and solution procedure

Hierarchical optimization

The main contribution of this Chapter is the optimization of the discrete decision variables $\boldsymbol{\varrho}$ (which compressors should run, etc.) and continuous decision variables $\boldsymbol{\Psi}$ (valve position, fan speed, etc.) of the RS for a given $\dot{Q}_{\mathrm{req}}$.
A hierarchic optimization is proposed, first determining the discrete decision variables $\boldsymbol{\varrho}$ and then maximizing COP using the look-up tables for the continuous decision variables

$\boldsymbol{\Psi}$. Note that the $\boldsymbol{\varrho}$ may be determined in a sequential optimization depending on the uniqueness of the solution, see Fig. 3.2.

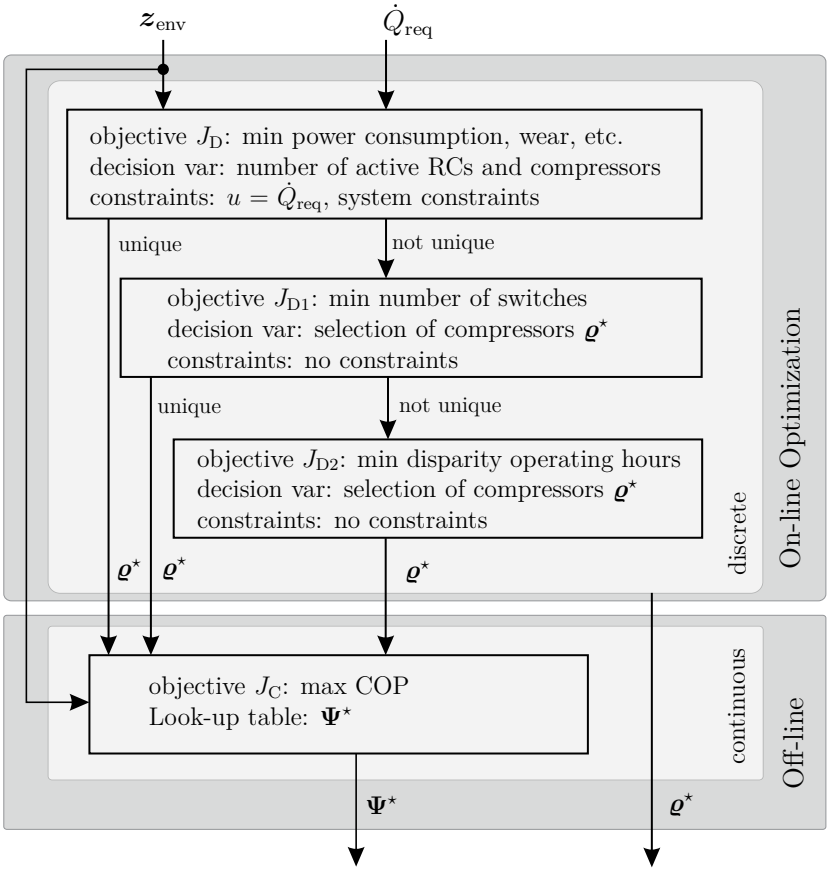

Figure 3.2: Solution procedure of the optimization. Once a discrete optimization leads to a unique solution the consecutive discrete optimizations can be skipped.

A necessary condition for the RS is posed by guaranteeing the required cooling capacity $u = \dot{Q}_{\text{req}}$. However, the redundant RCs lead to multiple solutions for providing $\dot{Q}_{\text{req}}$. This degree of freedom is used to fulfill different conflicting optimization goals J_{D}, such as minimizing the power consumption or the wear. This is the topmost goal for the optimization, it utilizes $\boldsymbol{\varrho}$ and considers $\boldsymbol{z}_{\text{env}}$ and all system constraints, eq. (2.13), see top box in Fig. 3.2.
Because of the redundant RCs the solution need not be unique in which case another optimization can be realized. The optimization goal J_{D1} is to minimize the number of switches, because it increases the wear of the compressors, see second from top box in Fig. 3.2. Consequently, life expectancy is optimized independent of the topmost optimization goal.
Again, this solution need not be unique, and another optimization can be made. This

optimization J_{D2} balances the operating hours of the compressors. As a result, no compressor is overly used, and wear is evenly distributed, see bottom box in the discrete optimization block of Fig. 3.2.
The optimization goals J_{D}, J_{D1} and J_{D2} are selected in the specified order because minimizing the power consumption is considered most important for industrial applications. Nevertheless, the order can be changed according to the requirements of the application.
After determining the discrete variables $\boldsymbol{\varrho}^{\star}$ the continuous variables $\boldsymbol{\Psi}^{\star}$ have to be set. Here the optimization goal J_{C} is to maximize COP under consideration of the system constraints, see bottom box in Fig. 3.2. With this optimization it can be guaranteed that all RCs work in the most effective operating point. This optimization is made off-line and the solution is saved in look-up tables.

Formal definition

A formal definition of the hierarchical optimization is given by the optimization of the discrete decision variables

$$\begin{aligned} \text{criterion}: \;& J_{\mathrm{D}}(\boldsymbol{\kappa}) = R_W \boldsymbol{W}(w_S \big| \boldsymbol{\kappa}) + R_P P + R_O J_{\mathrm{O}}, \\ \text{constraint}: \;& u(\boldsymbol{\kappa}) = \dot{Q}_{\mathrm{req}}. \end{aligned} \tag{3.1}$$

In eq. (3.1) $\boldsymbol{\kappa}$ is any permutation of active compressors that fulfills the constraint, $\boldsymbol{W}(w_S \big| \boldsymbol{\kappa})$ is the probability that some compressor switching is necessary, P is the electrical power consumption, J_{O} is some optional criterion, and R_W, R_P, R_O are suitable weighting factors. If the solution of J_{D} is not unique, it is augmented with further discrete optimizations

$$\text{criterion}: \; J_{\mathrm{D1}}(\boldsymbol{\varrho}) = c_l\,(\kappa^{\star}, \boldsymbol{\varrho}), \tag{3.2}$$

$$\text{criterion}: \; J_{\mathrm{D2}}(\boldsymbol{\varrho}) = H_l\,(\boldsymbol{\varrho}). \tag{3.3}$$

The criterion J_{D1} for minimal switching, eq. (3.2), depends on the solution to eq. (3.1) denoted by $\kappa^{\star}$, and c_l is the number of compressor switches necessary to obtain a new combination l of active compressors denoted by $\boldsymbol{\varrho}$. If this solution is still not unique, criterion J_{D2}, eq. (3.3), is evaluated, where the disparity of operating hours in the compressors H_l is minimized.
In a last step the optimal continuous decision variables are set using the look-up table. Note that J_{D} and J_{C} are always executed while J_{D1} and J_{D2} are optional goals only available if more redundant decision variables exist, see also Fig. 3.2.

3.3 On-line optimization of discrete variables

3.3.1 Fundamental procedure

The optimization of the mode selection can be divided into independent optimization goals, allowing to solve the optimization problems independently. The overall target is to determine the best permutation with the index $\kappa^\star$. If the permutation has been fixed the next decision is made, which compressor combination $\boldsymbol{\varrho}^\star$ should represent $\kappa^\star$. The optimizations presented in this Section correspond to the three boxes contained in the discrete optimization block in Fig. 3.2.
Note that the optimization of the discrete variables depends on the past decisions and has to be solved on-line. However, the optimization of the discrete variables is independent of high computational costs and can be calculated on an inexpensive micro controller.

3.3.2 Optimization of the permutation

The topmost box in Fig. 3.2 corresponds to the following optimization. If the desired cooling capacity $\dot{Q}_{\mathrm{req}}$ can be provided by different permutations, it is possible to optimize the choice of permutation. The main targets for an RS are minimizing the wear and minimizing the power consumption.
The cost function to be minimized is

$$J_{\mathrm{D}} = R_W \cdot J_{\mathrm{W}} + R_P \cdot J_{\mathrm{P}} + R_O \cdot J_{\mathrm{O}}, \tag{3.4}$$

with J_{W} and J_{E} the cost functions for the wear and the power consumption and J_{O} for other criteria. The weighting factors R_W, R_P, R_O in the cost function constitute the flexibility of the approach to meet different requirements.
The best permutation $\kappa^\star$ is given by the corresponding optimization problem

$$\kappa^\star = \arg\left[\min_{\boldsymbol{\kappa}}(J_{\mathrm{D}})\right] \tag{3.5}$$

s.t.

$$\delta_{\mathrm{eq}}(\boldsymbol{\Psi}) = u(\boldsymbol{\Psi}) - \dot{Q}_{\mathrm{req}} = 0, \tag{3.6}$$

with $\kappa^\star$ the best permutation of the set of possible permutations $\boldsymbol{\kappa}$, eq. (2.16). The hard constraint in eq. (3.6) can also be formulated as soft constraint. This ensures that a valid solution can always be found.

Minimizing wear

Mostly the wear depends on the on-off cycling of the compressors, therefore, the number of cycles has to be minimized. The decision of $\kappa^\star$ is made with the probability distribution of operating points. The appropriate probability density function $p(u)$, which

can be varying by time, location, season, etc. is used to define the best permutation. The shape of $p(u)$ can be based on historical data. It is possible to use data from service memory to generate the statistics about the probability distribution of operating points. The method is demonstrated in Fig. 3.3.

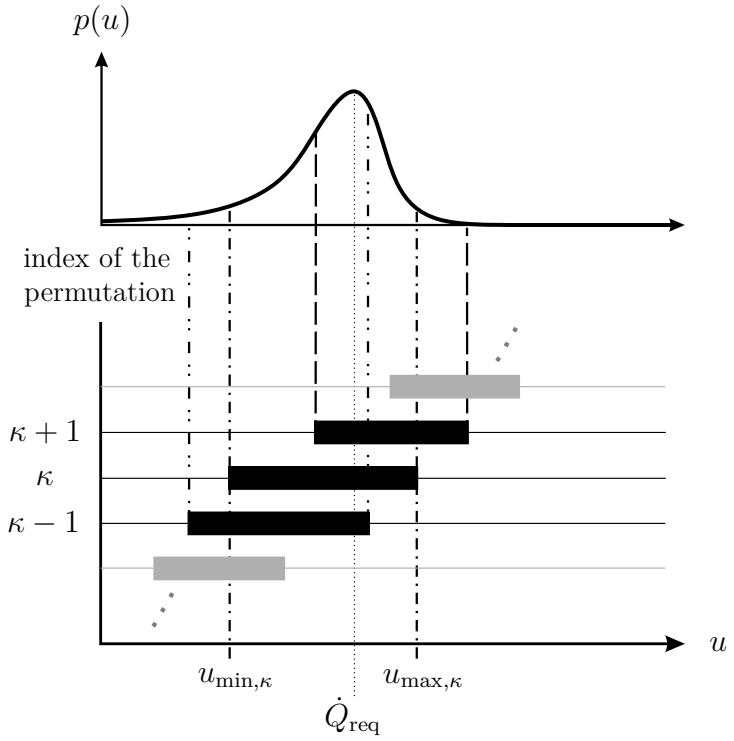

Figure 3.3: Probability density function, describing the operating point probability $p(u)$, with the permutations and cooling capacity ranges for one operating point with constant environmental conditions $\boldsymbol{z}_{\text{env}}$. Three different permutation indices ($\kappa - 1$, κ and $\kappa + 1$) can provide the required cooling capacity $\dot{Q}_{\text{req}}$. To minimize the wear, the permutation index κ is used.

The switching probability $\boldsymbol{W}(w_S|\boldsymbol{\kappa})$ of the permutation set $\boldsymbol{\kappa}$ defines the probability that a permutation has to change if the cooling capacity is varying. The switching probability $W_\kappa(w_S|\boldsymbol{\kappa})$ of κ is defined as

$$W_\kappa(w_S|\boldsymbol{\kappa}) = \int_{-\infty}^{u_{\min,\kappa}} p(u)\,\mathrm{du} + \int_{u_{\max,\kappa}}^{+\infty} p(u)\,\mathrm{du}. \tag{3.7}$$

where S is the switching event and with $u_{\min,\kappa}$ and $u_{\max,\kappa}$ as the left and right edge of the cooling capacity range of the permutation with index κ. The switching probability

$\boldsymbol{W}(w_S\big|\boldsymbol{\kappa})$ can be formulated as

$$\boldsymbol{W}(w_S\big|\boldsymbol{\kappa}) = \{W_\kappa(w_S|\boldsymbol{\kappa}) \in \boldsymbol{\kappa}\}. \tag{3.8}$$

The permutation index $\kappa^\star$ with the minimal switching probability is utilized to provide the cooling capacity.
The cost function to be minimized is

$$J_\mathrm{W} = \boldsymbol{W}(w_S\big|\boldsymbol{\kappa}). \tag{3.9}$$

The corresponding optimization problem is formally stated as

$$\kappa^\star = \arg\Big[\min_{\boldsymbol{\kappa}}(J_\mathrm{W})\Big]. \tag{3.10}$$

After choosing the best permutation, the permutation is active until it cannot provide the desired cooling capacity $\dot{Q}_\mathrm{req}$ any more.

Minimizing power consumption

To minimize the power consumption the electrical power should be minimized. Therefore, the permutation which leads to the minimal electrical power is used. The cost function to be minimized is

$$J_\mathrm{P} = P. \tag{3.11}$$

The corresponding optimization problem is formally stated as

$$\kappa^\star = \arg\Big[\min_{\boldsymbol{\kappa}}(J_\mathrm{P})\Big]. \tag{3.12}$$

In the case of using an internal combustion engine (ICE) as primary source, minimizing the brake specific fuel consumption is an important aspect. A specific fuel consumption map, can be considered in the optimization problem to decide which permutation achieves the lowest brake specific fuel consumption. Another criteria of using an ICE can be to minimizing the noise impact.

Other criteria

If there are other criteria which also should be optimized, they can be implemented with J_O to be also considered in the optimization problem, eq. (3.5).
For example if the set point often changes, an optimization of the control settling time t_cst can be made. The t_cst is defined as the time required for ϑ_ICB to slew to the vicinity of the final value $\vartheta_\mathrm{ICB}^\mathrm{ref}$ determined by a range of certain percentage of the final value.
The cost function to be minimized is

$$J_\mathrm{o} = t_\mathrm{cst}. \tag{3.13}$$

3.3.3 Optimization of the compressor combination

Minimizing compressor switching $\boldsymbol{c}$

This optional optimization is depicted in Fig. 3.2 in the second box from the top. After the selection of the best permutation, the decision which compressors should represent the permutation have to be made. Out of all possible compressor combinations a subset $\boldsymbol{\varrho}_{\text{act}}$ which fulfill the required $\kappa^\star$ is selected. To compute the number of compressor switching $\boldsymbol{c}$ the compressor states $\boldsymbol{s}$ which is currently active is used. If the current compressor combination can still be used, no switching is necessary and the current compressor combination remains, $\boldsymbol{\varrho}^\star = \boldsymbol{s}$. If switching is necessary the compressor combination which requires minimal switches has to be found. The compressor switching c_l is calculated by

$$c_l = \sum \left| \boldsymbol{s} - \boldsymbol{\varrho}_{\text{act},l} \right|, \tag{3.14}$$

with l the index of the subset $\boldsymbol{\varrho}_{\text{act}}$. The compressor switching of all $\boldsymbol{\varrho}_{\text{act}}$ is given by

$$\boldsymbol{c} = \begin{bmatrix} c_1 & c_2 & \dots & c_{n_l} \end{bmatrix}^T. \tag{3.15}$$

where n_l is the number of all compressor combinations in the subset $\boldsymbol{\varrho}_{\text{act}}$.
The cost function to be minimized is

$$J_{\text{D1}} = c_l. \tag{3.16}$$

The corresponding optimization problem is formally stated as (index of the smallest element of $\boldsymbol{c}$)

$$\boldsymbol{\varrho}^\star = \boldsymbol{\varrho}_{\text{act}} \left(\text{index} \left\| \frac{1}{\boldsymbol{c}} \right\|_\infty \right). \tag{3.17}$$

If the solution is unique the best compressor combination $\boldsymbol{\varrho}^\star$ is found. If there are more compressor combinations with the same minimal count of switching a further optimization problem is solved. The optimization goal is to balance the operating hours of the compressors, which is described in the next section.

Minimizing disparity of operating hours $\boldsymbol{h}$

The last potential optimization of discrete decision variables is also depicted in Fig. 3.2 as the bottom box in the discrete optimization block. The hours of operation of the compressor j is calculated by

$$h_{i,j} = \sum \int_0^t f_h(s,t)\, \mathrm{d}t, \tag{3.18}$$

with

$$f_h = \begin{cases} 1 & \text{if } s_{i,j} = 1 \\ 0 & \text{else} \end{cases}. \tag{3.19}$$

The operating hours of all compressors of the RS are collected in the vector $\boldsymbol{h}$,

$$\boldsymbol{h} = \begin{bmatrix} h_{1,1} & \dots & h_{1,n_1} & \dots & h_{n_{RC},n_{n_{RC}}} \end{bmatrix}^T. \tag{3.20}$$

The sum of the operating hours $\boldsymbol{H}$ of the active compressors is calculated by,

$$\boldsymbol{H} = \boldsymbol{\varrho}_{\text{act}}\, \boldsymbol{h}, \tag{3.21}$$

where $\boldsymbol{\varrho}_{\text{act}}$ are only the compressor combinations with minimal compressor switching, $\boldsymbol{\varrho}^\star$ of eq. (3.17), which ensures minimal count of switching. The cost function J_{D2} to be minimized is

$$J_{\text{D2}} = H_l, \tag{3.22}$$

with l the index of the subset $\boldsymbol{\varrho}_{\text{act}}$. The corresponding optimization problem is formally stated as (index of the smallest element of $\boldsymbol{H}$)

$$\boldsymbol{\varrho}^\star = \boldsymbol{\varrho}_{\text{act}}\left(\text{index}\left\|\frac{1}{\boldsymbol{H}}\right\|_\infty\right). \tag{3.23}$$

3.4 Off-line computation of continuous variables

The optimization of the continuous variables, bottom box in Fig. 3.2, is made based on the COP,

$$\text{COP}\ (\boldsymbol{\Psi}, \boldsymbol{z}_{\text{env}}) = \frac{u(\boldsymbol{\Psi}, \boldsymbol{z}_{\text{env}})}{P(\boldsymbol{\Psi}, \boldsymbol{z}_{\text{env}})}. \tag{3.24}$$

Different $\boldsymbol{\Psi}$ lead to the same cooling capacity but with different COP. To optimize $\boldsymbol{\Psi}$ the value with the maximal COP is utilized.
To find the best $\boldsymbol{\Psi}^\star$ a constraint optimization problem is formulated. The equality constraint is to guarantee $\dot{Q}_{\text{req}}$ and the inequality constraints make sure that the solution is found in the feasible range of $\boldsymbol{\Psi}$.
The cost function to be maximized is

$$J_{\text{C}} = \text{COP}\ (\boldsymbol{\Psi}, \boldsymbol{z}_{\text{env}}). \tag{3.25}$$

The corresponding optimization problem is formally stated as

$$\begin{aligned} \boldsymbol{\Psi}^\star &= \arg\Big[\max_{\boldsymbol{\Psi}\,\in\,\chi_{\text{ar}}} (J_{\text{C}})\Big] \\ \text{s. t.} & \\ \delta_{\text{eq}}(\boldsymbol{\Psi}) &= 0 \\ \boldsymbol{\delta}_{\text{ineq}}(\boldsymbol{\Psi}) &\leq \mathbf{0}, \end{aligned} \tag{3.26}$$

with

$$\delta_{\text{eq}}(\boldsymbol{\Psi}) = u(\boldsymbol{\Psi}) - \dot{Q}_{\text{req}}, \tag{3.27}$$

$$\boldsymbol{\delta}_{\text{ineq}}(\boldsymbol{\Psi}) = \begin{bmatrix} \boldsymbol{v}_{\min} & - & \boldsymbol{v} \\ \boldsymbol{v} & - & \boldsymbol{v}_{\max} \\ \boldsymbol{\omega}_{\text{FC}} & - & \boldsymbol{\omega}_{\text{FC,max}} \\ \boldsymbol{\omega}_{\text{FE}} & - & \boldsymbol{\omega}_{\text{FE,max}} \\ \boldsymbol{\omega} & - & \boldsymbol{\omega}_{\max} \end{bmatrix}, \tag{3.28}$$

and

$$\begin{aligned} \chi_{\text{ar}} = \{ \quad v_i \in \mathbb{R}_0^+ : \quad & v_i \geq v_{\min,i} \; ; \; v_i \leq v_{\max,i} \\ \omega_{\text{FC},i} \in \mathbb{R}_0^+ : \quad & \omega_{\text{FC},i} \leq \omega_{\text{FC,max},i}, \\ \omega_{\text{FE},i} \in \mathbb{R}_0^+ : \quad & \omega_{\text{FE},i} \leq \omega_{\text{FE,max},i}, \\ \omega_i \in \mathbb{R}_0^+ : \quad & \omega_i \leq \omega_{\max,i} \quad \}, \end{aligned} \tag{3.29}$$

It can be seen that the dimension of $\boldsymbol{\Psi}$ depends on the number of active RCs.
The optimization problem can be solved with Lagrange multiplier μ_{eq} and $\boldsymbol{\mu}_{\text{ineq}}$, [9]:

$$\mathcal{L}(\boldsymbol{\Psi}, \mu_{\text{eq}}, \boldsymbol{\mu}_{\text{ineq}}) = f_{\boldsymbol{\Psi}}(\boldsymbol{\Psi}) + \mu_{\text{eq}}\delta_{\text{eq}}(\boldsymbol{\Psi}) + \boldsymbol{\mu}_{\text{ineq}}^T\boldsymbol{\delta}_{\text{ineq}}(\boldsymbol{\Psi}) \tag{3.30}$$

$$\begin{aligned} & \text{s.t.} \\ \nabla f_{\boldsymbol{\Psi}}(\boldsymbol{\Psi}^\star) + \nabla\delta_{\text{eq}}(\boldsymbol{\Psi}^\star)\mu_{\text{eq}}^\star + \nabla\boldsymbol{\delta}_{\text{ineq}}(\boldsymbol{\Psi}^\star)\boldsymbol{\mu}_{\text{ineq}}^\star &= 0 \\ \boldsymbol{\mu}_{\text{ineq}}^\star &\geq 0 \\ \boldsymbol{\delta}_{\text{ineq}}^T(\boldsymbol{\Psi}^\star)\boldsymbol{\mu}_{\text{ineq}}^\star &= 0 \\ \boldsymbol{\delta}_{\text{ineq}}(\boldsymbol{\Psi}^\star) &\leq 0 \end{aligned}$$

The optimization of $\boldsymbol{\Psi}^\star$ requires high computational costs. Therefore, the optimization problem is solved off-line by a calculation over the whole operating envelope. The solution $\boldsymbol{\Psi}^\star$ is saved in look-up tables, these can be easily stored in the memory of a micro controller. The input variables from the look-up tables are the measurable environmental conditions $\boldsymbol{z}_{\text{env}}$, the best permutation $\kappa^\star$ and the desired cooling capacity $\dot{Q}_{\text{req}}$.

3.5 Illustrative example

The illustrative example utilizes an RS which includes three RCs each with two compressors all with identical capacity, Fig. 3.4. To facilitate the explanations, further assumptions are made. All compressors are single speed compressors with the same capacity. The fan speeds of the condenser and the evaporator have only one fixed speed. Therefore, eq. (2.6) is reduced to $\Psi_i = [v_i]$ and the decision vector for all RCs, eq. (2.7), is $\boldsymbol{\Psi} = [v_1 \;\; v_2 \;\; v_3]$.
Fig. 3.5 shows two diagrams of the operating hours $\boldsymbol{h}$ for all compressors. The left diagram shows the current states of the compressors $\boldsymbol{s}$, the right diagram shows the new compressor combination $\boldsymbol{\varrho}^\star$ under consideration of the optimization criteria.

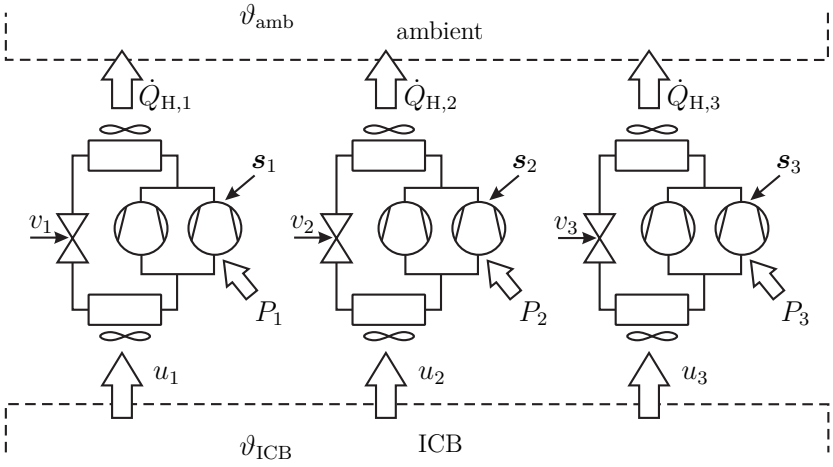

Figure 3.4: The structure of the refrigeration system with three RCs, each with two compressors.

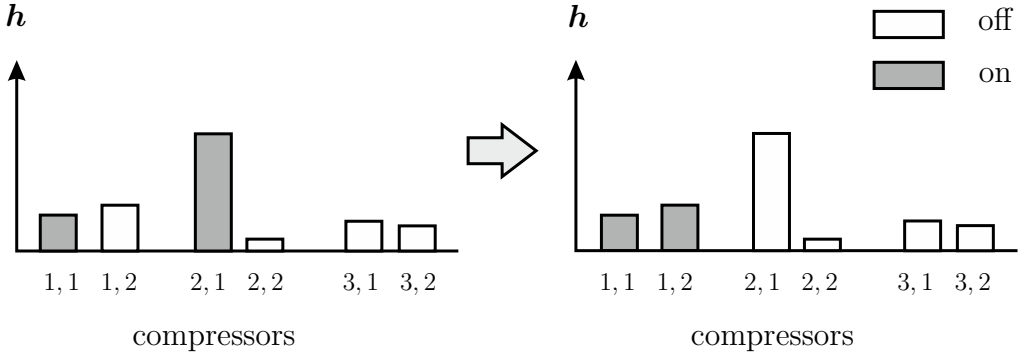

Figure 3.5: Best solution for minimizing compressor switching and disparity of operating hours. White bars denote compressors which are off, gray bars demonstrate compressors which are active.

Assumed $\dot{Q}_{\text{req}}$ can be realized by the permutation indices $\boldsymbol{\kappa} = \{2, 3\}$, eq. (2.16), where for example $\kappa = 2$ means one RC with two compressors is active and $\kappa = 3$ means two RCs are active, one with two compressor and the other one with only one compressor. Assumed that P should be minimized ($J_{\text{D}} = J_{\text{E}}$), eq. (3.4), and $P^2 < P^3$, where P^κ defines the electrical power of the permutation with index κ.
With $\kappa^\star = 2$, eq. (3.5), the possible compressor combinations are

$$\boldsymbol{\varrho}_{\text{act}} = \begin{bmatrix} 1 & 1 & 0 & 0 & 0 & 0 \\ 0 & 0 & 1 & 1 & 0 & 0 \\ 0 & 0 & 0 & 0 & 1 & 1 \end{bmatrix}.$$

Assumed that the state vector, Fig. 3.5, is

$$\boldsymbol{s} = \begin{bmatrix} 1 & 0 & 1 & 0 & 0 & 0 \end{bmatrix}.$$

Thus it appears that the compressor switching $\boldsymbol{c} = [2 \;\; 2 \;\; 4]^T$, (criterion J_{D1}). It can be seen that the first two compressor combinations of $\boldsymbol{\varrho}_{\mathrm{act}}$ need the minimum possible compressor switches,

$$\boldsymbol{\varrho}^{\star} = \begin{bmatrix} 1 & 1 & 0 & 0 & 0 & 0 \\ 0 & 0 & 1 & 1 & 0 & 0 \end{bmatrix}.$$

Therefore, $\boldsymbol{\varrho}^{\star}$ is not unique and the new combination is chosen such that the disparity of operating hours is minimized, (criterion J_{D2}).
Assumed the operating hours of all compressors are defined by

$$\boldsymbol{h} = \begin{bmatrix} 1.75 & 2 & 5 & 0.5 & 1.25 & 1 \end{bmatrix},$$

with eq. (3.20) and eq. (3.23) leads to $\boldsymbol{H} = [3.75 \;\; 5.5]^T$.
In the first compressor combination the sum of the operating hours of all active compressors $\boldsymbol{H}$ is smaller than the second one, therefore, the first combination is selected (criterion J_{D2}),

$$\boldsymbol{\varrho}^{\star} = \begin{bmatrix} 1 & 1 & 0 & 0 & 0 & 0 \end{bmatrix}.$$

With the assumption $v_1^{\star} = 0.3$ the optimal continuous decision vector, (criterion J_{C}), is defined $\boldsymbol{\Psi}^{\star} = [0.3 \;\; 0 \;\; 0]$.
The combination [0 0 0 0 1 1] in fact, would have the smallest operating hours ($H = 2.25$) but needs four compressor switches (compressors one and three have to be turned off and compressor five and six have to be turned on. Therefore, it is not an option for the optimization J_{D2}.

3.6 Simulation results

The simulation results are demonstrated with the same RS which is already mentioned, at the beginning of Section 3.5. All simulation results have been published in [42].

3.6.1 Comparing conventional control method with optimized method

This example shows the advantage of using redundant RCs with multiple compressors and continuous decision variables in comparison to the conventional on-off method with no continuous decision variables.

Effect of redundant compressors

Fig. 3.6 shows the conventional temperature control, method A. The RS consists of one RC with one large compressor. For a suitable comparison, it is assumed that the RC with one compressor provides the same cooling capacity as the RCs with all six compressors active.

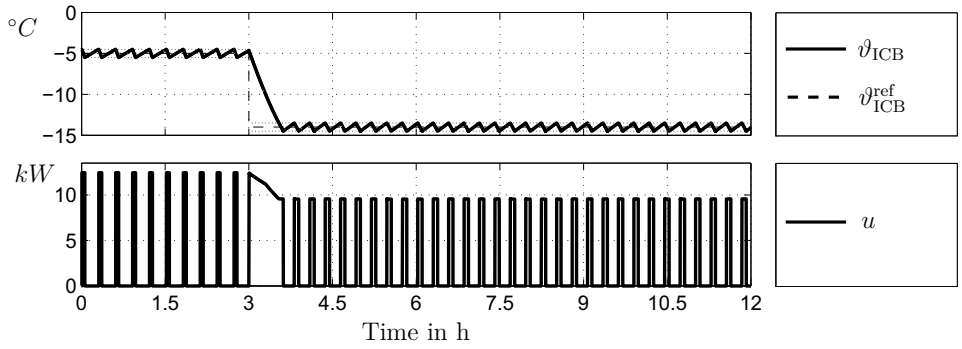

Figure 3.6: Method A: Conventional method with one compressor leads to a high compressor switching frequency.

In Fig 3.7 the RS consists of three RCs each with two compressors but no continuous decision variables, method B.

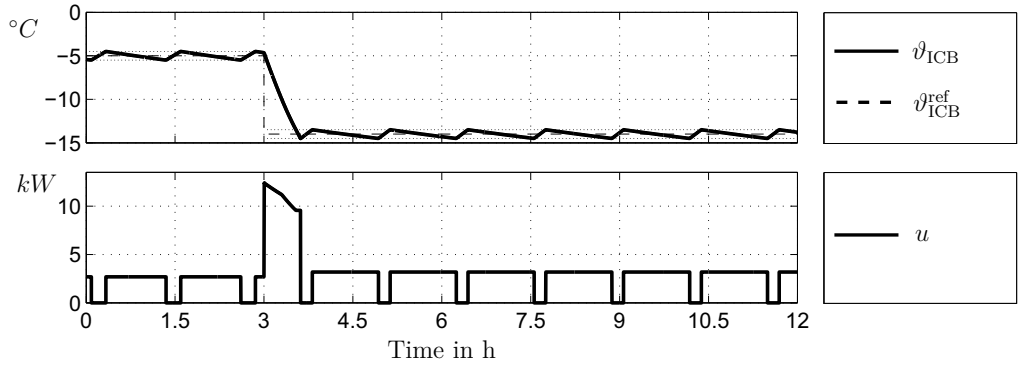

Figure 3.7: Method B: With multiple RCs and compressors the temperature gradients during the cooling process are smaller and the switching frequency is significantly reduced.

It can be seen that a cooling capacity closer to the demand value can be delivered. As a result, the compressor switching frequency is considerably reduced, because of more but smaller compressors, which leads to a finer discretization.
Note that right after the ICB temperature step the maximum available u is time-varying due to the decreasing ICB temperature.

Balancing of optimization goals

With the cost function

$$J_{\mathrm{D}} = R_W \cdot J_{\mathrm{W}} + (1 - R_W) \cdot J_{\mathrm{O}}, \tag{3.31}$$

a balancing between minimizing compressor switching and the control settling time can be achieved.

In Fig. 3.8, method C, it can be seen that only optimizing the compressor switching ($R_W = 1$) is not effective for a step change in ϑ_{ICB}. This leads to no switching and just variation of the continuous decision variables but causes only a small achievable gradient in ϑ_{ICB}. Therefore, an excessively long time is necessary to achieve the new set temperature. A mixed optimization of minimizing compressor switching and the control settling time achieves an equally fast time-performance with slight performance loss in minimizing compressor switching. In Fig. 3.8 it can also be seen that minimizing only the control settling time ($R_W = 0$) leads to a a high cooling power demand and more compressor switches.

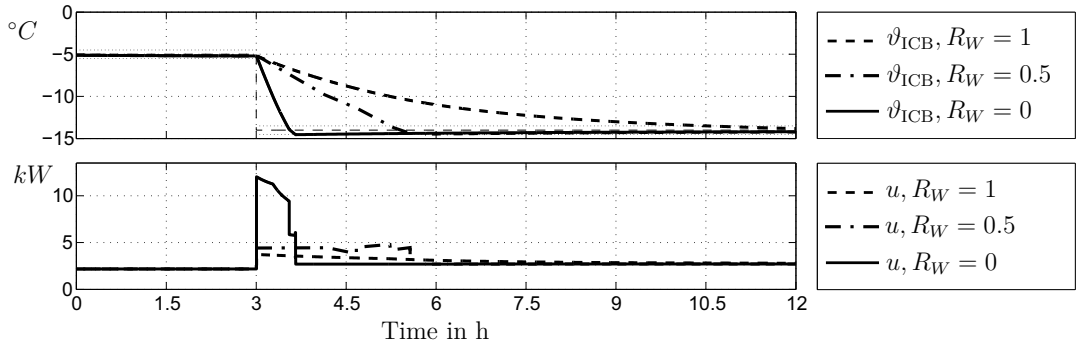

Figure 3.8: Method C: Different weighting factors between minimizing compressor switching and time-performance.

Table 3.1 shows the relevant values for the different methods. These are the total consumed energy E over the whole simulation span of 12 h, the average cooling capacity $\overline{u}$ and the control settling time t_{cst}. It can be seen that with the proposed method the life cycle costs can be reduced. The number of switches is reduced significantly. Compared with the conventional method savings of more than 12 % are possible.

Method	A	B	C	C	C
Fig.	3.6	3.7	3.8	3.8	3.8
R_W	-	-	1	0.5	0
n_c	1	6	6	6	6
# Switches	83	43	1	3	9
$\mathrm{COP}/\mathrm{COP}_{\mathrm{B}}$	1.02	1	0.93	0.92	0.96
E/E_B	1.04	1	0.9	0.92	0.97
$\overline{u}/\overline{u}_B$	1.02	1	0.97	1.003	1.02
$t_{\mathrm{cst}}/t_{\mathrm{cst,B}}$	1	1	17.73	4.14	0.976

Table 3.1: All relevant reference values, normalized by the values of the second column (method B), denoted by $_{\mathrm{B}}$.

3.6.2 Power consumption versus switching

This example shows a special case where it can be seen that minimizing only the electrical power can lead to poor performance. In this simulation $\dot{Q}_{\text{req}}$ is a time-varying trajectory (e.g. due to external disturbances).

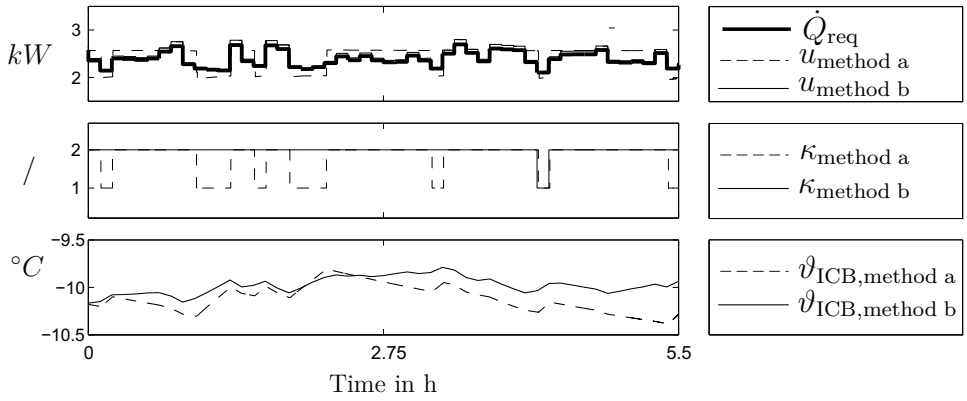

Figure 3.9: Minimizing power consumption (dashed line), method a, versus compressor switching (line), method b. Second plot: $\kappa = 1$: one compressor active, $\kappa = 2$: two compressors in one RC active.

Minimizing the compressor switching (method b), the variability can be managed most of the time by just varying a continuous decision variable. However, if only the electrical power is minimized (method a), one compressor is switched off every time the desired cooling capacity can be provided by a combination with smaller electrical power consumption. This also leads to a worse COP because the RC cannot work in the optimal operating point. In the first plot of Fig. 3.9 the cooling capacities of both methods are shown, $\dot{Q}_{\text{req}}$ is plotted for both methods. The second plot shows the permutations (a change represents switching) and the third plot shows the ICB temperature.
Table 3.2 shows the relevant values. These are the number of switching, E over the whole simulation span of 5.5 h, $\overline{u}$ and the root-mean-squared error (RMSE),

$$\text{RMSE} = \sqrt{\frac{1}{N}\sum_{k=1}^{N}(\dot{Q}_{\text{req}}(k) - u(k))^2},$$

with N the simulation time and k the index of the simulation time. It can be seen that minimizing the electrical power causes only small energy savings but the number of switches is significantly increased. From Table 3.2 it is clear that a combination of both criteria will deliver a good compromise.

Method	a	b
# Switches	13	2
$\mathrm{COP}/\mathrm{COP_b}$	0.97	1
E/E_b	0.94	1
$\overline{u}/\overline{u}_b$	0.98	1
RMSE	0.18	0.06

Table 3.2: Relevant reference values, normalized with the values of the second column, (method b), denoted by $_\mathrm{b}$.

3.7 Summary

The overall goal of the presented optimization is providing a desired cooling capacity $u = \dot{Q}_{\mathrm{req}}$ while optimizing several conflicting goals. Because of the redundant system, such conflicting goals can be achieved as minimizing power consumption and wear (represented by switching instances) while maximizing COP and disparity the operating hours of the compressors. The optimization reliefs the operator from heuristically choosing operating variables from a multitude of possible operation modes caused by the redundant components.
In contrast to existing on-line optimization methods the computationally expensive part can be done off-line. Thus, only the storage of the solution in simple look-up tables is necessary. It is therefore perfectly suited for implementation in a micro-controller based control unit of an industrial refrigeration system.
Due to the hierarchic structure the topmost optimization is always performed, ensuring an optimal compromise between power consumption, wear, and other possible goals. The outcome of the optimization can be easily shifted by the user towards one or the other goal by simple scalar weighting factors.
Simulation results show that the proposed method yields similar or even better performance (measured as settling time after a step in set point temperature) as conventional operating strategies while drastically reducing switching of the compressors and consuming less energy. Another result demonstrates the ability to achieve almost the same performance for tracking a time-varying $\dot{Q}_{\mathrm{req}}$ (measured as root mean square error between u and $\dot{Q}_{\mathrm{req}}$ and also in terms of power consumption) while reducing the switching instances to less than a sixth.

Chapter 4

Hierarchical model predictive control

Temperature control of an ICB can be efficiently provided by model predictive control. The design of MPC temperature control completes the overall control concept introduced in Chapter 3. In this Chapter a hierarchical MPC for temperature control is combined with two alternative predictive CA methods for the RS. However, if the cooling capacity u is supplied by redundant RCs with both continuous and switched control variables, the overall control design becomes complex: 1) Time constants of the ICB and RCs differ by a factor of approximately 100. 2) Switched and continuous control variables require mixed-integer optimization. 3) Power consumption, wear, control performance and output tracking call for multi-objective optimization.

4.1 State of the art

The theory of linear MPC can be considered mature, [10]. In the last few years, the application of MPC for energy management in buildings, heating, ventilation, and air conditioning (HVAC) systems and supermarket RS has received significant attention from the research community. In [84] an MPC formulation framework is defined and the outcomes of different existing MPC algorithms for building and HVAC system management is critically discussed. An MPC for a large temperature difference refrigerating station with ice cold thermal energy storage is developed in [15]. The optimization problem is solved with a nonlinear dynamic optimization algorithm based on neural networks and compared to a PID controller. A stochastic MPC of a air conditioning (AC) system is proposed in [23], where three control approaches are compared.
Several different solutions exist for a mixed integer MPC (MI-MPC) as the CA of the RCs. Approaches based on exact methods have been used, such as dynamic programming, [88], mixed-integer programming, [49], Lagrangian relaxation, [91], and branch and bound methods, [50]. The main drawbacks of these techniques are the large computational time and memory requirements for large complexity and dimensionality

problems. More recently, several meta-heuristic methods, such as simulated annealing, [86], evolutionary programming, [72], particle swarm optimization, [104] and genetic algorithms, [79] have been proposed. For further discussion and comparison of these methodologies, with special focus on meta-heuristic methods, see [78]. One drawback of heuristics is that they typically lack information on the quality of the found solutions compared to the global optimal solution. In [87] a sub-optimal MPC approach for handling both switched and continuous control has been proposed. The MI-MPC was not directly tackled, instead, a separation into logical variables with an ad hoc control design and continuous variables for the MPC was done.
In [7] a framework for hybrid systems is proposed. The optimization problem is defined as a mixed integer quadratic programming (MIQP) problem. One disadvantage of this formulation is that it is computationally complex. A framework which uses a simpler set of quadratic programming problems instead of the MIQP problem is presented in [54]. However, the problem of vastly differing time constants is not covered in these publications. A review of a number of decentralized, distributed and hierarchical control architectures for large-scale systems can be found in [80].
Early applications of hybrid MPC to supermarket refrigeration systems can be found in [32] and [89]. Whereas in [32] a mixed logical dynamic plant formulation is directly utilized in the MPC design, a high-level nonlinear MPC in combination with a low-level process control is proposed in [89]. A general approach to MPC for hybrid systems is given in [11], where a piece-wise affine model for the hybrid system is proposed. The application to a solar AC plant demonstrates that the hybrid MPC optimally switches between operating modes and computes the continuous control variables. In [85] an MPC for hybrid thermal systems in transport refrigeration is presented. It is shown that MPC can be successfully utilized for hybrid systems with both switched and continuous control variables. In [26] different MPC variants are designed for an automotive air-conditioning/refrigeration system, and it is shown that an adaptive hybrid MPC is the best performing concept.
Solutions similar to the proposed hierarchical MPC control structure have been published in [16], where a mixed-integer linear programming (MILP) and an MPC is used for optimal control of HVAC system, in [52] for a AC system, and [90, 61, 53, 16], where building heating and cooling control are provided by a similar control structure. However, in [52] the upper layer is an open loop controller which optimizes the energy cost of the AC system and the lower layer is a MPC which is in charge of tracking the tradeoff steady state calculated by the upper layer. In [90] only simple PI-controllers have been considered in the lower hierarchical level, in [61] binary variables have been approximated by continuous variables (resulting in a classical MPC problem), in [53] hierarchical MPCs solve for continuous control variables only at identical sampling times, and in [49] also identical sampling times apply at both layers although the hierarchical structure is similar to the concept proposed here. In [49, 61, 53, 41] identical sampling frequencies are used, thus strongly simplifying the communication, and no results on stability are included. In [41] the idea of different horizon lengths is also used and

recursive feasibility is proven. However, the lower-level MPC only solves a continuous optimization problem, and redundant supplies are not considered. In [16] an MPC-MILP control scheme for HVAC control was presented. Redundant components in the RS are considered, but all layers communicate with the same sampling frequency and stability is not considered. A decentralized control structure can also be implemented for redundant RCs, [56].
A theoretical work leading to a different strategy is given in [81]. On both levels robust MPCs with different sampling rates are employed, where the high-level MPC provides not only control variables but also admissible deviations to retain stability and performance. In contrast to that approach, in the proposed solution the high-level MPC has a simple linear structure and stability is guaranteed only by constraints on the switching action of the underlying CA. In an extension [69], the concept is adapted for independent systems with joint constraints, which would be applicable to the CA for the redundant RCs. In [102] a similar framework is presented, but it is again limited to a continuous optimization in the lower-level MPC.

4.2 Hierarchical control concept

Because of the vastly differing time constants the optimization problem is separated into two layers: The global MPC optimizes the temperature control of the slowly acting linear ICB system with a large sampling time T_s (samples denoted by K). The CA computes the fast acting input variables of the RS with a small sampling time t_s (samples denoted by k), and the integer ratio is defined as $\lambda = \frac{T_s}{t_s}, \lambda \in \mathbb{N}$. Hence, a multi-sampling rate control results, where the upper-level controller runs at a lower sampling frequency, [4].
The global MPC utilizes long prediction N_p and control N_c horizons, respectively. In general $N_\mathrm{p} > N_\mathrm{c}$ holds. The prediction horizon n_p and control horizon n_c of the complex CA are chosen relatively small. Therefore, the CA uses only a few samples of the global MPC optimization.
In Fig. 4.1 the overall hierarchical concept is presented. Note that the input to the CA varying by the different concepts and there constraints.
Two concepts are presented: In the first concept the global MPC is designed to compute a desired cooling capacity while the CA which is realized by a MI-MPC provides u with the constraint that u is in the large sample time always identical to the desired cooling capacity. This constraint leads to a temperature deviation between the ICB temperature and the predicted temperature of the global MPC, see [45]. To avoid this effect, a second concept is presented, where the CA is realized by a mixed-integer optimizer (MIO). The input of the MIO is the predicted ICB temperature of the global MPC. A constraint forces the result of the MIO to obtain exactly the same ICB temperature at the end of the large sample as predicted by the global MPC.

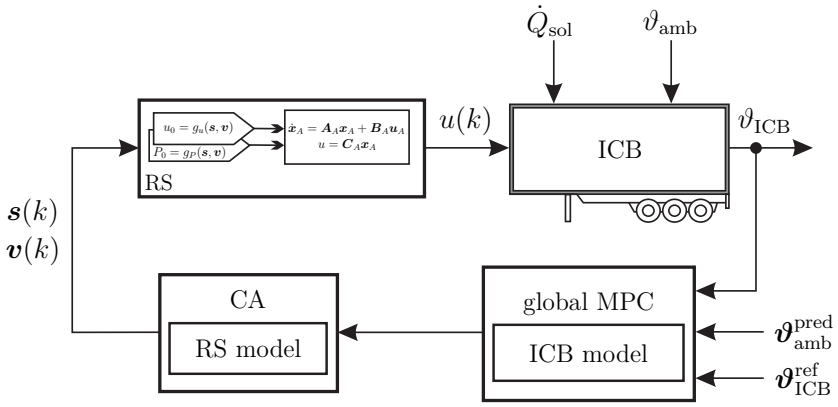

Figure 4.1: Conceptual architecture of the hierarchical control: a global model predictive controller (MPC), the control allocation (CA), the refrigeration system (RS) and the insulated cool box (ICB).

4.3 Concept 1: Cooling capacity constraint

4.3.1 Model assumptions

The RS which is used in the following concept is already shown in Fig. 3.4. All assumptions according to the RS can be seen at the first paragraph in Section 3.5. Furthermore the RS doesn't include a dynamic part, therefore only static maps are used to model the RS, see Section 2.3.5. In this Section the solar irradiation and the α deterioration is not considered.

4.3.2 Control structure

In Fig. 4.2 the conceptual architecture with a MI-MPC as realization for the CA is presented. The purpose of the global MPC is to control the temperature in the ICB and to reject disturbances. In order to guarantee the reference ICB temperature trajectory $\boldsymbol{\vartheta}_{\text{ICB}}^{\text{ref}}$, the global MPC with the underlying dynamic linear ICB model, eq. (2.20), and predicted disturbance trajectory, $\boldsymbol{\vartheta}_{\text{amb}}^{\text{pred}}$, calculates the optimal cooling capacity trajectory $\boldsymbol{U}(K)$.
For the MI-MPC the supply of $\boldsymbol{U}(K)$, while minimizing the cooling costs as well as minimizing the wear are important control goals. Hence, the MI-MPC is used for optimizing these goals by utilizing the redundancy of the RS. The MI-MPC receives $\boldsymbol{U}(K)$ from the upper-level global MPC and optimizes the switched control variables (which correspond to the compressor states $\boldsymbol{s}$ from the RS) and the continuous control variables (which correspond to the valve positions $\boldsymbol{v}$ of the active RCs) to provide $\boldsymbol{U}(K)$. Only the first sample of the optimal control sequences $\boldsymbol{s}$ and $\boldsymbol{v}$ is transferred to the RS and the resultant cooling capacity $u(k)$ is used to achieve the reference temperature in the ICB, see Fig. 4.3. Subsequently, the horizon is shifted one sample and the

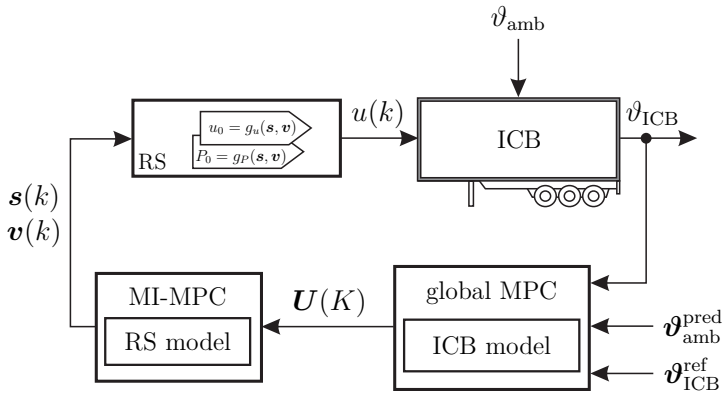

Figure 4.2: Conceptual architecture where the CA is realized by a mixed-integer MPC (MI-MPC).

optimization is restarted.
With the ratio λ a sampling rate conversion in both directions is possible. Note that a suitable anti-aliasing filter must be applied for correct sampling rate conversion.

4.3.3 Global MPC for temperature control

Standard MPC formulations are well-known and given in [10]. To use the dynamic ICB model, eq. (2.20), it is discretized with the zero order hold method and formulated as a linear state-space model. This model can be augmented to provide offset-free control, [94]

$$\boldsymbol{x}_{\text{MPC}}(K+1) = \boldsymbol{A}_a \boldsymbol{x}_{\text{MPC}}(K) + \boldsymbol{B}_a \Delta U(K) + \boldsymbol{E}_a \Delta Z(K), \tag{4.1}$$

$$, y(K) = \boldsymbol{C}_a \boldsymbol{x}_{\text{MPC}}(K) \tag{4.2}$$

with K the sampling instance of the global MPC, $\boldsymbol{A}_a, \boldsymbol{B}_a, \boldsymbol{C}_a, \boldsymbol{E}_a$ the augmented system-, input-, output- and disturbance matrices and

$$\Delta U(K) = U(K) - U(K-1), \tag{4.3}$$

$$\Delta Z(K) = \vartheta_{\text{amb}}^{\text{pred}}(K) - \vartheta_{\text{amb}}^{\text{pred}}(K-1), \tag{4.4}$$

$$\boldsymbol{x}_{\text{MPC}}(K) = \left[\Delta \boldsymbol{x}_{\text{MPC}}^T(K), \quad y(K)\right]^T, \tag{4.5}$$

where $\Delta \boldsymbol{x}_{\text{MPC}} = x_P(K) - x_P(K-1)$, see eq. (2.23).
Based on the state-space model the future state variables are calculated sequentially using the set of future control changes $\Delta \boldsymbol{U}$,

$$\Delta \boldsymbol{U}(K) = \left[\Delta U(K), \quad \Delta U(K+1), \quad \ldots, \quad \Delta U(K+N_{\text{c}}-1)\right]^T. \tag{4.6}$$

The dimension of $\Delta \boldsymbol{U}(K)$ is (N_p x 1). If $N_c < N_p$ the remaining $N_p - N_c$ values of $\Delta \boldsymbol{U}(K)$ are filled with the value of $\Delta U(K + N_{\text{c}} - 1)$.

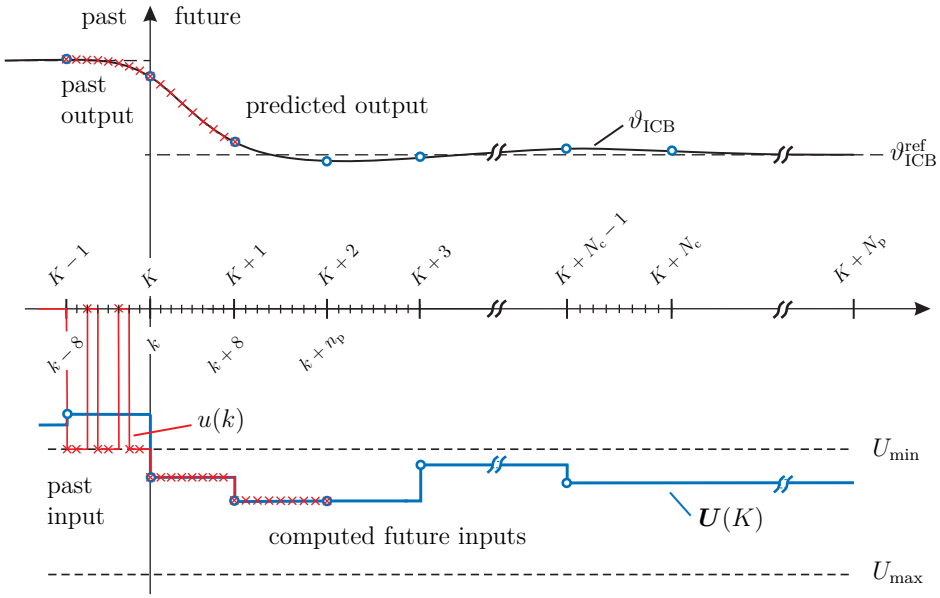

Figure 4.3: Principle of model predictive control, with two different sampling rates. The trajectory $\boldsymbol{U}(K)$ (blue) is defined at the sampling time T_S. The MI-MPC generates $u(k)$ (red) with the sampling time t_S.

The prediction is given by

$$\hat{\boldsymbol{Y}}(K) = \boldsymbol{F}_x \boldsymbol{x}_{\mathrm{MPC}}(K) + \boldsymbol{F}_u \Delta \boldsymbol{U}(K) + \boldsymbol{F}_z \Delta \boldsymbol{Z}(K), \tag{4.7}$$

where

$$\hat{\boldsymbol{Y}}(K) = \left[\hat{y}(K+1|K), \quad \hat{y}(K+2|K), \quad \ldots, \quad \hat{y}(K+N_{\mathrm{p}}|K)\right]^T, \tag{4.8}$$

$$\Delta \boldsymbol{Z}(K) = \left[\Delta Z(K|K), \quad \Delta Z(K+1|K), \quad \ldots, \quad \Delta Z(K+N_{\mathrm{p}}-1|K)\right]^T, \tag{4.9}$$

and the matrices $\boldsymbol{F}_x, \boldsymbol{F}_u$ and $\boldsymbol{F}_z$ are computed by

$$\boldsymbol{F}_x = \left[\boldsymbol{C}_a \boldsymbol{A}_a, \quad \boldsymbol{C}_a \boldsymbol{A}_a^2, \quad \boldsymbol{C}_a \boldsymbol{A}_a^3, \quad \ldots, \quad \boldsymbol{C}_a \boldsymbol{A}_a^{N_p}\right]^T, \tag{4.10}$$

$$\boldsymbol{F}_u = \begin{bmatrix} \boldsymbol{C}_a \boldsymbol{B}_a & 0 & 0 & \ldots & 0 \\ \boldsymbol{C}_a \boldsymbol{A}_a \boldsymbol{B}_a & \boldsymbol{C}_a \boldsymbol{B}_a & 0 & \ldots & 0 \\ \boldsymbol{C}_a \boldsymbol{A}_a^2 \boldsymbol{B}_a & \boldsymbol{C}_a \boldsymbol{A}_a \boldsymbol{B}_a & \boldsymbol{C}_a \boldsymbol{B}_a & \ldots & 0 \\ \vdots & & & & \\ \boldsymbol{C}_a \boldsymbol{A}_a^{N_p-1} \boldsymbol{B}_a & \boldsymbol{C}_a \boldsymbol{A}_a^{N_p-2} \boldsymbol{B}_a & \boldsymbol{C}_a \boldsymbol{A}_a^{N_p-3} \boldsymbol{B}_a & \ldots & \boldsymbol{C}_a \boldsymbol{A}_a^{N_p-N_c} \boldsymbol{B}_a \end{bmatrix}, \tag{4.11}$$

and

$$\boldsymbol{F}_z = \begin{bmatrix} \boldsymbol{C}_a\boldsymbol{E}_a & 0 & 0 & \dots & 0 \\ \boldsymbol{C}_a\boldsymbol{A}_a\boldsymbol{E}_a & \boldsymbol{C}_a\boldsymbol{E}_a & 0 & \dots & 0 \\ \boldsymbol{C}_a\boldsymbol{A}_a^2\boldsymbol{E}_a & \boldsymbol{C}_a\boldsymbol{A}_a\boldsymbol{E}_a & \boldsymbol{C}_a\boldsymbol{E}_a & \dots & 0 \\ \vdots & & & & \\ \boldsymbol{C}_a\boldsymbol{A}_a^{N_p-1}\boldsymbol{E}_a & \boldsymbol{C}_a\boldsymbol{A}_a^{N_p-2}\boldsymbol{E}_a & \boldsymbol{C}_a\boldsymbol{A}_a^{N_p-3}\boldsymbol{E}_a & \dots & \boldsymbol{C}_a\boldsymbol{E}_a \end{bmatrix}. \tag{4.12}$$

The reference trajectory $\boldsymbol{Y}^{\mathrm{ref}}$ is defined as

$$\boldsymbol{Y}^{\mathrm{ref}}(K) = \begin{bmatrix} \boldsymbol{\vartheta}_{\mathrm{ICB}}^{\mathrm{ref}}(K+1) & \boldsymbol{\vartheta}_{\mathrm{ICB}}^{\mathrm{ref}}(K+2) & \dots & \boldsymbol{\vartheta}_{\mathrm{ICB}}^{\mathrm{ref}}(K+N_{\mathrm{P}}) \end{bmatrix}^T. \tag{4.13}$$

The optimization criterion is chosen as

$$J_1 = (\boldsymbol{Y}^{\mathrm{ref}} - \hat{\boldsymbol{Y}})^T \boldsymbol{R}_1 (\boldsymbol{Y}^{\mathrm{ref}} - \hat{\boldsymbol{Y}}) + \Delta\boldsymbol{U}^T \boldsymbol{R}_2 \Delta\boldsymbol{U} \tag{4.14}$$

s.t.

$$-\boldsymbol{U}_{\min} \leq -\boldsymbol{U}(K) \leq -\boldsymbol{U}_{\max}, \tag{4.15}$$

where $\boldsymbol{R}_1$ and $\boldsymbol{R}_2$ are positive semi-definite weighting matrices, which are used for tuning.
The time-variant constraints $\boldsymbol{U}_{\min}$ and $\boldsymbol{U}_{\max}$, eq. (4.15), depend on the system constraints of the RCs, ϑ_{amb} and ϑ_{ICB} and limit the control sequence to the feasible range of the MI-MPC.
The corresponding optimization problem is formally stated as

$$J_1^\star = \min_{\Delta\boldsymbol{U}} J_1. \tag{4.16}$$

The optimal control sequence over the whole horizon N_{p} is given by

$$\Delta\boldsymbol{U}(K) = \arg\min_{\Delta\boldsymbol{U}} J_1^\star, \tag{4.17}$$

and $\boldsymbol{U}(K)$ can be calculated by

$$\boldsymbol{U}(K) = \left[U_1(K-1) + \Delta\boldsymbol{U}(K) \right], \tag{4.18}$$

where $U_1(K-1)$ is the first entry of $\boldsymbol{U}(K-1)$.

4.3.4 MI-MPC for cooling capacity control

The RS model of the MI-MPC has no dynamic state, the problem is formulated as a mixed-integer optimal control problem, with both switched control variables and continuous control variables. Latency periods for the compressor switching can also be considered, note that then a unit commitment problem has to be solved, [25].

The switched decision variables are the active RCs and compressors $\boldsymbol{s}$, the continuous decision variables are the valve positions $\boldsymbol{v}$. The fact that two RCs, each running one active compressor, provide different values of u and P compared to two active compressors in one RC is considered in the optimization.
Only the first three samples, denoted by $U_1(K), U_2(K)$ and $U_3(K)$ of $\boldsymbol{U}(K)$ are used to compute the up-sampled reference values of $\boldsymbol{U}(k)$,

$$\boldsymbol{U}(k) = \Big[U_1(K) \cdot \boldsymbol{I}, \;\; U_2(K) \cdot \boldsymbol{I}, \;\; U_3(K) \cdot \boldsymbol{I}\Big], \tag{4.19}$$

where $\boldsymbol{I} \in \mathbb{R}^{(\frac{np}{2},1)}$, which are used by the MI-MPC to calculates the optimal decision variables. The third part of $\boldsymbol{U}(k)$ in eq. (4.19) is required to guarantee that all values within the moving horizon are well defined. During the large sampling interval T_S of the global MPC the MI-MPC is executed λ times. The first sample of the resulting optimal cooling capacity trajectory $\boldsymbol{u}(k)$ is the actual cooling capacity input to the ICB.
To ensure that the RCs operate in a feasible range, the optimization problem of the MI-MPC includes constraints. The admissible valve position is defined by the time-variant trajectories $\boldsymbol{v}_{\min}(k)$ and $\boldsymbol{v}_{\max}(k)$. The time-variant valve position limits depend on the system constraints of the RCs. Constraints are defined for the superheat temperature, the suction pressure, the discharge pressure and the discharge temperature. These constraints limit the valve position depending on the number of active compressors (one or both active), ϑ_{amb} and ϑ_{ICB}.
The optimization problem of the MI-MPC is formulated as follows:

$$J_2 = (U(k) - u(k))^T R_3 (U(k) - u(k)) + P^T R_4 P + R_5 u_{\Delta\Sigma} + R_6 S \tag{4.20}$$

$$\begin{aligned} &\text{s.t.} \\ &G_{AA}(q^{-1})u(k) = U(K) \text{ for } (k \bmod \lambda) == 0 \\ &\boldsymbol{v}_{\min} \leq \boldsymbol{v} \leq \boldsymbol{v}_{\max}, \end{aligned} \tag{4.21}$$

where R_3, R_4, R_5 and R_6 are positive semi-definite weightings, which are used for tuning. The constraint, eq. (4.21), ensures stability of the global MPC, where $G_{AA}(q^{-1})$ is the pulse transfer function of the anti-aliasing low-pass filter. The constraint (4.21) guarantees that the down-sampled signal of $u(k)$ is always identical to $U(K)$.
The first term in eq. (4.20) guarantees that $\boldsymbol{U}(k)$ is tracked as closely as possible, the second term minimizes P, the third term ensures that the average of $u(k)$ within one large sample of the global MPC represents $\boldsymbol{U}(k)$, and the last term penalizes excessive compressor switching S, which is the main reason for compressor wear. If $-u < -u_{min}$ the quadratic term in eq. (4.20) yields the constant value of u_{min} as an optimal solution. This can be avoided by adding the third term $u_{\Delta\Sigma}$ which enforces switching action of the cooling capacity.

The third term of eq. (4.20) is defined as follows:

$$u_{\Delta\Sigma} = \left| \lambda \cdot U_1(k) - u_{\text{past}} - \sum_{i=1}^{a-1} u(i) \right| + \left| \sum_{i=a}^{b-1} U(i) - \sum_{i=a}^{b-1} u(i) \right| + \epsilon_1 \left| \sum_{i=b}^{n_\text{p}} U(i) - \sum_{i=b}^{n_\text{p}} u(i) \right|, \tag{4.22}$$

where $U_1(k)$ is the first value of $\boldsymbol{U}(k)$, a and b define the position of step changes in $\boldsymbol{U}(k)$, see Fig. 4.4, ϵ_1 indicates the existence of three constant sections for $\boldsymbol{U}(k)$ and u_{past} is the sum of all already implemented values of $u(k)$ in the sequence,

$$\epsilon_1 = \begin{cases} 1 & \text{if } (k \bmod \lambda) \neq 0 \\ 0 & \text{else,} \end{cases} \tag{4.23}$$

and

$$u_{\text{past}} = \begin{cases} \sum\limits_{i=\frac{n_\text{p}}{2}-a}^{k-1} u(i) & \text{if } (k \bmod \lambda) \neq 0 \\ 0 & \text{else.} \end{cases} \tag{4.24}$$

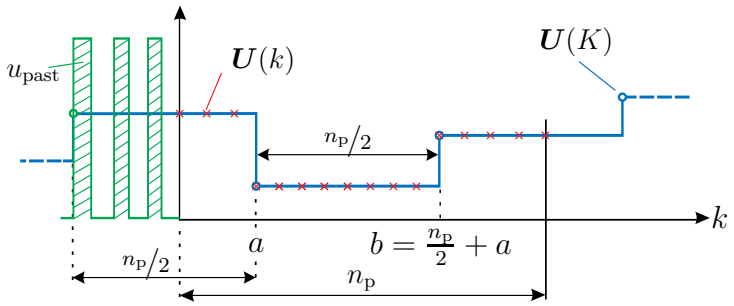

Figure 4.4: Moving horizon of the MI-MPC, $\boldsymbol{U}(K)$ is shifted λ times during one sample K. Every K-th sample only the first two samples of $\boldsymbol{U}(K)$ appear in the horizon n_p, therefore ϵ_1, eq. (4.23), and u_{past}, eq. 4.24, are zero.

The corresponding optimization problem is formally stated as

$$J_2^\star = \min_{\boldsymbol{s},\boldsymbol{v}} J_2. \tag{4.25}$$

4.3.5 Stability

To study closed-loop stability, the following additional assumptions are made:

Assumption 1 *All disturbances stay constant during all iterations at time step k.*

Assumption 2 *The closed-loop control system of the unconstrained global linear MPC without the MI-MPC is globally asymptotically stable.*

Assumption 3 *The error between the switched control $u(k)$ of the MI-MPC and the control $U(k)$ of the global MPC is uncorrelated with $U(k)$.*

Assumption 2 is guaranteed to hold for well-known conditions, [51]. Assumption 3 is reasonable due to the constraint (4.22), which guarantees zero mean error between sampling instances, and the fact that the MI-MPC constructs the switched control $u(k)$ solely based on available compressor combinations and the constant inter-sample value of $U(K)$.
As a direct consequence of Assumption 2 the following Theorem holds:

Theorem 1 *Identical control input*
If the cooling capacity supplied by the MI-MPC is exactly equal to the reference cooling capacity of the global MPC the closed-loop is asymptotically stable.

Proof 1 *In this case the closed-loop transfer function of the inner loop with the MI-MPC is the identity. Therefore, stability is only affected by the global MPC. Due to Assumption 2 the overall control system is asymptotically stable.*

Obviously, Theorem 1 does not apply during switching operation, when a specific cooling capacity cannot be supplied by continuous operation. In that case the following Theorem holds:

Theorem 2 *Switched control input*
If the set of equality constraints

$$u(k) = U(K), \forall \frac{k}{\lambda} = K, k \in \left[\frac{t}{t_S}, \frac{t}{t_S} + n_c - 1 \right]$$

is fulfilled by the MI-MPC's solution $u(k)$, the closed-loop control system will be robustly stable in the sense of being asymptotically ultimately bounded, [48].

Proof 2 *The down-sampled version of the MI-MPCs optimal control input is based on the low-pass filtered continuous signal $\tilde{u}(t)$. This signal is given by*

$$\tilde{u}(t) = g_{\mathrm{AA}}(t) * u(t), \tag{4.26}$$

where $g_{\mathrm{AA}}(t)$ is the weighting function of the (continuous) anti-aliasing low-pass filter and $*$ denotes the convolution operator, $u(t)$ is the continuous version (zero-order hold) of the switched control input $u(k)$. By sampling $\tilde{u}(t)$ at $t = KT_S$, the correctly down-sampled control $\tilde{u}(K)$ results, [63]. Due to Theorem 2 $\tilde{u}(K) = U(K)$ holds, and the predicted control $U(K)$ of the global linear MPC does not change when the horizon is shifted. Hence, the prediction $U(K)$ is invariant to the specific $u(k)$.

However, there will arise an error $e_{\vartheta_{\mathrm{ICB}}}$ in the prediction of the plant's output ϑ_{ICB}: The actual control input is not that of an ideal zero-order hold ($U(t) = U(K) = const.$ for $KT_S \leq t < (K+1)T_S$), but instead it is that of the MI-MPC's switched control input $u(k)$. The resulting prediction error $e_{\vartheta_{\mathrm{ICB}}}$ is given by

$$e_{\vartheta_{\mathrm{ICB}}}(k) = G_{\mathrm{ICB}}(q^{-1})(u(k) - U(k)), \tag{4.27}$$

where $G_{\mathrm{ICB}}(q^{-1})$ is the plant's pulse transfer function for t_S and $U(k)$ is the correctly up-sampled control of the global MPC. Using eq.(4.27) the actual plant output can be written as

$$\begin{aligned} \vartheta_{\mathrm{ICB}}(k) &= G_{\mathrm{ICB}}(q^{-1})u(k) \\ &= G_{\mathrm{ICB}}(q^{-1})U(k) + e_{\vartheta_{\mathrm{ICB}}}(k). \end{aligned}$$

Because of Assumption 3 $e_{\vartheta_{\mathrm{ICB}}}(k)$ will be uncorrelated with $U(K)$, due to the constraint (4.22) it will also be of zero mean. Furthermore, the error $e_{\vartheta_{\mathrm{ICB}}}$ will be bounded since available control inputs $u(k)$ are limited. As the error is bounded, the ICB's temperature will be confined to some neighborhood of the set-point. Hence, the system will be asymptotically ultimately bounded.

4.3.6 Simulation results

Results of a closed-loop simulation are used to demonstrate the control method. The mixed-integer optimization problem is solved with the Gurobi Optimizer. All simulation results have been published in [45].
The sampling time is chosen as $T_S = 8\ min$ in the global MPC and as $t_S = 1\ min$ in the MI-MPC and ICB. The prediction and control horizon of the global MPC are chosen as $N_{\mathrm{p}} = 30$ and $N_{\mathrm{c}} = 10$. The prediction and control horizon of the MI-MPC are set to $n_{\mathrm{p}} = n_{\mathrm{c}} = 16$.

Comparison with conventional control

The proposed controller is compared to a perfect MPC solution, denoted with a *, where only the global MPC (without the MI-MPC) is simulated, and an industry standard PI-controller method with a switching look-up table.
In Fig. 4.5 the solution is plotted over 6.67 h. After 2.5 h the reference ICB temperature $\boldsymbol{\vartheta}_{\mathrm{ICB}}^{\mathrm{ref}}$ changes. After 5 h a step in the ambient temperature $\boldsymbol{\vartheta}_{\mathrm{amb}}^{\mathrm{pred}}$ occurs. For a fair comparison between the proposed method and the PI-controller, the $\boldsymbol{\vartheta}_{\mathrm{ICB}}^{\mathrm{ref}}$ and $\boldsymbol{\vartheta}_{\mathrm{amb}}^{\mathrm{pred}}$ steps are not included in the predictions of the global MPC. However, it can be seen that the performance of the MI-MPC is significantly better than that of the traditional PI-controller.
The first plot shows the cooling capacities and the constraints of $\boldsymbol{U}_{\min}$ and $\boldsymbol{U}_{\max}$, which are plotted in gray. Switching is necessary if $U(k) < U_{\min}(k)$. It can also be seen that the MI-MPC only minimally affects the performance of the global MPC.

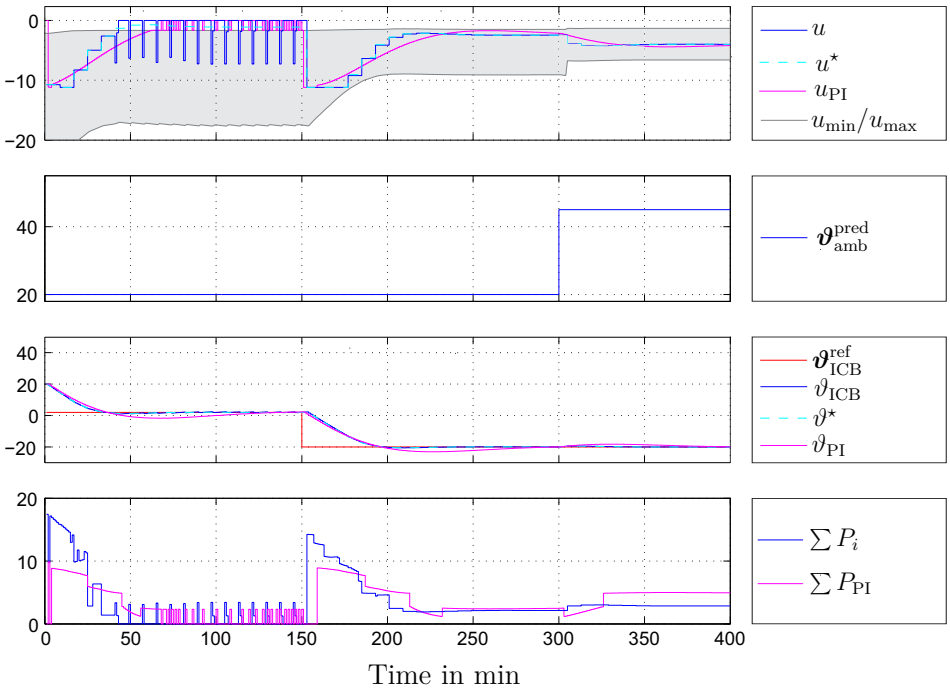

Figure 4.5: Comparison conventional control method with optimized method.

The last plot shows the total electrical power consumed by the MI-MPC compared with the PI controller. In this specific simulation the MI-MPC needs 17 % less power than the standard PI controller. Note that the deviation of the electrical power occurs because the MI-MPC utilizes the redundancy of the RCs and optimizes the active compressor combination according to the optimization problem, eq. (4.20), where minimization of the electrical power is defined. In contrast, the PI controller uses the next compressor combination in a static look-up table, which provides $U(k)$ independent of the electrical power consumption.

Robustness check

To demonstrate the robustness of the control concept a simulation based on an incorrect prediction of the ambient temperature $\boldsymbol{\vartheta}_{\mathrm{amb}}^{\mathrm{pred}}$ is made. A random disturbance d_{n}, with increasing variance is added to $\boldsymbol{\vartheta}_{\mathrm{amb}}^{\mathrm{pred}}$ every K-th sample. In Table 4.1 the RMSE between the reference and actual ICB temperatures are listed.

$$\mathrm{RMSE} = \sqrt{\frac{1}{N}\sum_{k=1}^{N}\left(\boldsymbol{\vartheta}_{\mathrm{ICB}}(k) - \boldsymbol{\vartheta}_{\mathrm{ICB}}^{\mathrm{ref}}(k)\right)^2},$$

where N is the number of simulation steps.
It can be seen that increasing variances affect the RMSE. Nevertheless, even for large prediction errors the temperature remains in an acceptable region around the reference

σ^2	0	1	2	3	4
RMSE	0.2166	0.2449	0.2472	0.2759	0.2879

Table 4.1: RMSE values for different variances.

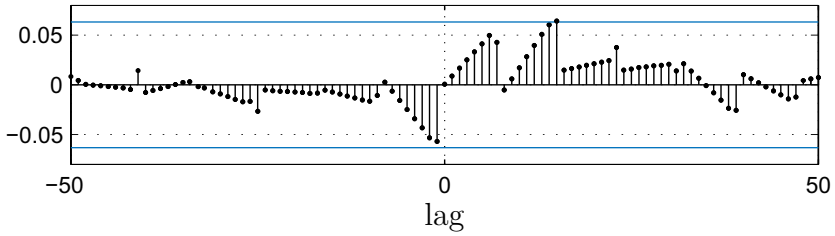

Figure 4.6: Cross-covariance function for $U(k)$ and $U(k) - u(k)$ together with 95 % confidence intervals for zero value. The correlation coefficient between the two signals is 13.10^{-4}.

temperature value. Typically an acceptable value for the region of tolerance is defined by $\boldsymbol{\vartheta}_{\mathrm{ICB}}^{\mathrm{ref}} \pm 0.5°\mathrm{C}$.
For $\sigma^2 = 1$ the cross-covariance function and the 95 % confidence interval for zero are plotted in Fig. 4.6. It can be seen that Assumption 3 is fulfilled in the given application example.
Fig. 4.7 demonstrates the robustness of the control concept. The random disturbance d_{n} is shown in the first plot, colored in green. As reference value the global MPC without the MI-MPC is used (second and third plot, denoted with *, colored in magenta). It can be seen that the MI-MPC (second and third plot, colored in blue) is able to handle the random disturbance and never exceeds the region of tolerance.

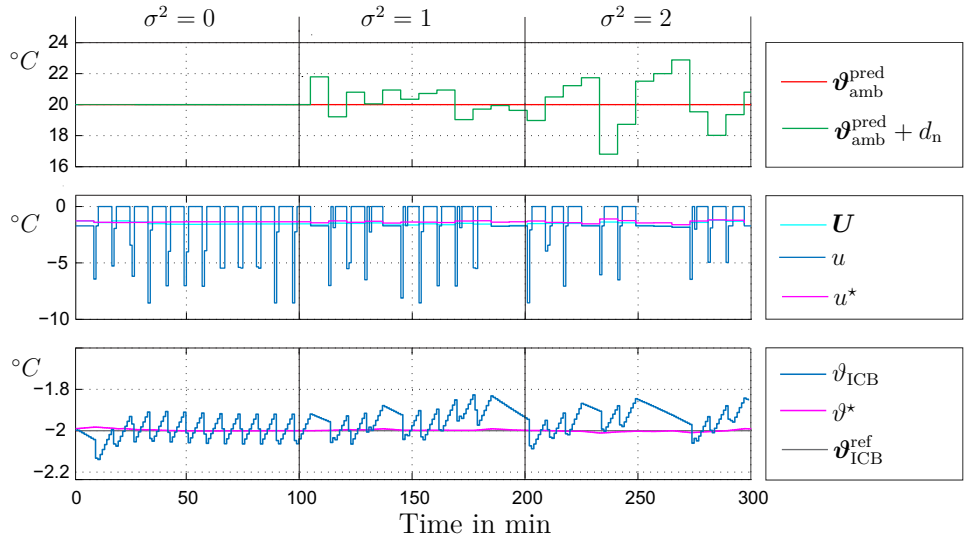

Figure 4.7: Robustness against faulty prediction of the ambient temperature.

4.4 Concept 2: Predicted temperature constraint

4.4.1 Model assumptions

The RS which is used in the following concept is already shown in Fig. 3.4. All assumptions according to the RS can be seen at the first paragraph in Section 3.5. In this Section the RS includes a static and a dynamic part, see Section 2.3.5 and also solar irradiation as an unknown disturbance. However, α deterioration is not considered.

4.4.2 Control structure

In Fig. 4.8 the conceptual architecture with a MIO as realization for the CA is presented.

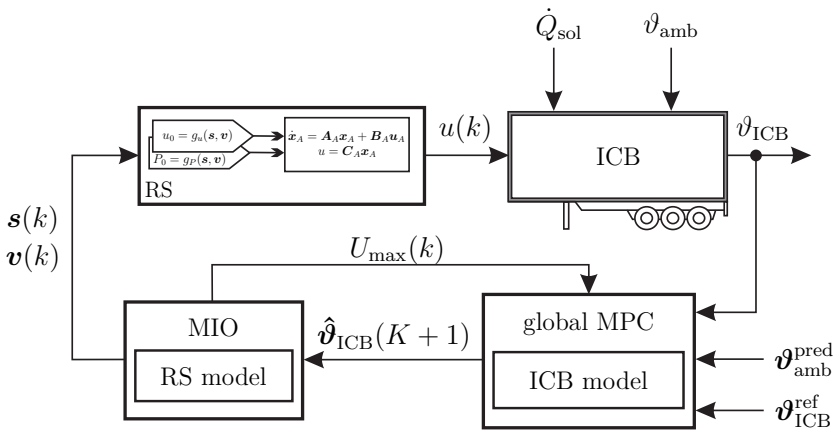

Figure 4.8: Conceptual architecture where the CA is realized by a mixed-integer optimizer (MIO) and the RS is modeled by a Hammerstein system.

The global MPC with the underlying dynamic linear ICB model, eq. (2.20), calculates the optimal cooling capacity trajectory $\boldsymbol{U}(K)$ and predicts the temperature of the ICB $\hat{\boldsymbol{\vartheta}}_{\mathrm{ICB}}$ under consideration of the known disturbance trajectory $\boldsymbol{\vartheta}^{\mathrm{pred}}_{\mathrm{amb}}$ and the ICB temperature reference trajectory $\boldsymbol{\vartheta}^{\mathrm{ref}}_{\mathrm{ICB}}$. Unknown disturbances on the ICB like $\dot{Q}_{\mathrm{sol}}$ are compensated by the integral behavior of the global MPC. The predicted temperature of the ICB is then used to formulate an output constraint for the MIO.
The MIO defines the switched control variables $\boldsymbol{s}$ and the continuous control variables (valve positions $\boldsymbol{v}$). Future constraints $\boldsymbol{U}_{\max}(K)$ are computed and sent back to the global MPC. This optimization is constrained such that at the end of the large sampling interval $\vartheta_{\mathrm{ICB}} = \hat{\vartheta}_{\mathrm{ICB}}$ holds, see Fig. 4.9.
As the MIO gets new information only every λ-th fast sample, the MIO is also only performed at the large sampling instance K. For the following $\lambda - 1$ small samples the computed solution for $\boldsymbol{s}$ and $\boldsymbol{v}$ is preserved and sent to the RS.

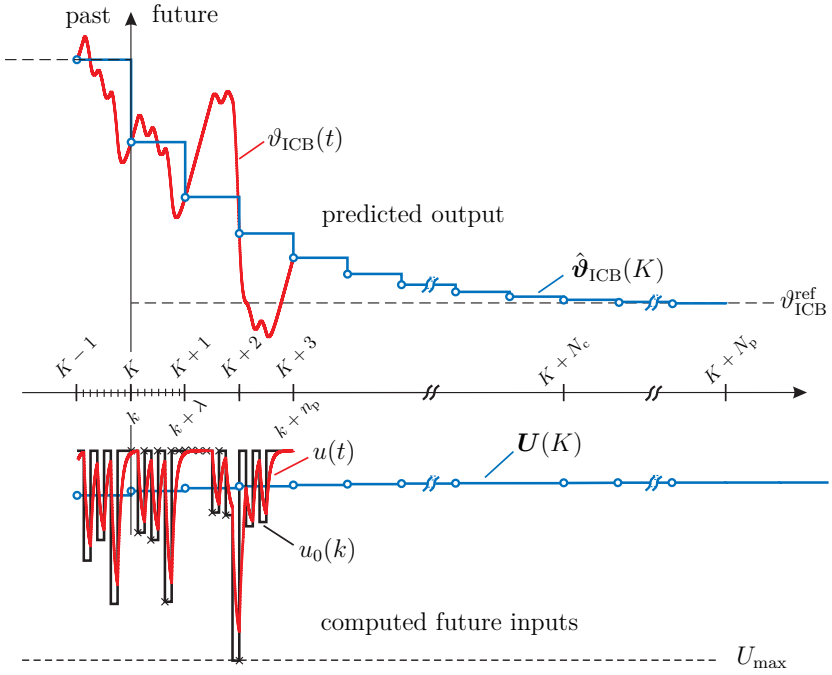

Figure 4.9: Principle of model predictive control, with two different sampling rates. The trajectory $\boldsymbol{U}(K)$ (blue) is defined at the sampling time T_s. The MIO generates $u_0(k)$ (black) with the sampling time t_s. The continuous temperature signal $\vartheta_{\mathrm{ICB}}(t)$ (red) is correctly sampled to $\hat{\boldsymbol{\vartheta}}_{\mathrm{ICB}}(K)$ (blue).

4.4.3 Global MPC for temperature control

The offset-free MPC formulation is already mentioned in Section 4.3.3 , eqns. (4.1-4.13). The optimization criterion is chosen as

$$\begin{aligned} J_1 \;=\; & (\boldsymbol{Y}^{\mathrm{ref}} - \hat{\boldsymbol{Y}})^T \boldsymbol{R}_1 (\boldsymbol{Y}^{\mathrm{ref}} - \hat{\boldsymbol{Y}}) + \Delta \boldsymbol{U}^T \boldsymbol{R}_2 \Delta \boldsymbol{U} + V(\boldsymbol{x}_{\mathrm{MPC}}(K+N_c)) \quad (4.28) \\ & \text{s.t.} \\ & \text{eq. (4.1) and (4.2)} \\ & \mathbf{0} \le -\boldsymbol{U}(K) \le -\boldsymbol{U}_{\max}(K), \end{aligned}$$

where $\boldsymbol{R}_1$ and $\boldsymbol{R}_2$ are positive semi-definite weighting matrices, which are used for tuning and the terminal cost $V(\boldsymbol{x}_{\mathrm{MPC}}(K+N_c))$:

$$V(\boldsymbol{x}_{\mathrm{MPC}}(K+N_c)) = \frac{1}{2}(\boldsymbol{x}_{\mathrm{MPC}}^{\mathrm{ref}} - \boldsymbol{x}_{\mathrm{MPC}}(K+N_c))^T \boldsymbol{P}_L (\boldsymbol{x}_{\mathrm{MPC}}^{\mathrm{ref}} - \boldsymbol{x}_{\mathrm{MPC}}(K+N_c)), \quad (4.29)$$

where the steady state is defined by $\boldsymbol{x}_{\mathrm{MPC}}^{\mathrm{ref}}$. The terminal cost corresponding to the solution of an infinite horizon LQ-controller is weighted by the solution of the corresponding

discrete-time Riccati equation

$$\boldsymbol{P}_L = -(\boldsymbol{A}_a^T \boldsymbol{P}_L \boldsymbol{B}_a)(\boldsymbol{B}_a^T \boldsymbol{P}_L \boldsymbol{B}_a + \boldsymbol{R}_2)^{-1}(\boldsymbol{B}_a^T \boldsymbol{P}_L \boldsymbol{A}_a) + \boldsymbol{A}_a^T \boldsymbol{P}_L \boldsymbol{A}_a + \boldsymbol{R}_1, \tag{4.30}$$

which corresponds to a dual-mode MPC concept [75].
The time-varying constraint $\boldsymbol{U}_{\max}(\mathrm{K})$ depends on the system constraints of the RCs, ϑ_{amb} and ϑ_{ICB} and limits the control sequence to the feasible range of the MIO.
The corresponding optimization problem is formally stated as

$$J_1^\star = \min_{\Delta \boldsymbol{U}} J_1 \tag{4.31}$$

s.t.

constraints of eq. (4.28),

and the optimal control sequence over the whole control horizon N_{c} is given by

$$\Delta \boldsymbol{U} = \arg\min_{\Delta \boldsymbol{U}} J_1. \tag{4.32}$$

4.4.4 State Transition

The state transition of a system, eq. (2.23), with state equation

$$\dot{x}_P = A_P x_P + B_P u \tag{4.33}$$

from initial state $x_P(t = t_0)$ to final state $x_P(t = t_1)$ is given by

$$x_P(t_1) = e^{A_P(t_1 - t_0)} x_P(t_0) + \int_{\tau = t_0}^{t_1} e^{A_P(t_1 - \tau)} B_P u(\tau) d\tau. \tag{4.34}$$

For $KT_s \leq t < (K+1)T_s$ with fixed sampling time T_s and $u(t) = U(K) = const$ eq. (4.34) is transformed to

$$\begin{aligned} x_P(K+1) &= e^{A_P T_s} x_P(K) + U(K) \int_{KT_s}^{(K+1)T_s} e^{A_P((K+1)T_s - \tau)} B_P d\tau \\ &= \Phi_P x_P(K) + \Gamma_P U(K). \end{aligned} \tag{4.35}$$

In eq. (4.35) the terms $\Phi_P x_P(K)$ and $\Gamma_P U(K)$ denote the free and the forced response of the system, eq. (4.33), for the constant input $U(K)$, respectively. Note that Φ_P and Γ_P are constant matrices depending only on A_P, B_P and T_s. Furthermore, the effect of constant disturbances $\boldsymbol{z}(K)$ over one large sample K would be given by an additional additive term $\boldsymbol{M}_P \boldsymbol{z}(K)$, where $\boldsymbol{M}_P$ is computed as Γ_P in eq. (4.35) with B_P replaced by $\boldsymbol{E}_P$.

For the smaller sampling time t_s and the state-space system, eq. (2.25), the transition over one small sample t_s is given by

$$\boldsymbol{x}(k+1) = e^{\boldsymbol{A}t_s}\boldsymbol{x}(k) + u_0(k) \int_{kt_s}^{(k+1)t_s} e^{\boldsymbol{A}((k+1)t_s-\tau)}\boldsymbol{B}d\tau = \boldsymbol{\Phi}\boldsymbol{x}(k) + \boldsymbol{\Gamma}u_0(k). \tag{4.36}$$

Again, the effect of constant disturbances $\boldsymbol{z}(k)$ over one small sample k would be given by an additional additive term $\boldsymbol{M}\boldsymbol{z}(k)$, where $\boldsymbol{M}$ is computed as $\boldsymbol{\Gamma}$ in eq. (4.36) by replacing $\boldsymbol{B}$ with $\boldsymbol{E}$.

4.4.5 Constraint formulation

The basic idea for the constraint formulation is the requirement that at the end of the large sample time the prediction of ϑ_{ICB} by the global MPC $x(K+1)$ based on the input $u(K)$ must be identical to the result of λ control inputs $u_{0,j}, j = 1...\lambda$, by the MIO based on the inputs $u_0(k)$:

$$C_P x_P(K+1) = \boldsymbol{C}\boldsymbol{x}(k+\lambda). \tag{4.37}$$

Let $\boldsymbol{C}\boldsymbol{x}(k) = C_P x_P(K)$ then $x_P(K+1)$ according to eq. (4.35) with the additional disturbance $\boldsymbol{z}(K)$ is given by

$$x_P(K+1) = \Phi_P x_P(K) + \Gamma_P U(K) + \boldsymbol{M}_P\boldsymbol{z}(K), \tag{4.38}$$

and $\boldsymbol{x}(k+\lambda)$ is computed by recursive evaluation of eq. (4.36) using the combined linear dynamics of RS and plant given in eq. (2.25):

$$\begin{aligned}\boldsymbol{x}(k+\lambda) = {} & e^{\lambda\boldsymbol{A}t_s}B\boldsymbol{x}(k) + u_0(k)e^{\boldsymbol{A}(\lambda-1)t_s}\int_{kt_s}^{(k+1)t_s} e^{\boldsymbol{A}((k+1)t_s-\tau)}\boldsymbol{B}d\tau \\ & + u_0(k+1)e^{\boldsymbol{A}(\lambda-2)t_s}\int_{(k+1)t_s}^{(k+2)t_s} e^{\boldsymbol{A}((k+2)t_s-\tau)}\boldsymbol{B}d\tau + \cdots + \\ & + u_0(k+\lambda-1)\int_{(k+\lambda-1)t_s}^{(k+\lambda)t_s} e^{\boldsymbol{A}((k+\lambda)t_s-\tau)}\boldsymbol{B}d\tau + \boldsymbol{\eta}(\boldsymbol{A},\boldsymbol{E},\boldsymbol{z}(K)).\end{aligned} \tag{4.39}$$

The term $\boldsymbol{\eta}(\boldsymbol{A},\boldsymbol{E},\boldsymbol{z}(K))$ in eq. (4.39) denotes the effect of the disturbances for which $\boldsymbol{z}(k+j) = \boldsymbol{z}(K)$ holds ($\boldsymbol{z}$ is constant over one large sample). Setting $e^{\lambda\boldsymbol{A}t_s} = (e^{\boldsymbol{A}t_s})^\lambda = \boldsymbol{\Phi}^\lambda$ eq. (4.39) can be written as

$$\begin{aligned}\boldsymbol{x}(k+\lambda) &= \boldsymbol{\Phi}^\lambda\boldsymbol{x}(k) + \boldsymbol{\Gamma}_1u_0(k) + \boldsymbol{\Gamma}_2u_0(k+1) + \ldots + \boldsymbol{\Gamma}_\lambda u_0(k+\lambda-1) \\ &+ \underbrace{\boldsymbol{M}_1\boldsymbol{z}(K) + \boldsymbol{M}_2\boldsymbol{z}(K) + \ldots + \boldsymbol{M}_\lambda\boldsymbol{z}(K)}_{\boldsymbol{M}_\Sigma\boldsymbol{z}(K)},\end{aligned} \tag{4.40}$$

where $\mathbf{\Gamma}_i$, $\boldsymbol{M}_i$, and $\boldsymbol{M}_\Sigma$ are constant coefficients for the given plant. Therefore,

$$\begin{aligned} C_P x_P(K+1) &= \boldsymbol{C}\boldsymbol{x}(k+\lambda) \qquad \Leftrightarrow \\ C_P\left(\Phi_P x_P(K) + \Gamma_P U(K)\right) + [C_P \boldsymbol{M}_P - \boldsymbol{C}\boldsymbol{H}_\Sigma]\boldsymbol{z}(K) \\ = \boldsymbol{C}\boldsymbol{\Phi}^\lambda \boldsymbol{x}(k) + \boldsymbol{C}\left(\mathbf{\Gamma}_1 u_0(k) + \ldots + \mathbf{\Gamma}_\lambda u_0(k+\lambda-1)\right). \end{aligned} \tag{4.41}$$

Inserting eq. (2.17) in eq. (4.41) and observing that $[C_P \boldsymbol{M}_P - \boldsymbol{C}\boldsymbol{H}_\Sigma] \equiv \mathbf{0}$ yields the final form of the nonlinear equality constraint

$$\begin{aligned} C_P\left(\Phi_P x_P(K) + \Gamma_P U(K)\right) = \boldsymbol{C}\boldsymbol{\Phi}^\lambda \boldsymbol{x}(k) + \boldsymbol{C}(\mathbf{\Gamma}_1 g_u(\boldsymbol{s}(k), \boldsymbol{v}(k)) \\ + \ldots + \mathbf{\Gamma}_\lambda g_u(\boldsymbol{s}(k+\lambda-1), \boldsymbol{v}(k+\lambda-1))). \end{aligned} \tag{4.42}$$

4.4.6 MIO for cooling capacity control

Because of the redundancy of the RCs the MIO targets different goals. minimizing the wear which results from excessive compressor switching S, or the electrical power consumption P can be considered in the optimization.
The optimization problem of the MIO is formulated as follows:

$$\begin{aligned} J_2 \;=\; & (U(k)-u(k))^T R_3 (U(k)-u(k)) + P^T R_4 P + R_6 S \\ & \text{s.t.} \\ & \boldsymbol{s} \in \{0,1\} \\ & \boldsymbol{v}_{\min} \le \boldsymbol{v} \le \boldsymbol{v}_{\max} \\ & \text{Eq. (2.19)} \\ & \text{Eq. (4.42)}, \end{aligned} \tag{4.43}$$

where R_3, R_4 and R_6 are positive semi-definite weightings used for tuning.
The first term in eq. (4.43) guarantees that $U(k)$, which is the finely sampled $U(K)$, is tracked. The time-variant inequality constraints ensure that the RCs always operate in a feasible range.
The corresponding optimization problem is formally stated as

$$\begin{aligned} & J_2^\star = \min_{\boldsymbol{s},\boldsymbol{v}} J_2 \\ & \text{s.t.} \\ & \text{constraints of eq. (4.43)}, \end{aligned} \tag{4.44}$$

and the optimal control sequence $\boldsymbol{u}_0$ over the whole horizon n_p is given by

$$\boldsymbol{u}_0(k) = g_u(\arg\min_{\boldsymbol{s},\boldsymbol{v}} J_2). \tag{4.45}$$

The MIO is executed only once at the beginning of each large sample K of the global MPC. Latency periods for compressor switching can also be considered; in this case a unit commitment problem has to be solved, see e.g. [25].

4.4.7 Stability and feasibility

Stability of the closed-loop system is discussed based on the stabilizing behavior of the global MPC. Due to the constraint for the MIO derived in Section 4.4.5 the global MPC shows asymptotic convergence to the set point in the large sampling interval K. The behavior of the continuous-time trajectory $\boldsymbol{x}(t)$ between the large samples is shown to be bounded, and the condition for existence of a limit cycle passing through the set point is given.

Global MPC

The global MPC presented in Section 4.4.3 has been designed as a dual mode MPC (see e.g. [75], pp. 142). For the case of an active input constraint $U(K) = U_{\max} = const.$ the linear and stable plant will show stable behavior: If the setpoint $\vartheta_{\mathrm{ICB}}^{\mathrm{ref}}$ is feasible for some realizable $U(K) = U^{\mathrm{ref}}$, the plant's trajectory will develop along an exponential time series according to eq.(4.46)

$$x_P(K+1) = \Phi x_P(K) + \Gamma U_{\max}, \tag{4.46}$$

and eventually the trajectory will enter a neighborhood of the setpoint with unconstrained closed-loop dynamics. These dynamics are equal to a stable state-feedback controller with feedback gain $-G_{\mathrm{FB}}$ ([75], p.24). Thus, if the setpoint is feasible and constraint (4.42) is always fulfilled, the region of attraction for the global MPC is unbounded.

Intersample Boundedness of x

The results of Section 4.4.7 guarantee that $\boldsymbol{x}(K)$ converges to the setpoint under some conditions. However, it remains to be shown that $\boldsymbol{x}(t)$ is stable between large samples K. The general description of $\boldsymbol{x}(t)$ between large samples K and $K+1$, $KT_s \leq t < (K+1)T_s$, is given by

$$\boldsymbol{x}(t) = \boldsymbol{\Phi}^{\lambda}(t)\boldsymbol{x}(K) + \boldsymbol{\Gamma}_1(t)u_{0,1} + \ldots + \boldsymbol{\Gamma}_{\lambda}(t)u_{0,\lambda} + \boldsymbol{M}_1(t)\boldsymbol{z}(K) + \ldots + \boldsymbol{M}_{\lambda}(t)\boldsymbol{z}(K), \tag{4.47}$$

where $\boldsymbol{\Phi}(t)$, $\boldsymbol{\Gamma}_i(t)$, and $\boldsymbol{M}_i(t)$ can be obtained from eq. (4.39) by replacing the fixed value of t_s by the independent variable of t. As the control inputs $u_{0,j}$ of the MIO are bounded $\boldsymbol{x}(t)$ will also be bounded for all K. A conservative estimate for such a bound is given in A.

Existence and stability of a limit cycle

In steady state (i.e. when $\boldsymbol{x}(K) = \boldsymbol{x}^{\mathrm{ref}}$, $\forall K$) the continuous-time trajectory of the combined dynamics $\boldsymbol{x}(t)$ need not contract to the setpoint. Such an asymptotic behavior

will only occur for $u_{0,j} = U(K)$. Under the assumption that the control sequence $u_0(k)$ of the MIO is the result of a deterministic program, a cyclo-stationary sequence $u_0^*(k+j),\ j = 1, \ldots, \lambda$ results for holding the set point $y_{y_P(K)=y_{\text{set}}},\ \forall K$. As a consequence the continuous-time state trajectory must be a limit cycle described by

$$\boldsymbol{x}^*(t) = \boldsymbol{\Phi}(t)\boldsymbol{x}^{\text{ref}} + \boldsymbol{\Gamma}_1(t)u_{0,1}^* + \boldsymbol{\Gamma}_2(t)u_{0,2}^* + \ldots + \boldsymbol{\Gamma}_\lambda(t)u_{0,\lambda}^*, \tag{4.48}$$

with initial condition $\boldsymbol{x}(t_0) = \boldsymbol{x}^{\text{ref}}$, $t_0 \leq t < \lambda t_s$.
The main obstacle for proving the stability of such a limit cycle with period T_s is the possibly discontinuous objective function of the MIO. It need not be differentiable in the vicinity of $\boldsymbol{x}^{\text{ref}}$, and as a consequence the switching pattern $u_0(k)$ may exhibit large changes between consecutive samples even with constraint eq. (4.42) fulfilled.
However, if the objective function of the MIO is assumed to be differentiable in the vicinity of $\boldsymbol{x}^{\text{ref}}$, a stable limit cycle can be proven by the following reasoning: Let $\mathbb{S}\ \epsilon\ \mathbb{R}^{n-1}$ be a locally differentiable transversal section of $x(t)$ through $\boldsymbol{x}^{\text{ref}}$ in the state-space $\mathbb{R}^n$ and $\mathbb{U}\ \epsilon\ \mathbb{R}^n$ an open connected neighborhood of $\boldsymbol{x}_{\text{set}}$. Then

$$\boldsymbol{x}^{q+1} = \mathcal{P}(\boldsymbol{x}^q) \tag{4.49}$$

defines a Poincaré map $\mathcal{P}$ for the fixed-point $\boldsymbol{x} = \boldsymbol{x}^{\text{ref}}$ (hence $\mathcal{P}(\boldsymbol{x}^{\text{ref}}) = \boldsymbol{x}^{\text{ref}}$). Note that $\boldsymbol{x}^q$ does not denote sampling in the time domain but occurrence of an intersection of $\boldsymbol{x}(t)$ with $\mathbb{S}$.
The computation of $\mathcal{P}$ is not always possible but the local Jacobian $J_\mathcal{P} = \frac{\partial \mathcal{P}}{\partial \boldsymbol{x}}$ in $\boldsymbol{x}_{\text{set}}$ can be evaluated numerically. Choosing $\mathbb{S}$ to be an orthogonal plane $\boldsymbol{o}$ through $\boldsymbol{x}_{\text{set}}$:

$$\mathbb{S}: \quad \boldsymbol{o}(\boldsymbol{x} - \boldsymbol{x}_{\text{set}}) = [o_1\ o_2\ \ldots\ o_{n-1}\ 0](\boldsymbol{x} - \boldsymbol{x}_{\text{set}}) = 0 \tag{4.50}$$

gives such a local linearization of $\mathcal{P}$ with the proper choice of the normal vector n. In this case $\lim\limits_{q\to\infty} \boldsymbol{x}^q = \lim\limits_{K\to\infty} \boldsymbol{x}(K) = \boldsymbol{x}^{\text{ref}}$, and more importantly, spatial and temporal sampling approximately coincide: $\boldsymbol{x}^q \approx \boldsymbol{x}(K)$. Hence, $\boldsymbol{x}^q$ has the same asymptotic stability properties as $\boldsymbol{x}(K)$ and the limit cycle exists and is stable.

4.4.8 Feasibility

Hard equality constraints such as eq. (4.42) in MPC raise the question if the constrained optimization problem is feasible. It is important to note that the equality constraint, eq. (4.42), is a scalar equation, so only one degree of freedom is lost in the optimization of the MIO. This poses minimal restrictions on feasibility as still at least $\lambda - 1$ degrees of freedom remain. Even if in the critical case $t_s = T_s$, $\lambda = 1$, and the value of $u(k)$ is fixed by $u(k) \equiv U(K)$, the MIO typically has some degrees of freedom due to the redundant RS. As long as $u(k) \equiv U(K)$ can be provided by the RS the constrained problem is feasible.
An additional complication is the state dependency of the constraints on $u_0(k)$. The problem of feasibility can therefore be tackled by a constraint communication between global MPC and MIO:

1. The global MPC solves the problem, eq. (4.28), for some fixed but relaxed $\boldsymbol{U}_{\max}$.

2. In the MIO a sequence of $u_{0,\max}(k)$ is computed for each K in the control horizon. This must be done sequentially i.e. $u_{0,\max}(k)$ is given by the initial state $\boldsymbol{x}(k)$ and defines $\boldsymbol{x}_{\max}(k+1)$, $u_{0,\max}(k+1)$ is given by $\boldsymbol{x}_{\max}(k+1)$ etc. Thus, the right hand side of eq. (4.41) is defined and $\Phi_P x_{P,\max}(K)$ is also known. This allows eq. (4.41) to be explicitly solved for $U_{\max,\mathrm{MI}}(K)$.

3. This value is communicated back to the global MPC and a second optimization with $U_{\max}(K) = U_{\max,\mathrm{MI}}(K)$ is done.

However, due to the state dependency of the $u_{0,\max}(k)$ actually an iteration of the sequence described above would be necessary, and convergence of such an iteration is hard to prove. In the application to an RS all simulations have shown that a single evaluation suffices.
For practical application one effective way to handle feasibility is the implementation of the the equality constraint as a soft constraint. Since the global MPC is designed with integral action, no steady-state error is to be expected anyway. Another way would be to precompute the feasible operating envelope of the RS and store a multidimensional look-up table for $\boldsymbol{U}_{\max}$ in the global MPC. This is current state of the art but requires RS-characteristics to be implicitly stored in the global MPC.

4.4.9 Simulation results

Results of closed-loop simulations are presented and discussed to demonstrate the functionality and effectivity of the proposed control scheme. A comparison with conventional PI-control, compensation of an unmeasured disturbance (solar irradiation), robustness with respect to RS-model errors and faulty disturbance predictions are presented. Additionally, a limit cycle in steady state operation is shown and discussed.

Simulation setup

The nonlinear static models g_u and g_P of the RS consists of high-dimensional look-up tables, provided by the manufacturer. The linear dynamic model of the RS is represented by simple and decoupled dynamics for u and P for demonstration purposes. The respective transfer functions are:

$$G_{A,u} = \frac{1}{1+30s}, \qquad G_{A,P} = \frac{1+5s}{1+10s}$$

Parameters for the simulation results are given in Table 4.2. In all figures u and P is shown in kW, all temperatures are shown in degree Celsius and the time is given in sec. The mixed-integer optimization problem is solved with Yalmip [40], and the Gurobi optimizer [19].

Parameter	Value	Parameter	Value
T_s	8 min	N_p	30
t_s	1 min	N_c	10
A_ICB	163.5 m^2	n_p	16
α	0.4 $\mathrm{W/m^2K}$	n_c	16
mc_p	8.8e6 $\mathrm{J/K}$	R_3	1
$\boldsymbol{R}_1$	$\begin{bmatrix} 1 & 0 \\ 0 & 10^7 \end{bmatrix}$	R_4	0.1
$\boldsymbol{R}_2$	10^{-5}	R_5	100

Table 4.2: Parameters for the simulations

Comparison with conventional control

The controller proposed in this Chapter for three RCs with six compressors (MIO6) is compared to an MIO with three large compressors (MIO3) (one in each each RC), a perfect MPC solution (MPC), where only the global MPC without the MIO is simulated, and an industry standard PI-controller method combined with a hysteresis switching scheme (PI). The PI-controller was tuned such that no overshoot occurred in the constrained case ($K_P = 15000$, $K_I = 155$), see Fig. 4.5. The hysteresis controller is activated whenever the PI-control is smaller than $u_\mathrm{min}(k)$. Either $u = 0$ or $u = u_\mathrm{min}(k)$ are activated in this case. The hysteresis is defined by ± 0.0005 as switching values for the control error; although these values achieve approximately the same switching count as the proposed method.
In Fig. 4.10 the solution is plotted over 19200 sec. At 12200 sec a step in ϑ_amb occurs ($15°C$ to $30°C$). For a fair comparison between the proposed method and the PI-controller, the ϑ_amb step is not included in the predictions of the global MPC. The first plot shows the ICB temperature. It can be seen that the MIO does not affect the performance of the global MPC as the blue, black, and green lines coincide.
The second plot shows the cooling capacities u and the feasible range of stationary cooling capacity u_0, which is plotted in gray. The constraint for the method with three large compressors is plotted as black dashed line. Note that the constraint directly affects only u_0, due to the dynamics of the RS u reaches the constraint only asymptotically.
The last plot in Fig. 4.10 shows the total electrical power consumed by the different methods.
In Fig. 4.11 a detailed plot of Fig. 4.10 is shown. After the ambient step the limit cycle vanishes for the MIO6. This is caused by a larger feasible range for u_0 shown in gray in the second plot. The necessary cooling capacity after the step is no longer in the constrained region. However, the minimal u_0 for the MIO3 with three large compressors is always smaller (denoted with the dotted line in gray) and therefore this method switches into another limit cycle.
The root-mean-squared-error (RMSE) between the reference temperature and the ac-

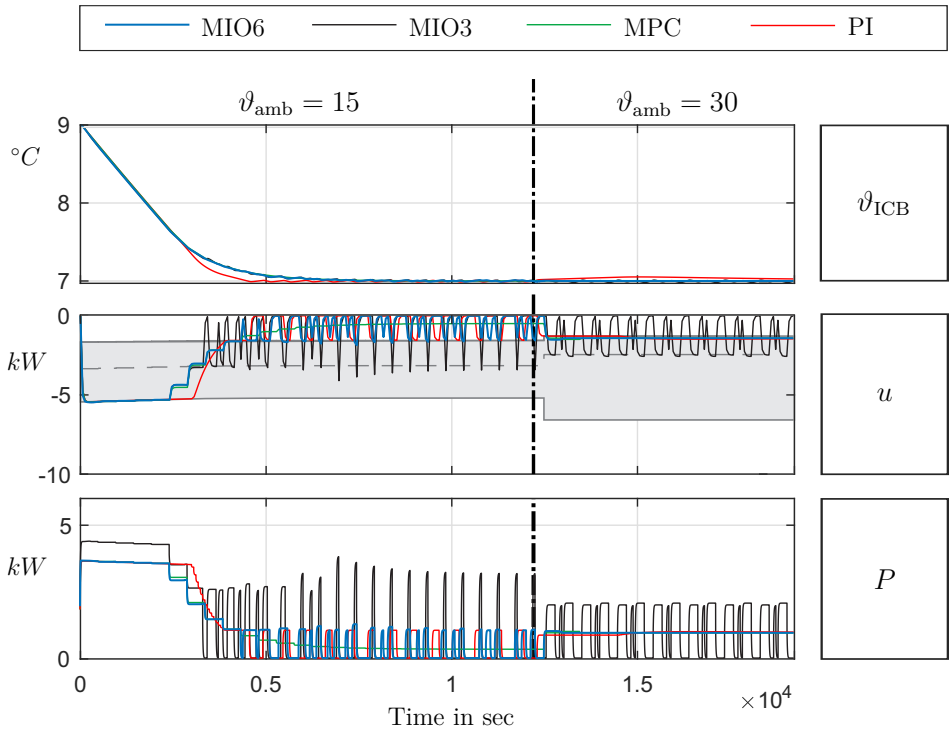

Figure 4.10: Comparison of proposed control method (MIO6-blue), MIO with three large compressors (MIO3-black), with global MPC only (MPC-green), and PI-control plus hysteresis (PI-red).

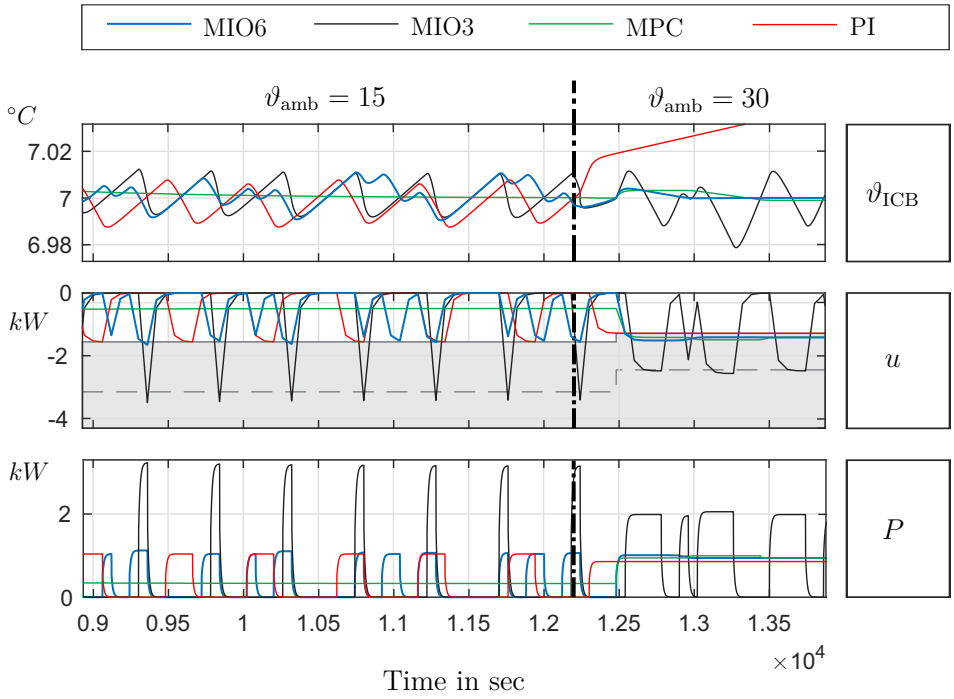

Figure 4.11: Zoom into Fig. 4.10. Switching behavior before and after the ambient step.

tual ICB temperatures is defined as (N being the number of simulation steps)

$$\text{RMSE} = \sqrt{\frac{1}{N}\sum_{k}^{N}\left(\vartheta_{\text{ICB}}(k) - \vartheta_{\text{ICB}}^{\text{ref}}(k)\right)^2}. \tag{4.51}$$

In Table 4.3 the normalized RMSE for t $\geq$ 8000 sec is listed. It can be seen that the RMSE value of MPC is minimal, and MIO6 outperforms MIO3 and PI-control. The PI-controller shows the least effective disturbance compensation as can be seen in

	MIO6	MIO3	MPC	PI
RMSE	1	2.44	0.51	9.11
$E = \int P dt$	1	1.19	1.00	0.99
S	29	84	-	16
sim. time	66.6	16.6	3.87	1.68

Table 4.3: Normalized RMSE and energy consumption E (normalized with MIO6) and switching count S for t $\geq$ 8000 sec, and simulation time for the different control methods.

Fig. 4.11 after the ambient step. This performance could be improved at the cost of

higher power consumption, but in principle some deviation will remain. This puts the minimal switching count and shortest simulation time of the PI-control into perspective as disturbance compensation is the main task of ICB temperature control.
In this specific simulation the MIO3 needs roughly 20% more energy than the other methods. This is mainly due to the poor COP when a large compressor is operated in its minimum power range. Note that the MIO6 utilizes the redundancy of the RCs and solves the control allocation problem by minimizing eq. (4.43), where electrical power is included. In contrast, the PI controller uses a fixed compressor combination stored in a static look-up table, which provides $U(k)$ independent of the electrical power consumption.
The 66.6 sec simulation time of the proposed method for 40 large samples are equivalent to 1.7 sec average computation time for MIO6. This corresponds to 0.3% of the large sample time which can be considered acceptable for real-time implementation.

Solar irradiation

Typically, the ICB is exposed to the sun. Without an irradiation prediction and a irradiation sensor the global MPC has to compensate the heating of the ICB. In Fig. 4.12 measured solar irradiation on a sunny day is shown in the first plot. In the second plot the actual cooling capacity u is shown. The third plot shows that the proposed concept can compensate $\dot{Q}_{\text{sol}}$ and the temperature remains in an acceptable region around the reference temperature value, which is typically $\vartheta_{\text{ICB}}^{\text{ref}} \pm 0.5°\text{C}$. In this simulation the compressor switching count is 740 times in 12h.

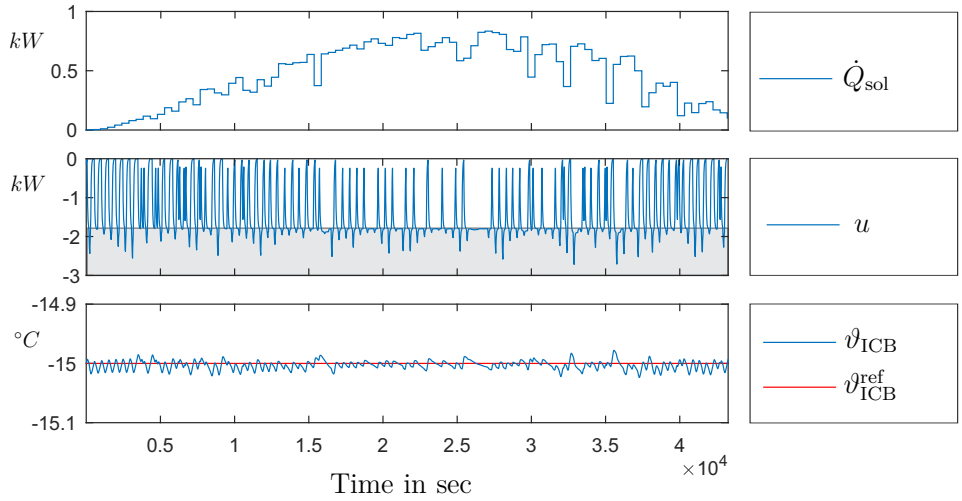

Figure 4.12: Impact of solar irradiation. First plot: A measured irradiation profile for a sunny day. Second plot: The feasible region of u_0 is shown in gray. Third plot: $\vartheta_{\text{ICB}}^{\text{ref}}$ is plotted in red.

RS model errors

Time constant $T_{A,u}$ and the gain $K_{A,u}$ of the RS model are varied to demonstrate the robustness of the controller. A simulation over 19200 sec with two steps in ϑ_{amb} ($15° \nearrow 30° \searrow 0°$) at each third of the simulation time is performed. The output of the perfect model (model 1) is denoted by $\vartheta^{\star}_{\text{ICB}}(K)$ and the output error of all other models is defined as

$$e_{\text{model}}(K) = \vartheta_{\text{ICB,model}}(K) - \vartheta^{\star}_{\text{ICB}}(K). \tag{4.52}$$

Table 4.4 shows the root mean squared output error (RMSE) and the switching count S of the different models. It can be seen that poor modeling of the RS can lead to a significant increase in switching but is compensated effectively by the proposed concept (RMSE always smaller than 0.1).

Model	$\Delta T_{A,u}$ in %	$\Delta K_{A,u}$ in %	RMSE	S
1	0	0	0	62
2	0	30	0.05	116
3	0	-30	0.08	164
4	30	0	0.01	141
5	-30	0	0.01	54
6	30	30	0.05	97
7	-30	-30	0.08	148
8	30	-30	0.09	192
9	-30	30	0.06	91

Table 4.4: RMSE and S for different errors in the RS model.

Robustness with respect to faulty predictions

To demonstrate the robustness of the control concept with respect to faulty predictions a simulation based on an incorrect prediction of $\boldsymbol{\vartheta}^{\text{pred}}_{\text{amb}}$ is made. A random disturbance d_{n}, with increasing variance is added to $\boldsymbol{\vartheta}^{\text{pred}}_{\text{amb}}$ every K-th sample. In Table 4.5 the different variances and the RMSE between the constant reference temperature and the actual ICB temperatures, eq. (4.51), are listed:

σ^2	0	4	25	100
RMSE	0.0074	0.0128	0.0179	0.0364

Table 4.5: RMSE values for different variances.

It can be seen that increasing variances affect the RMSE. Nevertheless, even for large prediction errors the temperature remains in an acceptable region around the reference

temperature value. Typically an acceptable value for the region of tolerance is defined by $\vartheta_{\mathrm{ICB}}^{\mathrm{ref}} \pm 0.5°\mathrm{C}$.
Fig. 4.13 demonstrates the robustness of the control concept. The simulation is plotted over 8 h. After 9600 sec a disturbance d_{n} with $\sigma^2 = 25$ is added to $\boldsymbol{\vartheta}_{\mathrm{amb}}^{\mathrm{pred}}$. After 19200 sec the variance of d_{n} is increased to $\sigma^2 = 100$, shown in the first plot. In the second plot can be seen that d_{n} influences the switching pattern of the MIO, nevertheless the fault is effectively compensated. The third plot shows the ϑ_{ICB} which never exceeds the region of tolerance.

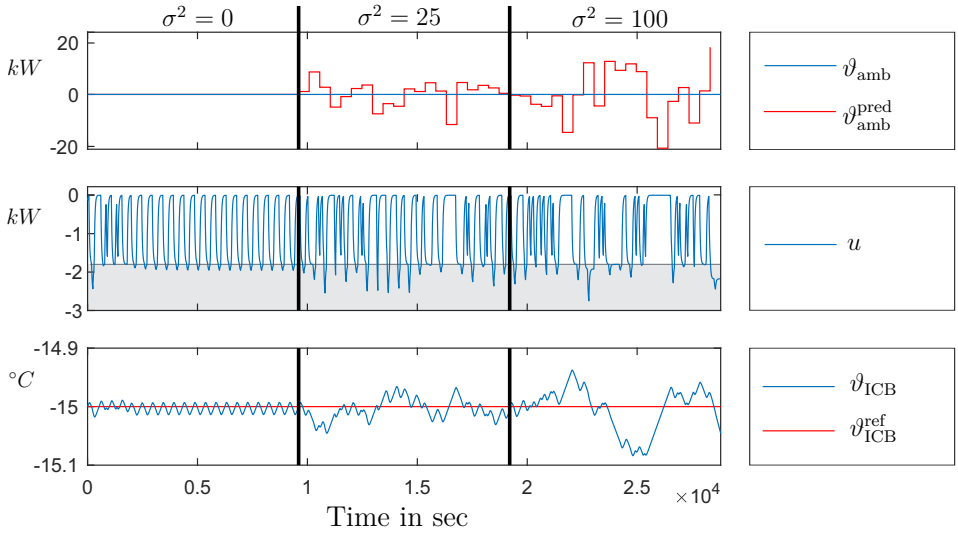

Figure 4.13: Robustness against faulty prediction of $\boldsymbol{\vartheta}_{\mathrm{amb}}^{\mathrm{pred}}$. The third plot shows that ϑ_{ICB} stays in a region of $-15°\mathrm{C} \pm 0.1°\mathrm{C}$.

4.4.10 Limit Cycle

As already visible during steady state in the figures above, a limit cycle occurs in all simulations. In Fig. 4.14 the ICB is cooled from initial condition $\vartheta_{\mathrm{ICB}} = -14°\mathrm{C}$ to the set-point $\vartheta_{\mathrm{ICB}}^{\mathrm{ref}} = -15°\mathrm{C}$. The upper plot shows temperature $\vartheta_{\mathrm{ICB}}(t)$ in blue and $\vartheta_{\mathrm{ICB}}(K)$ in black. The lower plot shows $u_0(k)$ in red and the actual cooling capacity $u(t)$ in blue. In the lower plot it can be seen that from $t = 5000$ sec on a regular switching pattern is visible. Only amplitudes of $u_0(k)$ and accordingly $u(t)$ are consequently slightly adjusted.
In Fig. 4.15 part of the state trajectory $\boldsymbol{x}_{\mathrm{cl}}(t)$ is plotted in blue. The complete state vector of the closed loop is plotted: $\boldsymbol{x}_{\mathrm{cl}} = [u,\ \vartheta_{ICB},\ \Delta\vartheta_{ICB}]^T$. Note that the internal state of the global MPC $\Delta\vartheta_{ICB}$ is only sampled at K and is assumed to be constant between samples. Black circles denote $\boldsymbol{x}_{\mathrm{cl}}(K)$ and the limit cycle $\boldsymbol{x}_{\mathrm{cl}}^*(t)$, eq. (4.48), is plotted in red. The green box represents the estimate for a bound on the limit cycle according to Sections 4.4.7 and A. A zoom into the limit cycle is plotted in Fig. 4.16.

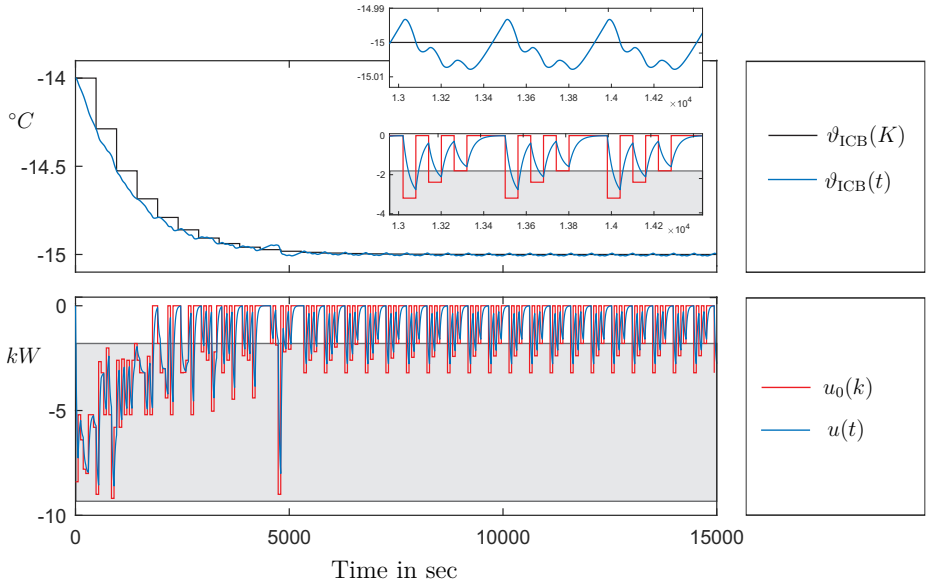

Figure 4.14: Transient simulation to steady-state limit cycle.

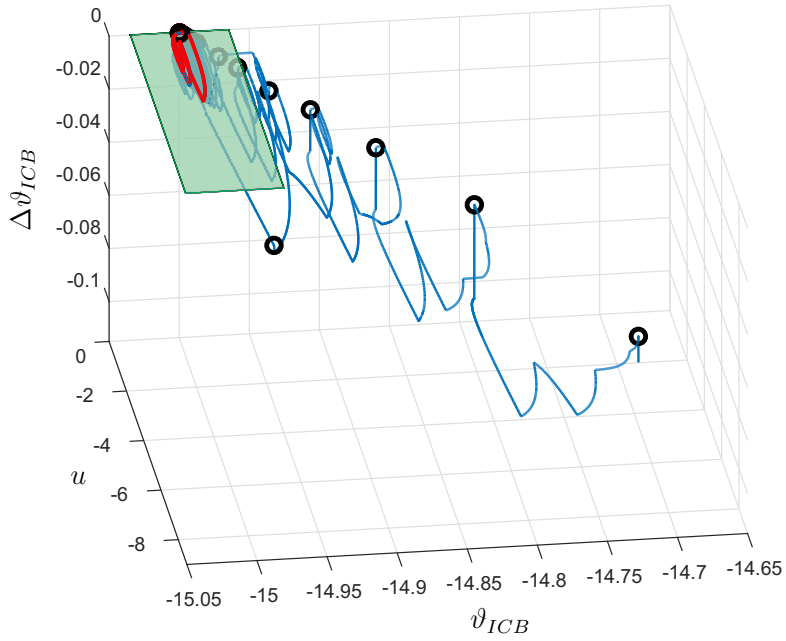

Figure 4.15: Continuous trajectory $\boldsymbol{x}_{\mathrm{cl}}(t)$ (blue), sampled values $\boldsymbol{x}_{\mathrm{cl}}(K)$ (black circles), and limit cycle $\boldsymbol{x}^*_{\mathrm{cl}}(t)$ (red). The green box represents the estimate for a bound on the limit cycle.

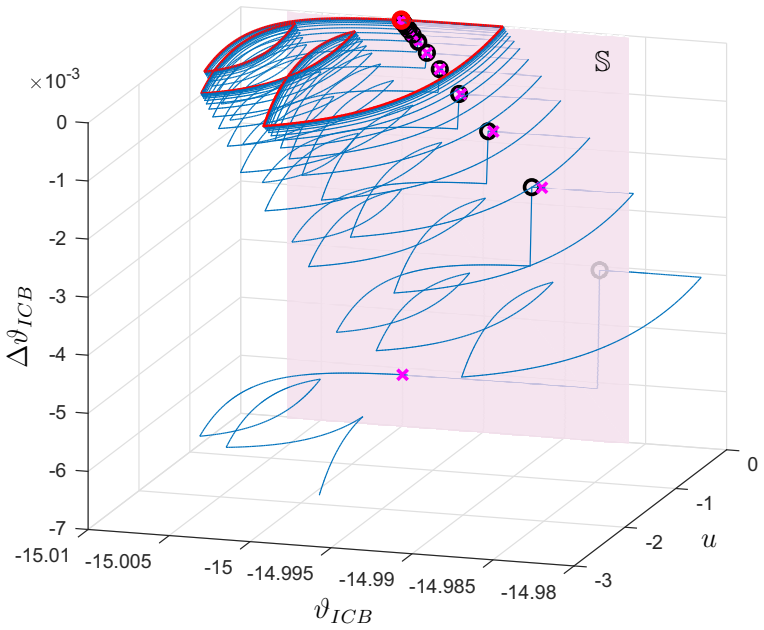

Figure 4.16: Continuous trajectory $\boldsymbol{x}_{\mathrm{cl}}(t)$ (blue), sampled values $\boldsymbol{x}_{\mathrm{cl}}(K)$ (black circles), Poincaré samples $\boldsymbol{x}^q$ (pink crosses), and set-point $\boldsymbol{x}^{\mathrm{ref}}$ (red circle). The Poincaré section $\mathbb{S}$ is a vertical plane plotted in pink.

The set-point is plotted as a red circle, and the asymptotic behavior of the overall system dynamics near the limit cycle is clearly visible. In Fig. 4.16 a Poincaré section $\mathbb{S}$ is plotted in pink: It is a vertical plane through $\boldsymbol{x}^{\mathrm{ref}}$, and the Poincaré samples $\boldsymbol{x}^q$ (intersection of $\boldsymbol{x}_{\mathrm{cl}}(t)$ with $\mathbb{S}$) are plotted as pink crosses. It can be seen that in the vicinity of the set-point the Poincaré samples coincide with the $\boldsymbol{x}_{\mathrm{cl}}(K)$, proving the stability of the limit cycle. As can bee seen in Fig. 4.17 the Poincaré section $\mathbb{S}$ has been selected orthogonal to the (u/ϑ_{ICB})-plane and tangential to the evolution of the $\boldsymbol{x}_{\mathrm{cl}}(K)$ (black circles). For $t \to \infty$ the sequence $\boldsymbol{x}_{\mathrm{cl}}(K)$ actually comes to lie on the sequence $\boldsymbol{x}^q$.

4.5 Comparison of the concepts

In Table 4.6 the differences between the two proposed concepts are shown:
The first concept uses a MI-MPC with moving horizon for the optimization of the control variable. After each small sampling time the solution is calculated again which has higher computational costs then the MIO in concept 2 where the optimization is made once during a large sample. The RS of the concept 1 only has the nonlinear static part of the RS, nevertheless it can easily extended with the dynamic part. In

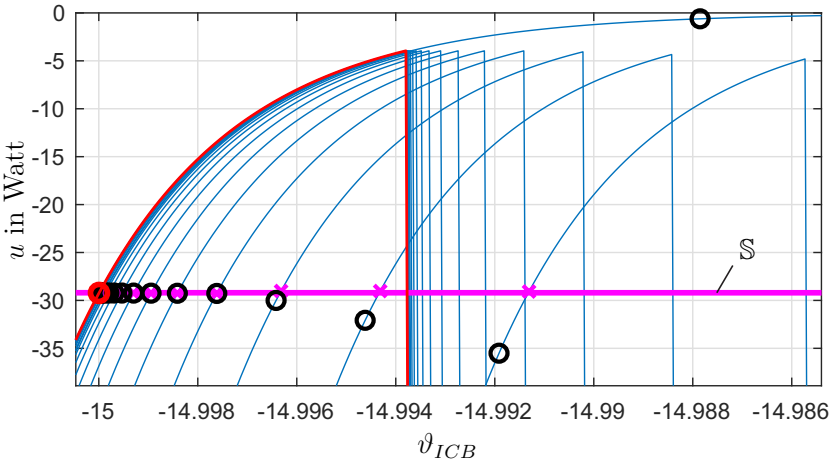

Figure 4.17: Continuous trajectory $\boldsymbol{x}_{\mathrm{cl}}(t)$ (blue), sampled values $\boldsymbol{x}_{\mathrm{cl}}(K)$ (black circles), Poincaré samples $\boldsymbol{x}^q$ (pink crosses), and set-point $\boldsymbol{x}^{\mathrm{ref}}$ (red circle). The Poincaré section $\mathbb{S}$ is a projecting plane visible as pink line.

	Concept 1: Cooling capacity constraint	Concept 2: Predicted temperature constraint
CA	mixed-integer MPC	mixed-integer optimizer
RS model	static nonlinear	Hammerstein
MPC output	cooling capacity $U(K)$	predicted temperature $\vartheta_{\mathrm{ICB}}(K+1)$
MPC constraints	fixed	variable
$\dot{Q}_{\mathrm{sol}}$	not considered	considered

Table 4.6: Differences of the two concepts: Cooling capacity constraint and predicted temperature constraint.

concept 2 the nonlinear static and dynamic part is used in the form of a Hammerstein model. Another difference of the concepts is the output of the MPC. In the first concept the necessary cooling capacity is the output of the MPC. The MI-MPC has to ensure that the average cooling capacity is fulfilled. This control can be easily implemented, nevertheless a deviation of the ICB temperature is possible. A wrong model would also lead to a deviation of the ICB temperature. To avoid these problems, in the second concept the output of the MPC is the predicted temperature at the end of a large sample. The constraint forces the result of the MIO to obtain exactly the same ICB temperature at the end of the large sample as predicted by the global MPC. For a straight forward implementation the MPC of the first concept has fixed constraints for the maximal possible cooling capacity. But the maximal possible cooling capacity depends on the environmental conditions, therefore in concept 2 there is a feedback loop between the MIO and the MPC. The MPC calculates the optimal cooling capacity. If

the constraint is violated, the MI-MPC returns the maximal possible cooling capacity and the MPC calculates the solution again under consideration of the actual constraint. For simplicity the first concept does not include a solar irradiation. Concept 2 has the solar irradiation as unknown disturbance, it can be seen in the simulation results of Section 4.4.9 that the MPC can handle the disturbance without offset.

4.6 Summary

The presented hierarchical MPC control scheme enables the global linear MPC to utilize a long prediction horizon at low computational costs, while the CA provides a predictive multi-objective optimization of the required cooling capacity with both continuous and switched variables. One advantage of the CA compared to Section 3 is the predictive realization of the CA. The main drawback is the higher computational cost. However, due to the hierarchical scheme the computational load of the remaining CA is reduced significantly in comparison to the overall problem. Two different control concepts, constraint formulation, and the communication between the two layers with different sampling times have been presented. Stability and feasibility is discussed, and for the second concept the existence of a limit cycle for steady-state operation has been shown.

Chapter 5

Observer and estimation

In Chapter 4 an MPC for effective temperature control is introduced. However, the strong disturbance of irradiation by the sun can be rarely measured. Furthermore, the aging of the ICB's insulation is a parameter of vital interest for logistic and economic planning although it cannot be directly measured. An important complication is the fact that both of these estimates have the same effect on the measured outputs, and only the use of a proper aging model for α enables the separate reconstruction of the solar irradiation and α, respectively.
Therefore, in this Chapter a unknown input observer (UIO) is used to design a fast sampled disturbance compensation obtaining a fast response of the system. Two specific characteristics of the disturbance are utilized to estimate α: 1) During nighttime solar irradiation has its minimum. 2) α declines at a very slow rate. The MPC, irradiation estimation, and α estimation are implemented with different sampling rates. The separation of the disturbances is obtained by first estimating the excess heat loss of the ICB, and then with the knowledge of the aging model for α splitting up this heat loss into an irradiation part and a part due to aging of the ICB's insulation.

5.1 State of the art

Using an UIO to estimate non-measurable disturbances is well known in literature. Classical state-observers like the Kalman-filter have been used for state-feedback control of a refrigeration system in [82]. In [46] the theory of the Luenberger basic observer is introduced. In [95] a full-order state observer is employed for temperature control of power electronics. The observer concept can also be combined with fault detection and isolation (FDI) methods: A Kalman-filter based FDI concept is presented in [99] for a supermarket refrigeration system; the observer is not only employed to estimate the full state vector but also to estimate the unknown disturbance composed of solar irradiation and declining insulation. A similar approach is presented in [100] where the unknown disturbance is the non-measurable heat input due to ambient air. This enables effective decoupling of the FDI residuals from the non-measurable disturbance. In [12] an UIO

and fault detection filter is combined to ensure that the residual vector has robust and directional properties. A FDI technique for complex power systems is proposed in [1], where where the load fluctuation and output power variation of renewable energy resources are modeled as unknown inputs of the power system. In [106] a fault diagnosis method of an intelligent hydraulic pump system based on a nonlinear unknown input observer is proposed. Different from factors of a full-order Luenberger-type unknown input observer, nonlinear factors are considered in this method. A nonlinear jet engine system is used to illustrate the robust fault isolation approach. In [103] unknown disturbance and model mismatch of a boiler-turbine unit are estimated using an unknown input observer. However, all the aforementioned references do not consider the simultaneous estimation of a model parameter. A hybrid fixed-time observer for state estimation of linear systems is presented in [76], where linear system with unknown inputs and linear system with unknown inputs and parametric uncertainty are analyzed. A unknown input observer and a time-varying parameter estimation is used in [57] to on-line estimate the unknown torque of a vehicle engine.
Parameter estimation in refrigeration or HVAC systems has been presented in [96, 18, 77, 71]. In [18] and [77] only off-line parameter estimation is performed for a refrigeration system and a cold water chiller, respectively. An artificial neural network is utilized in [18] and in [77] different linear models are compared in their validation performance. On-line parameter estimation has been applied to HVAC systems by [96] where recursive least squares with a variable forgetting factor was used to estimate model parameters. In [2] the thermal load of an HVAC system which is treated as a constant unknown disturbance is observed. A similar approach for a building with multiple zones is presented in [62]. An unscented Kalman-filter was used to estimate the thermal parameters of a building model in [71]. In [65] a method for estimating food temperature in supermarket display cases on measurements of air temperature and knowledge of the EXV opening degree. Parameter estimation of heat transfer coefficients for a vehicle has been done in [24]. There an estimation of the heat capacity and heat transfer coefficient for a rail vehicle is provided. The estimation is however based on experimental data from a climatic wind tunnel, which requires special experiments with considerable effort. A complex estimation scheme for a heat transfer coefficient inside an ICE is given in [21]. The method is based on a nonlinear thermodynamical model together with Bayesian estimation schemes and specifically tailored to an ICE. The aging of insulation materials has been mainly investigated for buildings [29, 3] and pipes [13, 101]. These references contain experimental data and partly also analytical models. In [23] a Markov chain based velocity predictor is used to provide a sense of the future disturbances over a stochastic model predictive controller of AC system. The sensitivity of electrified AC plant to solar radiation, ambient temperature, and relative air flow speed is quantitatively analyzed from an energy efficiency perspective.

5.2 Observer and estimation concept

Two different concepts are presented. The first concept has a parallel MPC and observer in feedback loops. Therefore, the estimated disturbance is an additional input to the ICB. The fast sampled observer compensates the disturbance before it affects the MPC. A linear aging model for α is assumed, see [43].
In the second concept the observer estimates the disturbance and a zero order prediction calculates the predicted disturbance. The MPC uses the disturbance prediction for the optimization. The aging model for α is assumed to be a parametric and nonlinear scheme. The concept is extended with predictive maintenance, which is an important feature for managing fleet logistics. Additional, all measured values are affected by measurement noise, see [44].
In both concepts the cooling capacity U which is necessary to hold the desired reference temperature $\vartheta_{\mathrm{ICB}}^{\mathrm{ref}}$ is calculated by the MPC. It is assumed that the desired cooling capacity can always be realized by the RS, therefore $U = u$. Note that a control design for u with the compressor state and electronic expansion valve of the RS as additional control variables is much more involved, see Section 3 and 4.

5.3 Concept 1: Disturbance compensation with Luenberger observer

5.3.1 Overall control structure

In Fig. 5.1 the conceptual architecture of the control structure is shown. The ambient temperature ϑ_{amb} is measured as well as predicted and therefore known for the finite horizon of the MPC. The additional disturbance $\dot{Q}_z$ is not measurable and consequently not available as a predictive disturbance for the MPC. However, with the disturbance observer the current $\dot{Q}_z$ can be estimated and is therefore available for fast sampled disturbance compensation.
The dynamics of the ICB are comparatively slow. Depending on mc_{p}, typically hours pass by to cool down the ICB by 1°C. In contrast $\dot{Q}_{\mathrm{sol}}$ is highly variably during day time. Therefore, the MPC and the disturbance observer utilize two different sampling times.
The MPC optimizes the temperature control of the linear ICB system at a slow sampling rate (samples denoted by K) and provides the required cooling capacity U_{MPC} for the RS. The detailed presentation of the MPC can be found in Section 4.3.3, eqns. (4.1 - 4.32).
The disturbance observer utilizes the fast sampling rate (samples denoted by k) and estimates the state ϑ_{ICB} as well as the disturbance heat flow $\dot{Q}_z$, where $\dot{Q}_{\mathrm{sol}}$ is included; this estimate $\hat{\dot{Q}}_z$ is added to the control variable $u = U_{\mathrm{MPC}} - \hat{\dot{Q}}_z$ which is the input to the ICB.

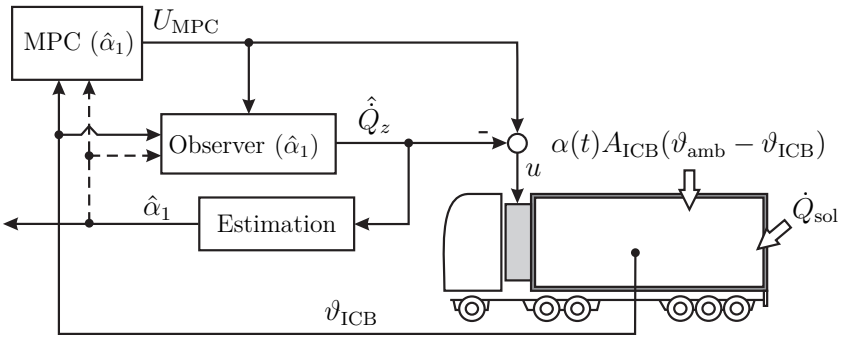

Figure 5.1: Conceptual architecture of the control structure, where $\hat{\alpha}_1$ is the estimation of α_1.

Last, a dedicated estimator identifies the deterioration of α_1. This update is done at widely spaced time intervals (e.g. once in a week) so that the value of $\hat{\alpha}_1$ is assumed to be constant during normal operation. This is justified as the deterioration of α proceeds slowly over time. Thus, $\hat{\alpha}_1$ is developing a step-wise fashion, and for constant $\hat{\alpha}_1$ no adaptive control methods need to be applied.

5.3.2 Disturbance Observer

The main task of the disturbance observer is to estimate the additional heat flow $\dot{Q}_z$ into the ICB. A discrimination between the contribution of solar irradiation $\dot{Q}_{\mathrm{sol}}$ and a deterioration of the heat transfer coefficient α_1 is not possible.
A classical discrete-time Luenberger observer is used [46], with the following structure

$$\hat{\vartheta}_{\mathrm{ICB}}(k+1) = A_P\hat{\vartheta}_{\mathrm{ICB}}(k) + B_P u(k) + E_m\vartheta_{\mathrm{amb}}(k) + G_H C_P(\vartheta_{\mathrm{ICB}}(k) - \hat{\vartheta}_{\mathrm{ICB}}(k)),$$

where $\hat{\vartheta}_{\mathrm{ICB}}(k+1)$ and G_H the observer gain matrix.
The Luenberger observer, eq. (5.1), is augmented with $\hat{\dot{Q}}_z$ to

$$\hat{\vartheta}_{\mathrm{ICB}}(k+1) = A_P\hat{\vartheta}_{\mathrm{ICB}}(k) + B_P u(k) + E_m\vartheta_{\mathrm{amb}}(k) + G_H C_P(\vartheta_{\mathrm{ICB}}(k) - \hat{\vartheta}_{\mathrm{ICB}}(k)) + E_o\hat{\dot{Q}}_z(k), \tag{5.1}$$

and

$$\hat{\dot{Q}}_z(k+1) = \hat{\dot{Q}}_z(k) + G_S C_P(\vartheta_{\mathrm{ICB}}(k) - \hat{\vartheta}_{\mathrm{ICB}}(k)), \tag{5.2}$$

where G_S is the gain for the estimated disturbance, Fig. 5.2.
The estimated disturbance is used as additional control input, Fig. 5.1. Combined with the feed-back control the performance over simple feed-back control is significantly improved whenever there is a major disturbance that can be observed before the slower MPC can react.

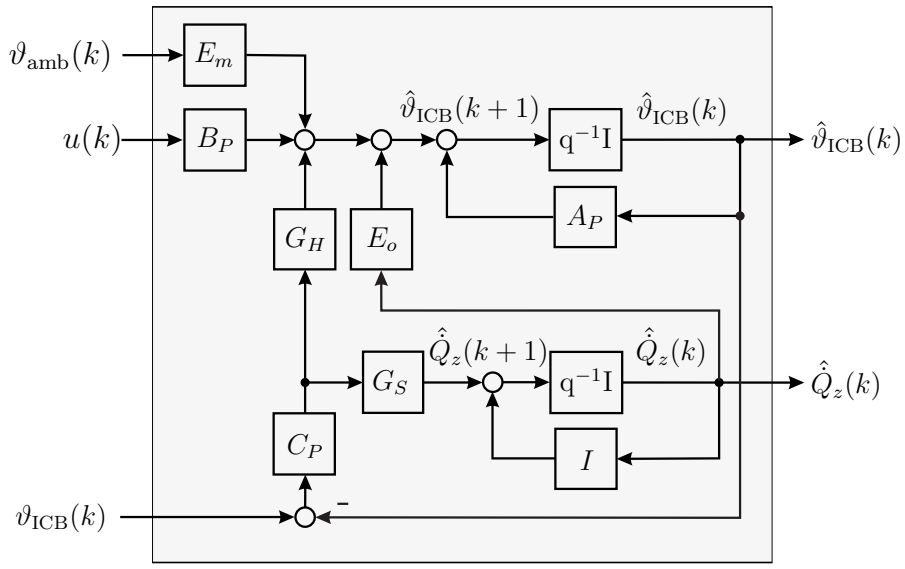

Figure 5.2: Block diagram of the disturbance observer.

5.3.3 Estimation of α

Utilizing the assumption that α is slowly increasing over time and that the heat input of $\dot{Q}_{\mathrm{sol}}$ varies between known maximum and minimum values it is possible to estimate α_1 by a dedicated scheme. Because of the slow increase the estimation is done only once in a week or on a monthly basis.
In order to demonstrate the principle of α-estimation in the remainder the linear model of the AF-50 type [29] is assumed:

$$\alpha(t) = \alpha_0 + \alpha_1 t; \quad \alpha_0, \alpha_1 \in \mathbb{R} \tag{5.3}$$

with α_1 being the constant slope of $\alpha(t)$ over time.
The linear time-discrete model of aging is given by

$$\alpha(k) = \alpha_0 + \hat{\alpha}_1 k t_o, \tag{5.4}$$

where k is the sampling index for the time and t_o is the associated sampling time of the disturbance observer. The estimated disturbance $\hat{\dot{Q}}_z$ can be split up into

$$\hat{\dot{Q}}_z = \hat{\dot{Q}}_{\mathrm{sol}} + \hat{\alpha}_1 k t_o A_{\mathrm{ICB}}(\vartheta_{\mathrm{amb}} - \vartheta_{\mathrm{ICB}}). \tag{5.5}$$

The second term of eq. (5.5) affects $\hat{\dot{Q}}_z$ in such a way that $\hat{\dot{Q}}_z$ exhibits a linear trend due to the increase of α. Thus, the terms of eq. (2.21) can be superimposed as shown in Fig. 5.3.
As the minima of solar irradiation occur during nighttime, a local minimum of $\hat{\dot{Q}}_z$ for every 24 hours can be found. These minima constitute a linear model which corresponds

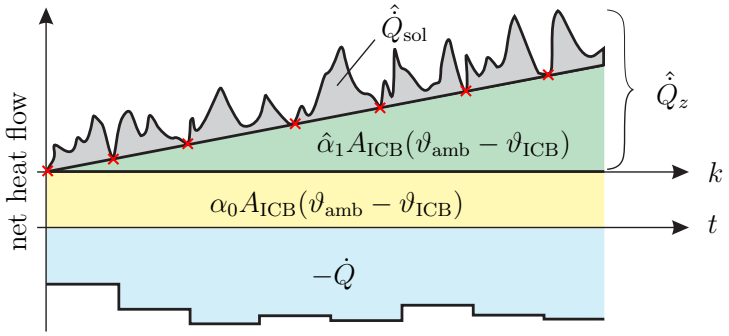

Figure 5.3: Terms of eq. (2.21). The linear trend of $\hat{\alpha}_1$ is visible and data for the linear model of the increase in α are denoted by red crosses.

to the term $\hat{\alpha}_1 A_{\mathrm{ICB}}(\vartheta_{\mathrm{amb}} - \vartheta_{\mathrm{ICB}})$ in eq. (5.5), see Fig. 5.3. For an accurate estimation the whole measured data of the ICB operation are used.
To find the local minimum per day, in the whole measured data every 24h a local minimum is defined. Data for day r are defined as

$$\hat{\boldsymbol{Q}}_z^r = \left[\hat{Q}_z^{(r-1)c+1},\ \hat{Q}_z^{(r-1)c+2},\ \ldots\ \hat{Q}_z^{rc}\right]^T, \tag{5.6}$$

where $c = 14440$ is the number of measurements for one day ($t_o = 1\mathrm{min}$). The local minimum of day r is given by

$$\hat{Q}_{z,\min}^r = \min(\hat{\boldsymbol{Q}}_z^r), \tag{5.7}$$

and the corresponding index is

$$k_{\min}^r = \arg\min(\hat{\boldsymbol{Q}}_z^r). \tag{5.8}$$

The vector of all local minima over n days is defined as

$$\hat{\boldsymbol{Q}}_{z,\min} = \left[\hat{Q}_{z,\min}^1,\ \hat{Q}_{z,\min}^2,\ \ldots\ ,\ \hat{Q}_{z,\min}^n\right], \tag{5.9}$$

with the corresponding vector for the index

$$\boldsymbol{k}_{\min} = \left[k_{\min}^1, k_{\min}^2,\ \ldots\ , k_{\min}^n\right]. \tag{5.10}$$

For every minimum the following equation with the associated index k results

$$\hat{\dot{Q}}_{z,\min}(k) \stackrel{!}{=} \hat{\alpha}_1 k t_o A_{\mathrm{ICB}}(\vartheta_{\mathrm{amb}}(k) - \vartheta_{\mathrm{ICB}}(k)), \tag{5.11}$$

which is written in vector notation for the whole measured data

$$\hat{\dot{\boldsymbol{Q}}}_{z,\min} \stackrel{!}{=} A_{\mathrm{ICB}} t_o \boldsymbol{k}_{\min} \underbrace{\begin{bmatrix} \vartheta_{\mathrm{amb}}(k^1_{\min}) - \vartheta_{\mathrm{ICB}}(k^1_{\min}) \\ \vartheta_{\mathrm{amb}}(k^2_{\min}) - \vartheta_{\mathrm{ICB}}(k^2_{\min}) \\ \vdots \\ \vartheta_{\mathrm{amb}}(k^r_{\min}) - \vartheta_{\mathrm{ICB}}(k^r_{\min}) \\ \vdots \\ \vartheta_{\mathrm{amb}}(k^n_{\min}) - \vartheta_{\mathrm{ICB}}(k^n_{\min}) \end{bmatrix}^T}_{\boldsymbol{X}} \hat{\alpha}_1. \tag{5.12}$$

The linear increase of α_1 is estimated by least squares (LS)

$$\hat{\alpha}_1 = (\boldsymbol{X}^T \boldsymbol{X})^{-1} \boldsymbol{X}^T \hat{\dot{\boldsymbol{Q}}}_{z,\min}, \tag{5.13}$$

where $(\boldsymbol{X}^T \boldsymbol{X})^{-1}$ is proportional to the parameter-error covariance.
Note that if α_0 is unknown it can also be estimated with a slight adaptation. Instead of eq. (5.13) the recursive least squares algorithm may be used.

5.3.4 Robust estimation

The prediction interval (pi) can be used to identify outliers in $\hat{\dot{\boldsymbol{Q}}}_{z,\min}$ so the estimation of $\hat{\alpha}_1$ is not biased. Also already included data $\hat{\dot{Q}}^r_{z,\min}$ can be tested a posteriori with the same method.
The prediction interval of the model output $\hat{\dot{Q}}^0_{z,\min}$ of a regression model at index k_0 is given with a confidence level of $1-\beta$ as

$$pi(\hat{\dot{Q}}^0_{z,\min}, n) = \hat{\dot{Q}}^0_{z,\min} \pm t_{\beta/2,\nu} \hat{\sigma}_e \sqrt{k_0^T (\boldsymbol{X}^T \boldsymbol{X})^{-1} k_0}, \tag{5.14}$$

where $\nu = n_s - p$ with p the number of parameters in the regression model and the estimated residual $\hat{\sigma}_e$

$$\hat{\sigma}_e = \frac{(\hat{\dot{\boldsymbol{Q}}}_{z,\min})^T \hat{\dot{\boldsymbol{Q}}}_{z,\min} - \hat{\alpha}_1 \boldsymbol{X}^T \hat{\dot{\boldsymbol{Q}}}_{z,\min}}{n_s - p} = \frac{\mathrm{SSE}}{n_s - p}, \tag{5.15}$$

where SSE denotes the sum squared error.
Note that constraints $\alpha_{\min} \leq \hat{\alpha}_1 \leq \alpha_{\max}$ for $\hat{\alpha}_1$ can also improve the robust estimation; in that case Lagrange multipliers would be needed in the LS optimization.

5.3.5 Stability of the overall control system

Stability is first shown for the overall system with the single sampling frequency of the MPC (denoted by K). The augmented state equation of the ICB is given by eq. (4.1).

Setting $\vartheta_{\text{amb}} = 0$ and adding the additional control input from the disturbance observer $\hat{\dot{Q}}_z$ the following state equation results:

$$\boldsymbol{x}_{\text{MPC}}(K+1) = \boldsymbol{A}_a \boldsymbol{x}_{\text{MPC}}(K) + \boldsymbol{B}_a \Delta U(K) + \boldsymbol{E}_a \hat{\dot{Q}}_z(K). \tag{5.16}$$

In the unconstrained case the control input of the MPC $\Delta U_K = U(K) - U(K-1)$ can be written as

$$\Delta U(K) = \boldsymbol{K}_{\text{MPC}} \boldsymbol{x}(K), \tag{5.17}$$

where the constant feedback matrix $\boldsymbol{K}_{\text{MPC}}$ is defined by the controller matrices, [94]:

$$\boldsymbol{K}_{\text{MPC}} = [1 \;\; 0](\boldsymbol{F}_u^T \boldsymbol{F}_u + \boldsymbol{R}_2)^{-1} \boldsymbol{F}_u^T \boldsymbol{F}_x. \tag{5.18}$$

Reformulating the observer dynamics introduced in Section 5.3.2 with the estimation error $\tilde{x}_P(K) = x_P(K) - \hat{x}_P(K)$ yields

$$\tilde{x}_P(K+1) = (A_P - HC_P)\tilde{x}_P(K), \tag{5.19}$$

and the dynamics of the unknown disturbance are

$$\hat{\dot{Q}}_z(K+1) = \hat{\dot{Q}}_z(K) + G_S C_P \tilde{x}_P(K). \tag{5.20}$$

Thus, using state vector $\boldsymbol{x}_{cl} = [\boldsymbol{x}_{\text{MPC}} \;\; \tilde{x}_P \;\; \hat{\dot{Q}}_z]^T$ the closed-loop state equation of the overall system is given by

$$\boldsymbol{x}_{cl}(K+1) = \begin{bmatrix} (\boldsymbol{A}_a + \boldsymbol{B}_a \boldsymbol{K}_{\text{MPC}}) & \boldsymbol{0} & \boldsymbol{E}_a \\ 0 & (A_P - G_H C_P) & 0 \\ 0 & G_S C_P & 1 \end{bmatrix} \boldsymbol{x}_{cl}(K). \tag{5.21}$$

Matrices $\boldsymbol{K}_{\text{MPC}}$, H, and S can be chosen such that the closed-loop eigenvalues yield a stable system with desired dynamics. Eq. (5.21) is just the basis for a stability analysis, a design procedure for guaranteed stability would require further work.
The actually higher sampling frequency of the disturbance observer will not pose a problem if 1) the MPC output is kept constant until the next K, and 2) the estimated $\hat{\dot{Q}}_z$ is correctly down-sampled at time instances K. Then the above given derivation will hold as the disturbance observer must be designed stable anyways.
Note that α is kept constant for most of the time and does not pose a stability problem. Only during the small step-wise changes of α stability could be an issue; however, methods for piece-wise affine systems exist, which can be used for stability analysis, [37].

5.3.6 Simulation results

Results of closed-loop simulations are used to demonstrate the concept. The method and the results have been published in [43].
Note that typically durations for a food transport system are less than a week, nevertheless to see the effect of aging the simulation is made over a longer time span. The model parameters for the simulation results are given in the Table 5.1.

Parameter	Value	Parameter	Value
N	131040 min	$u_{\max}$	9 kW
t_S	1 min	A_{ICB}	163.5 m^2
T_S	8 min	mc_{p}	8.8e6 J/K
α_0	0.4 $\text{W}/\text{m}^2\text{K}$	G_S	10000
$\alpha_{N_{\text{sim}}}$	0.5 $\text{W}/\text{m}^2\text{K}$	G_H	2
ϑ_{amb}	30 ° C		

Table 5.1: Model parameters for the simulation

It is assumed that α increases linear over time, from α_0 to $\alpha_{N_{\text{sim}}}$, where N is the simulation duration, which corresponds to three months. The solar irradiation data is taken from real measured data, [59]. In Fig. 5.4 a comparison between the simulation with disturbance estimation versus the simulation with standard MPC control is shown. The simulation duration is 28 days. The first plot shows the cooling capacity (control variable) in kW. The second plot shows the ICB temperature. Typically a variation of $\pm 0.5°$ C is an acceptable range for the temperature control. It can be seen that the MPC without disturbance estimation is not able to hold the desired set temperature in the acceptable range. The same MPC with the disturbance observer can significantly decrease the variation and remains well within the acceptable range. The third plot shows the actual solar irradiation and the estimated solar irradiation together with the impact of the increasing α.
The RMSE between the desired set temperature and the actual ICB temperatures is defined as

$$\text{RMSE} = \sqrt{\frac{1}{N}\sum_{k=1}^{N}\left(\vartheta_{\text{ICB}}(k) - \vartheta_{\text{ICB}}^{\text{ref}}(k)\right)^2}. \tag{5.22}$$

In Table 5.2 the normalized RMSE is listed. It can be seen that the RMSE is reduced by approximately 90%.

	without obs.	with obs.
RMSE	1	0.097

Table 5.2: Normalized RMSE values with and without observer.

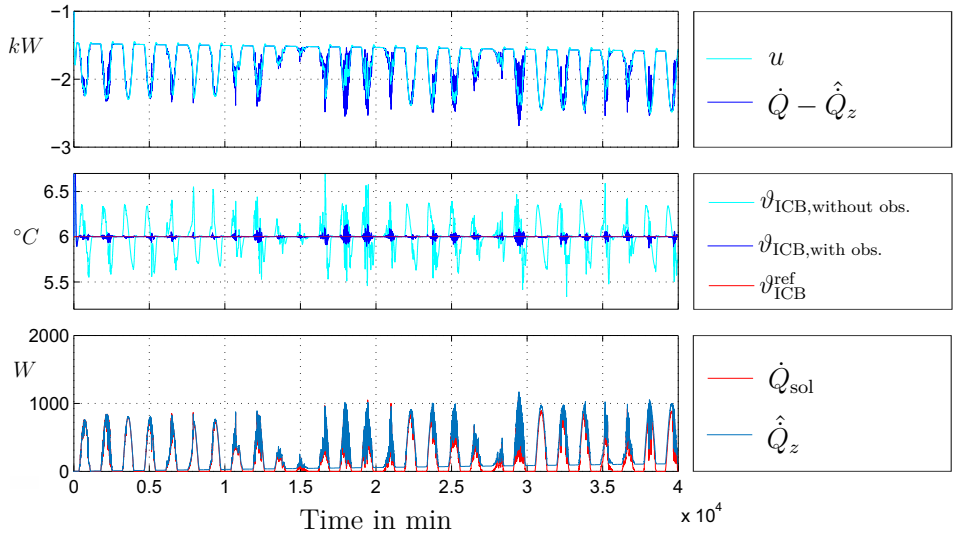

Figure 5.4: Comparison between standard MPC and MPC with disturbance observer.

In Fig 5.5 the solar irradiation and the observed disturbance is shown for 91 days. The linear increase of α can be clearly seen in the estimated disturbance. Note that the observer estimate $\hat{\dot{Q}}_z$ comprises both the effects of irradiation and increasing α.

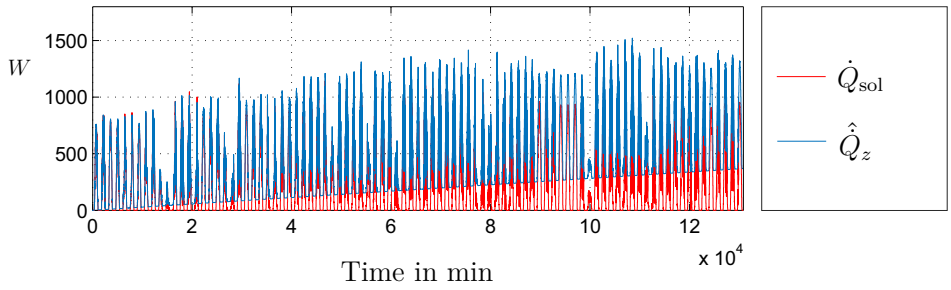

Figure 5.5: Solar irradiation $\dot{Q}_{\text{sol}}$ and estimated disturbance $\hat{\dot{Q}}_z$. The trend of $\hat{\dot{Q}}_z$ is caused by the increase of α due to aging.

The estimated disturbance $\hat{\dot{Q}}_z$ over 12 days is plotted in Fig. 5.6. The local minima identified by the method from Section 5.3.3 are denoted by a red cross. Also here the linear trend of $\hat{\dot{Q}}_z$ can be seen. Note that in this case all minima come to lie within the prediction interval and are therefore included in the estimation of α_1.
In Fig. 5.7 the identified $\hat{\alpha}_1$ value is shown together with the actual increase of α. Because of the slow increase of α an update approximately every 14 days (2.10^4 min) is accurate enough. At the update instances α is estimated quite accurately, however, for a sufficiently performing ICB model in the MPC and observer the error in between is completely acceptable.

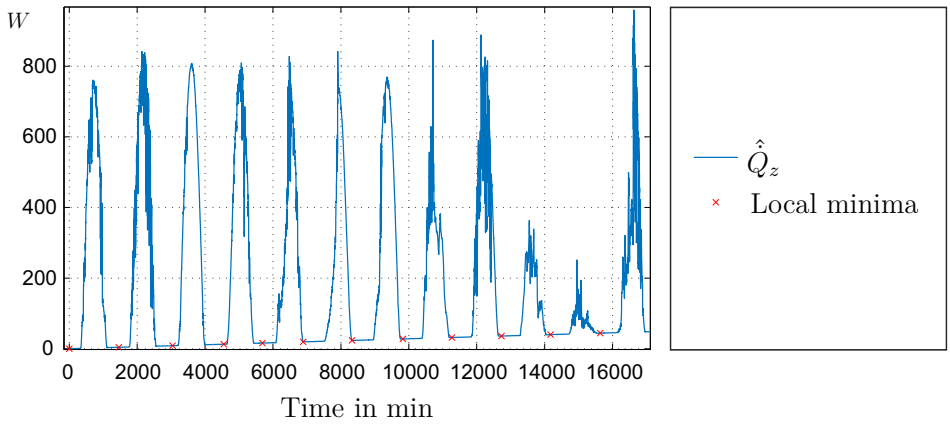

Figure 5.6: The estimated disturbance of the observer $\hat{\dot{Q}}_z$ with all local minima during nighttime (red crosses).

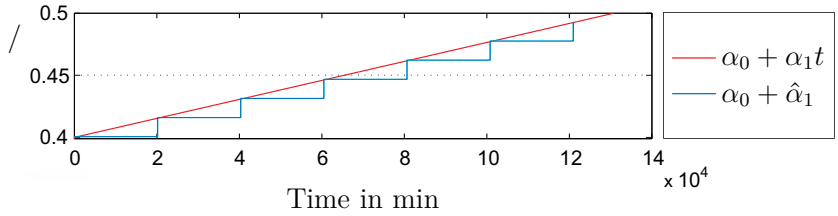

Figure 5.7: Comparison of the estimated (blue) and real (red) α.

Note that $\hat{\dot{Q}}_z$ will be estimated accurately in steady-state even for a biased α-estimate, as the observer has integral behavior for estimating $\hat{\dot{Q}}_z$.

5.4 Concept 2: Full state observer with nonlinear estimation

5.4.1 Overall control structure

The conceptual architecture can be divided into four main blocks, Fig. 5.8.

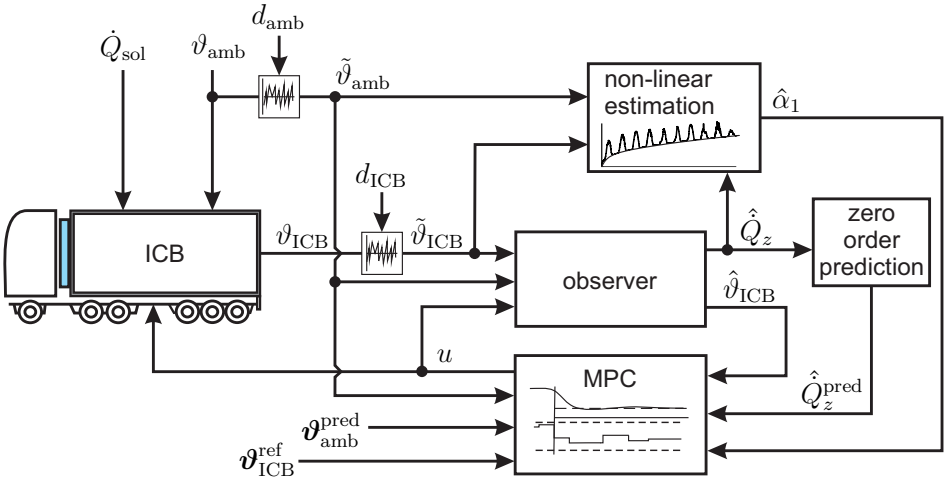

Figure 5.8: Conceptual architecture of the control structure including an MPC, full state observer, a zero order disturbance prediction and a nonlinear estimation of the aging parameter $\hat{\alpha}_1$.

For the sake of simplicity in this Chapter the sampling frequency of the MPC is chosen to be the same as the observer sampling frequency and therefore $K = k$. The observer estimates the temperature of the ICB $\hat{\vartheta}_{\mathrm{ICB}}$ and the unknown disturbance $\hat{\dot{Q}}_z$. The inputs for the observer are the necessary cooling capacity u of the MPC, the measured ambient temperature $\tilde{\vartheta}_{\mathrm{amb}}$ and the measured temperature of the ICB $\tilde{\vartheta}_{\mathrm{ICB}}$. Both measurements are affected by measurement noise d_{amb} and d_{ICB}, respectively.
The nonlinear identification estimates the deviation of the heat transfer coefficient $\hat{\alpha}_1$. The inputs to the identification block are $\tilde{\vartheta}_{\mathrm{amb}}$, $\tilde{\vartheta}_{\mathrm{ICB}}$ and $\hat{\dot{Q}}_z$.
The zero order prediction block forecasts the future disturbance $\hat{\dot{Q}}_z^{\mathrm{pred}}$, which is an input to the MPC. With $\hat{\dot{Q}}_z^{\mathrm{pred}}$, the predicted ambient temperature $\vartheta_{\mathrm{amb}}^{\mathrm{pred}}$, the reference temperature of the ICB $\vartheta_{\mathrm{ICB}}^{\mathrm{ref}}$ and $\tilde{\vartheta}_{\mathrm{ICB}}$ the MPC calculates the optimal cooling capacity u to hold the desired reference temperature of the ICB.

5.4.2 Estimation of α

Nonlinear estimation

For the estimation of α a parametric model with a nonlinear optimization is used. The main idea is to fit the nonlinear aging model to $\dot{Q}_z$, which enables the separation of $\dot{Q}_\alpha$ and $\dot{Q}_{\text{sol}}$.
With eqns. (2.21) and (2.24) the estimated heat input $\dot{Q}_{\hat{\alpha}}$ can be written as

$$\dot{Q}_{\hat{\alpha}}(\boldsymbol{\theta}_\alpha) = f_\alpha(\boldsymbol{\theta}_\alpha, t)\boldsymbol{x}_\alpha, \tag{5.23}$$

where $\boldsymbol{x}_\alpha$ is the regressor vector

$$\boldsymbol{x}_\alpha = \left[A_{\text{ICB}}(\tilde{\boldsymbol{\vartheta}}_{\text{amb}} - \tilde{\boldsymbol{\vartheta}}_{\text{ICB}})\right], \tag{5.24}$$

with $\tilde{\boldsymbol{\vartheta}}_{\text{amb}}$ and $\tilde{\boldsymbol{\vartheta}}_{\text{ICB}}$ the vectors of all past values.
The optimization criterion for $f_\alpha(\boldsymbol{\theta}_\alpha, t)$ is defined as

$$J_\alpha = \gamma \sum_k \|\dot{Q}_z - \dot{Q}_{\hat{\alpha}}\| + (1-\gamma)(\dot{Q}_z - \dot{Q}_{\hat{\alpha}})\epsilon_2, \tag{5.25}$$

where γ is the weighting factor ($0 \leq \gamma \leq 1$) and ϵ_2

$$\epsilon_2 = \begin{cases} 1 & \dot{Q}_z - \dot{Q}_{\hat{\alpha}} < 0 \\ 0 & \text{else.} \end{cases} \tag{5.26}$$

The corresponding optimization problem is formally stated as

$$J_\alpha^\star = \min_{\boldsymbol{\theta}_\alpha} J_\alpha, \tag{5.27}$$

and the optimal value of $\boldsymbol{\theta}_\alpha$ is given by

$$\boldsymbol{\theta}_\alpha^\star = \arg\min_{\boldsymbol{\theta}_\alpha} J_\alpha^\star. \tag{5.28}$$

With the result of the optimization, eq. (5.28), the estimation of $\hat{\alpha}_1$ is made,

$$\hat{\alpha}_1 = f_\alpha(\boldsymbol{\theta}_\alpha^\star, t). \tag{5.29}$$

Note that eq. (5.28) defines an infimum to $\dot{Q}_z$ if γ in eq. (5.25) is properly selected. This infimum is assumed to be constituted by $\dot{Q}_{\hat{\alpha}}$. For $\gamma = 1$ the resulting $\dot{Q}_{\hat{\alpha}}$ will be just some average of $\dot{Q}_z$, see Fig. 5.9.

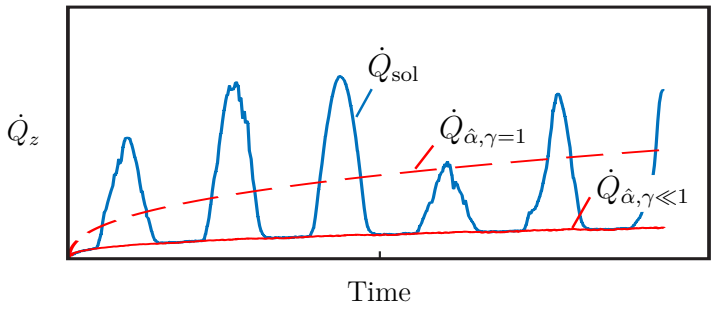

Figure 5.9: Total disturbance $\dot{Q}_z$ and separation of $\dot{Q}_{\mathrm{sol}}$ and $\dot{Q}_{\hat{\alpha}}$ with two different weighting factor values of γ in the optimization criterion J_α.

Detection of changes

Accidental damage to the interior or exterior cover sheet of the ICB is quite common in normal operation. Punctures and fissures allow moisture to enter and diffuse within the isolation material at a much higher rate. This causes a significant acceleration of the deterioration of the α-value, see Fig. 5.10. In terms of the aging model, eq. (2.24), this means a sudden change in the parameter values $\boldsymbol{\theta}_\alpha$. It is assumed, that the aging model is also valid in this case, however the independent variable τ is now constituted by $\tau = t - t_{\mathrm{ch}}$ and $\alpha(t) = \alpha_{\mathrm{ch}} + \alpha(\tau)$ for $t >= t_{\mathrm{ch}}$. This corresponds to a shift of the coordinate origin to $(t_{\mathrm{ch}}, \alpha_{\mathrm{ch}})$.
In order to detect such a change an additional local aging model can be fitted to data from a moving window. This moving window ends at the current sample and starts at t_{hist} in the past. The model fit in terms of the mean square error (MSE) is computed

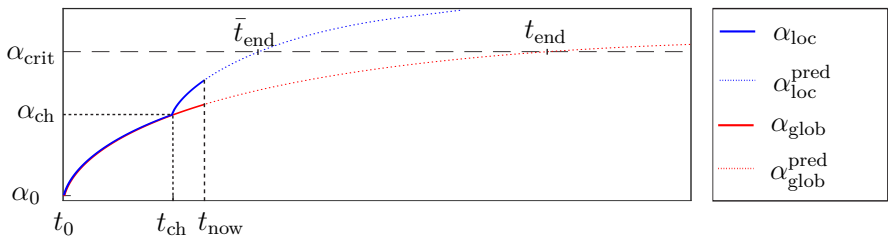

Figure 5.10: Deterioration of α_1 and prediction of reaching the critical value at t_{end} or rather $\bar{t}_{\mathrm{end}}$. The current time is denoted with t_{now} and the corresponding changing time is denoted with t_{ch}, which is then the new start point of the new global model.

for both the global (J_{glob}) and the local model (J_{loc}):

$$J_{\text{glob}} = \frac{1}{t_{\text{hist}}} \sum_{i=1}^{t_{\text{hist}}} (\hat{\dot{Q}}_z - \hat{\alpha}_{1,\text{glob}} A_{\text{ICB}} (\tilde{\vartheta}_{\text{amb}} - \tilde{\vartheta}_{\text{ICB}}))^2, \tag{5.30}$$

$$J_{\text{loc}} = \frac{1}{t_{\text{hist}}} \sum_{i=1}^{t_{\text{hist}}} (\hat{\dot{Q}}_z - \hat{\alpha}_{1,\text{loc}} A_{\text{ICB}} (\tilde{\vartheta}_{\text{amb}} - \tilde{\vartheta}_{\text{ICB}}))^2. \tag{5.31}$$

Note that $\hat{\alpha}_{1,\text{glob}}$ and $\hat{\alpha}_{1,\text{loc}}$ is computed according to eq. (5.29). A sudden parameter change is detected if $J_{\text{loc}} < J_{\text{glob}}$, and the first sample of the respective moving window is assumed to be the associated sampling instance. Additionally, a more accurate estimate of this sampling instance can be obtained by performing the above described comparison on a finer sampling within the detected interval. The local model is now considered being the new global model, and the procedure continues. Note that this extension guarantees updated predictions for end-of-life, see Fig. 5.10 (new expected value $\bar{t}_{\text{end}}$ replacing former value t_{end}).
A similar result could be obtained by an exponential weight decay on past data, however, sudden changes would just lead to an asymptotic fit of the new model, and the time of the sudden change would remain unclear.

Predictive maintenance

The aging model presented in Section 5.4.2 enables an effective application of predictive maintenance. If some α_{crit} is defined for service, re-certification or end-of-life, a prediction of the model can be used to estimate the respective time t_{end}, see Fig. 5.10. Note that the detection of changes explained in Section 5.4.2 is an important feature, as it can timely predict a significant reduction of service life (reduction from t_{end} to $\bar{t}_{\text{end}}$ in Fig. 5.10). This is an important feature for managing fleet logistics by reducing costs and maximizing availability.
The prediction of the aging model is uncertain due to parameter estimation based on noisy measurement data. Because of the generally nonlinear model structure and the nonlinear parameter optimization no analytic estimate of the parameter and output covariance is possible. Nevertheless, based on fleet data an estimate of a non-parametric probability density can be obtained for both the output uncertainty and the uncertainty of the critical point in time t_{end}. Depending on the aging model and the available data this uncertainty can become large especially for the critical point in time t_{end}.

5.4.3 Plant model

As the plant model, eq. (2.20), is linear for a constant α the state, input, and disturbances, respectively, are defined as absolute values: $x(k) = \vartheta_{\text{ICB}}(k)$ and $\boldsymbol{z} = \left[z_m(k), z_o(k)\right]$ where $z_m(k) = \tilde{\vartheta}_{\text{amb}}(k)$ describes the measured disturbances and $z_o(k)$

describes unknown disturbances. The corresponding discrete state-space description from eq. (2.23) is given by:

$$\begin{aligned} x_P(k+1) &= A_P x_P(k) + B_P u(k) + E_m z_m(k) + E_o z_o(k) \\ y_P(k) &= C_P x_P(k). \end{aligned} \tag{5.32}$$

5.4.4 Observer

Current observer structure

For ensure offset-free control an MPC is augmented with a disturbance model which is used to estimate and predict the mismatch between measured and predicted outputs, [47],

$$\begin{aligned} \hat{x}_P(k+1) &= A_P \hat{x}_P(k) + B_P u(k) + E_m z_m(k) + E_o \hat{z}_o(k) \\ \hat{z}_o(k+1) &= \hat{z}_o(k) \\ \hat{y}_P(k) &= C_P \hat{x}_P(k) + C_z \hat{z}_o(k), \end{aligned} \tag{5.33}$$

where C_z is the disturbance input vector (which is zero in the specific application) and $\hat{z}_o(k)$ is the observed disturbance. In order to instantaneously react to a step-wise change in $z_o(k)$ an observer formulation is used that provides a current estimator based on the most recent measurements of $y_P(k)$, [68]

$$\hat{x}_P(k+1) = A_P \bar{x}_P(k) + L_1(y_P(k) - C_P \bar{x}_P(k)), \tag{5.34}$$

$$\hat{z}_o(k+1) = \bar{z}_o(k) + L_2(y_P(k) - C_P \bar{x}_P(k)), \tag{5.35}$$

$$\bar{x}(k+1) = A_P \bar{x}_P(k) + B_P u(k) + E_m z_m(k) + E_o \hat{z}_o(k) + A_P L_1(y_P(k) - C_P \bar{x}_P(k)), \tag{5.36}$$

$$\bar{z}_o(k+1) = \bar{z}_o(k) + A_P L_2(y_P(k) - C_P \bar{x}_P(k)). \tag{5.37}$$

Parametrization

For the optimal pole selection of $\boldsymbol{L} = \begin{bmatrix} L_1 & L_2 \end{bmatrix}$ an optimization of the RMSE of $\hat{x}_p = \hat{\vartheta}_{\mathrm{ICB}}$ is made:

$$J_L = \sqrt{\frac{1}{N} \sum_{k=1}^{N} (\vartheta_{\mathrm{ICB}}^{\mathrm{ref}}(k) - \hat{\vartheta}_{\mathrm{ICB}}(k))^2}.$$

The corresponding optimization problem is formally stated as

$$J_L^\star = \min_{\boldsymbol{\theta}_L} J_L, \tag{5.38}$$

where $\boldsymbol{\theta}_L = \begin{bmatrix} L_1, & L_2 \end{bmatrix}^T$ in eqns. (5.34 - 5.37), and the optimal value of $\boldsymbol{\theta}_L$ is given by

$$\boldsymbol{\theta}_L^\star = \arg\min_{\boldsymbol{\theta}_L} J_L^\star. \tag{5.39}$$

A simulation with three representative solar irradiations over summer days is used for the optimization. The simulation includes a sunny day, a sunny day with clouds and a very cloudy day, see Fig. 5.11.

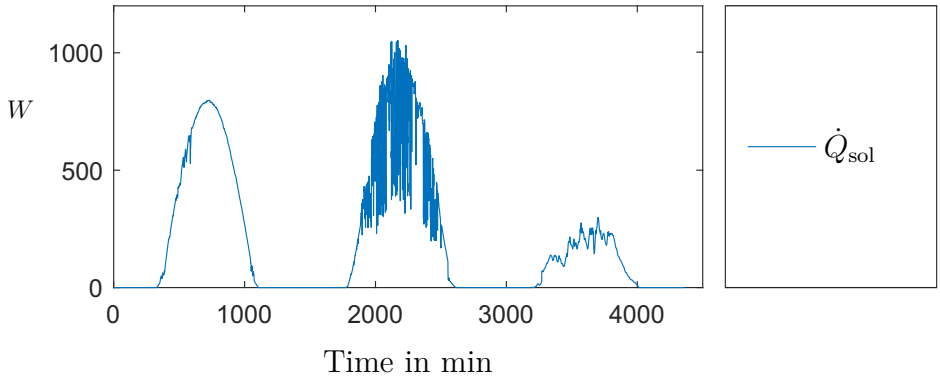

Figure 5.11: Solar irradiation which is used for tuning the observer poles.

Note that noise d_{ICB} on the measured temperature $\tilde{\vartheta}_{\mathrm{ICB}}$ implicitly enters the optimization. Thus, the optimal estimate $\boldsymbol{\theta}_L^{\star}$ represents a trade-off between speed and noise rejection of the observer.

5.4.5 MPC formulation

Based on the state-space model, eq. (5.32), the future state variables are calculated sequentially using the set of future control inputs $\boldsymbol{u}$,

$$\boldsymbol{u}(k) = \Big[u(k), \quad u(k+1), \quad \ldots, \quad u(k+N_c-1)\Big]^T, \tag{5.40}$$

The dimension of $\boldsymbol{u}(k)$ is (N_p x 1), if $N_c < N_p$ the remaining $N_p - N_c$ values of $\boldsymbol{u}(k)$ are filled with the value of $u(k+N_c-1)$.
The prediction of the ambient temperature is defined as

$$\hat{\boldsymbol{z}}_m^{\mathrm{p}}(k) = \Big[\vartheta_{\mathrm{amb}}^{\mathrm{pred}}(k|k), \quad \vartheta_{\mathrm{amb}}^{\mathrm{pred}}(k+1|k), \quad \ldots, \quad \vartheta_{\mathrm{amb}}^{\mathrm{pred}}(k+N_p-1|k)\Big]^T. \tag{5.41}$$

For the prediction $\hat{\boldsymbol{z}}_o^{\mathrm{p}}(k)$ a constant prediction of $\dot{Q}_z^{\mathrm{pred}}$ is assumed, which yields to

$$\hat{\boldsymbol{z}}_o^{\mathrm{p}}(k) = \dot{Q}_z^{\mathrm{pred}} = \Big[\hat{z}_o(k-1), \quad \hat{z}_o(k-1), \quad \ldots, \quad \hat{z}_o(k-1)\Big]^T_{(1\mathrm{x}N_p)}. \tag{5.42}$$

The reference trajectory $\boldsymbol{Y}^{\mathrm{ref}}(k)$ is defined in eq. (4.13).

The optimization criterion for an offset-free MPC is chosen as, [47]

$$\begin{aligned}
\min_{\boldsymbol{u}(k)} ||\hat{x}_P(N_p) - x_{ss}||^2_{P_R} \quad &+ \quad \sum_{i=k}^{k+N_p-1} ||\hat{x}_P(i) - x_{ss}||^2_{R_1} + ||u(i) - u_{ss}||^2_{R_2} \qquad (5.43)\\
\text{s.t.} \quad & \\
\hat{x}_P(k+1) &= A_P\hat{x}_P(k) + B_P u(k) + E_m\hat{z}^{\mathrm{p}}_m(k) + E_o\hat{z}^{\mathrm{p}}_o(k),\ k = 0, ..., N_p\\
\hat{z}_o(k+1) &= \hat{z}_o(k),\ k = 0, ..., N_p\\
0 &\leq u(k) \leq u_{\max},\ k = 0, ..., N_p
\end{aligned}$$

where $u_{\max}$ is the maximal available cooling capacity of the RS, R_1, R_2 are positive semi-definite weighting factors, which are used for tuning, P_R satisfies the discrete-time Riccati equation

$$P_R = A_P^T P_R A_P - (A_P^T P_R B_P)(B_P^T P_R B_P + R_2)^{-1}(B_P^T P_R A_P) + R_1, \qquad (5.44)$$

and with x_{ss} and u_{ss} given by, [47]

$$\begin{bmatrix} A_P - I & B_P \\ C_P & 0 \end{bmatrix} \begin{bmatrix} x_{ss} \\ u_{ss} \end{bmatrix} = \begin{bmatrix} -E_o\hat{z}_o(k) \\ Y^{\mathrm{ref}}(k) - C_z\hat{z}_o(k) \end{bmatrix}. \qquad (5.45)$$

Note that a solar irradiation model for predicting the daily irradiation, eq. (5.42), could also be used, e.g. the ASHRAE model [22]. However, with the data which is used in this paper no improvement could be achieved with a model of higher order, therefore the constant prediction is used, which is less complex and faster. If reliable irradiation predictions from a weather service are available an improvement over the proposed simple model can be expected. Also intelligent operation strategies, based on stochastic MPC algorithm augmented with a probabilistic time series autoregressive model that is used to quantify solar irradiance uncertainty using sky-cover forecasts can be used, see [39].

5.4.6 Stability of the overall control system

The main structure of the control system according to Fig. 5.8 consists of a linear MPC and a linear state observer. In the case of unconstrained MPC closed-loop stability is known to exist if both characteristic polynomials of the current observer

$$P_{\mathrm{obs}}(z, \boldsymbol{L}) = \det[zI - (A_P - \boldsymbol{L}C_P A_P)], \qquad (5.46)$$

and MPC

$$P_{\mathrm{MPC}}(z, G_{\mathrm{FB}}) = \det[zI - (A_P - B_P G_{\mathrm{FB}})], \qquad (5.47)$$

with the constant feedback matrix G_{FB}, which is defined by the controller matrices, [94], respectively, have eigenvalues inside the unit circle. Furthermore, due to the separation principle dynamics of the observer and the MPC can be chosen independently, [68].

In the case of constrained MPC stability analysis is more involved and can be based on the concept of the terminal set, [33].
Note that the zero order prediction of the disturbance $\hat{\dot{Q}}_z$ does not contain any dynamic behavior and therefore does not affect stability characteristics.
However, the nonlinear identification of $\hat{\alpha}_1$ renders the implicit model of the MPC time-variant. This results in an adaptive control scheme. Nevertheless, the estimate $\hat{\alpha}_1$ is kept constant for a considerable duration (e.g. 14 days) and is then set to the current estimated value. Because of this step-wise change in the model parameter $\hat{\alpha}_1$ the structure of the time-varying MPC can be interpreted as a piecewise affine system, [55]. For such systems stability can be proven by finding a suitable common quadratic Lyapunov function. Such a function can be found by solving an appropriate set of linear matrix inequalities. For the system at hand the change of $\hat{\alpha}_1$ within 14 days is typically small, and all the above mentioned criteria will hold.

5.4.7 Simulation results

Results of closed-loop simulations are used to demonstrate the concept. The method and the simulation results are also published in [44].
Model parameters for the simulation results are given in Table 5.3.

Parameter	Value	Parameter	Value
T_s	1 min	A_{ICB}	163.5 m^2
α_0	0.4 $\mathrm{W/m^2K}$	mc_{p}	8.8e+06 $\mathrm{J/K}$
n_{p}	20 samples	γ	0.2
n_{c}	20 samples		

Table 5.3: Model parameters

The value of N_p has been increased from a small value until the further performance increase was insignificant; for the value of $N_p = 20$ a good compromise between performance and computational efficiency was obtained. Selection of N_c was done in a similar way which led to $N_c = N_p$. Smaller values of N_c led to undesirable high control action.

Comparison with conventional control

The MPC controller with observer ($\mathrm{MPC_o}$) is compared to an offset-free augmented MPC without observer ($\mathrm{MPC_c}$), [94]. In order to achieve a compromise between noise attenuation and performance for $\mathrm{MPC_o}$ weighting factors R_1 and R_2 where optimized such that $\vartheta_{\mathrm{ICB,o}}$ in the simulation shown in Fig. 5.12 had minimum variance. The obtained values have been rounded. Note that the plant model is not normalized and therefore large numerical values for R_1 and R_2 result. Furthermore, the choice of one weighting factor is arbitrary, as criterion eq. (5.43) is only affected by the quotient of

R_1 and R_2. To get a fair comparison, the $\mathrm{MPC_c}$ was tuned such that the responses of both controllers have the same dynamics after a step change in ϑ_{amb}. The controller parameters are given in Table 5.4.

	R_1	R_2	P_R	$\boldsymbol{L}$
$\mathrm{MPC_o}$	1000000	1.00e−06	1.24e+07	$\begin{bmatrix} -1.7606 \\ -19.5613 \end{bmatrix}$
$\mathrm{MPC_c}$	100	3.85e−11	1.24e+03	-

Table 5.4: Controller parameters

In the first comparison zero-mean random measurement noise d_{ICB} with increasing variance is added to ϑ_{ICB}. For sake of clarity α is kept constant in this simulation, therefore $\alpha(t) = \alpha = \alpha_0$ and $\dot{Q}_z = \dot{Q}_{\mathrm{sol}}$.
In Table 5.5 the different variances of d_{ICB} and the RMSE, eq. (5.22), between the constant reference temperature and the actual ICB temperature are listed. Only values where solar irradiation $Q_{\mathrm{sol}} > 0$ are used for calculating the RMSE value.

Variance	0.00	0.01	0.02	0.04	0.06	0.08	0.10	0.12
$\mathrm{MPC_o}$	0.033	0.033	0.033	0.034	0.034	0.032	0.041	0.038
$\mathrm{MPC_c}$	0.0002	0.010	0.019	0.037	0.058	0.075	0.092	0.116

Table 5.5: Comparison of the RMSE values for varying variance of d_{ICB}.

In Fig. 5.12 the input, state, output, and disturbance values of both controllers are shown for a simulation with a variance of d_{ICB} with 0.01. Due to the additional observer $\mathrm{MPC_o}$ exhibits a delay in estimating $\hat{\dot{Q}}_z$ (Fig. 5.12, bottom plot). This delayed estimate in turn leads to a small low-pass deviation in the controlled variable $\vartheta_{\mathrm{ICB,o}}$ (Fig. 5.12, middle plot). For small values of d_{ICB} this deviation is larger than the result for $\mathrm{MPC_c}$. Nevertheless, the observer acts as a low-pass filter and the smooth $\vartheta_{\mathrm{ICB,o}}$ is almost invariant to the amplitude of d_{ICB}. The RMSE of $\mathrm{MPC_c}$, however, shows a proportional increase with the variance of d_{ICB}, Fig. 5.13 and Table 5.5.
Note that aside from the performance comparison only $\mathrm{MPC_o}$ is capable to deliver an estimate for $\hat{\dot{Q}}_z$ and consequently for $\dot{Q}_{\mathrm{sol}}$ and α.

α-deterioration

In order to demonstrate the estimation principle of α_1 a nonlinear parametric model of the MF2-100 type, [3], is assumed. With eq. (2.24) the nonlinear parametric model can be described as

$$\alpha(t) = \alpha_0 + \theta_{\alpha,1} t^{\theta_{\alpha,2}} + \theta_{\alpha,3}. \tag{5.48}$$

A simulation over three months with a sudden change in α is performed. Fig. 5.14 shows the time behavior of the input, state, output, and disturbance values, respectively.

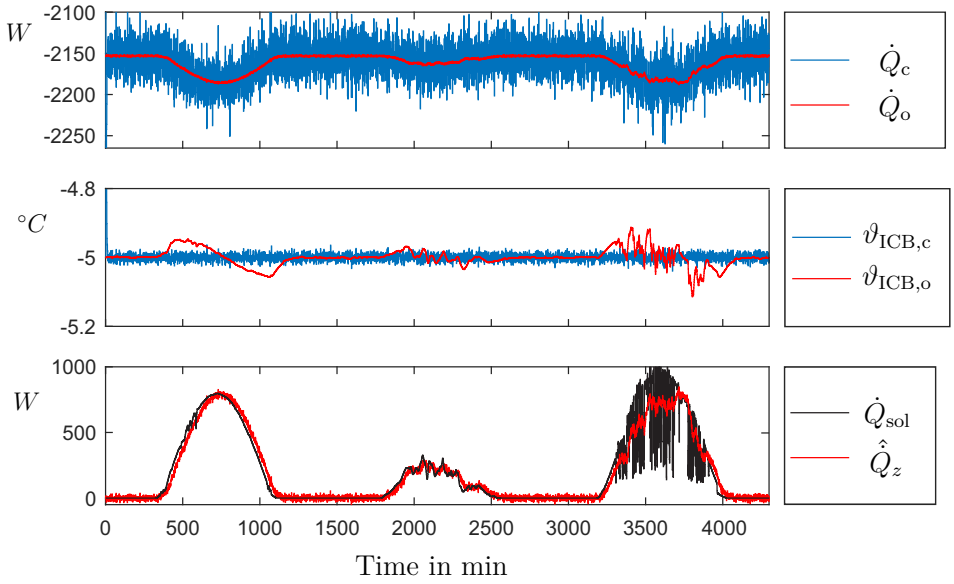

Figure 5.12: Comparison of the MPC controller without observer MPC_c and with observer MPC_o. The variance for d_{ICB} is 0.01.

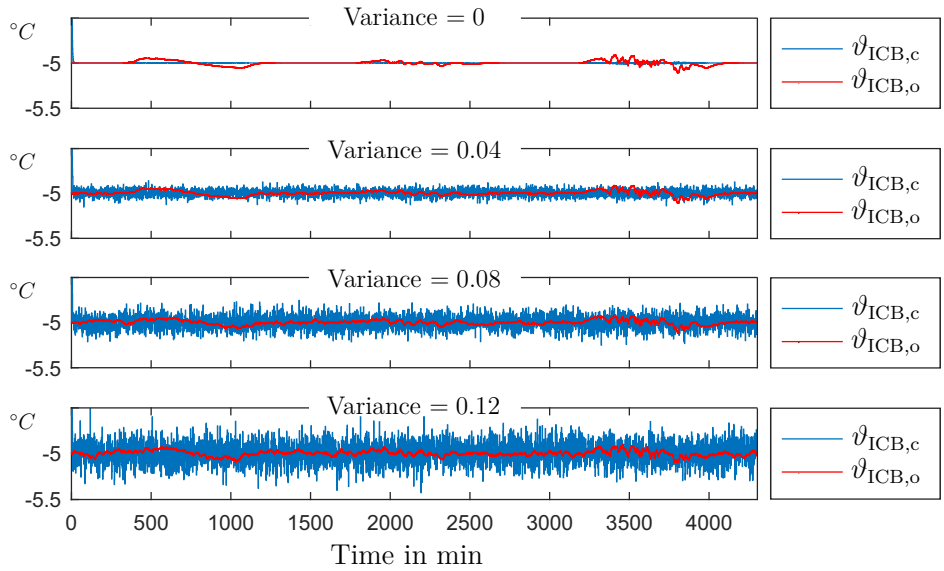

Figure 5.13: Comparison of ϑ_{ICB} of both methods (MPC_c and MPC_o), with increasing noise variances of d_{ICB} in the subplots.

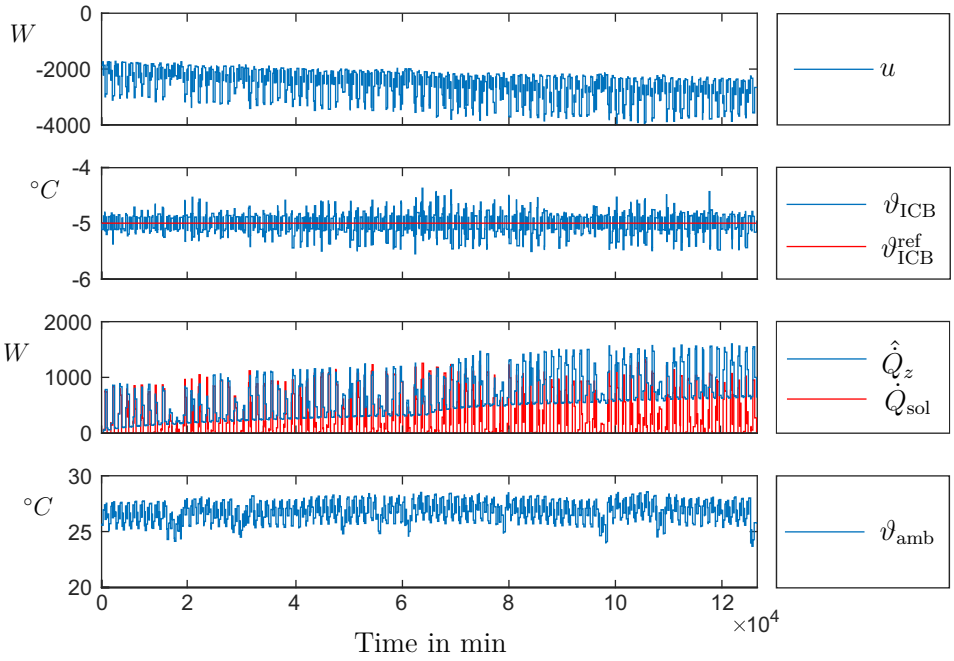

Figure 5.14: Control variable, state, output, and disturbance signals with a sudden change in α after $6.624 \cdot 10^4$ samples.

In Fig. 5.15 the first plot shows the total disturbance and the heat input of α, where $\dot{Q}_{\hat{\alpha}}$ is estimated every 14 days. The measurement noise affects the estimation, nevertheless an acceptable estimation of α_1 can be ensured, see second plot. All estimated predictions are plotted, showing that first estimates already coincide well with later more reliable estimates. It can be seen, that the sudden change in α is detected by the method (solid lines of $\dot{Q}_{\alpha_0} + \dot{Q}_{\hat{\alpha}}$). The dashed lines represent the predicted output of the global model if no detection of change would be included in the estimation.
In Fig. 5.16 the values of J_{glob}, eq. (5.30), and J_{loc}, eq. (5.31) are shown. The first plot shows the values evaluated every 14 days. The second plot shows the values evaluated every day. This finer evaluation can be used to find the correct time instant of the change in α. As both criteria J_{glob} and J_{loc} are proportional to the estimation error covariance, a significant deviation between both values should be evaluated by an F-test.
In Table 5.6 the values of J_{glob}, J_{loc} and the F-test with $t_{\mathrm{hist}} = 14$ days are shown. With a one-sided hypothesis test, where the F-value $= \frac{J_{\mathrm{glob}}}{J_{\mathrm{loc}}}$ has to be smaller than the critical F-value $F_{\mathrm{crit}} = 1.03$ for 14 days, it can be seen that a change of α occurs after day 42 since later F-values are larger than F_{crit}.
To find the correct position of the change in α a finer evaluation, $t_{\mathrm{hist}} = 1$ day in the relevant region is made. For a robust evaluation the F-value has to be more than two times in succession larger than the critical F-value $F_{\mathrm{crit}} = 1.11$ for one day. Therefore

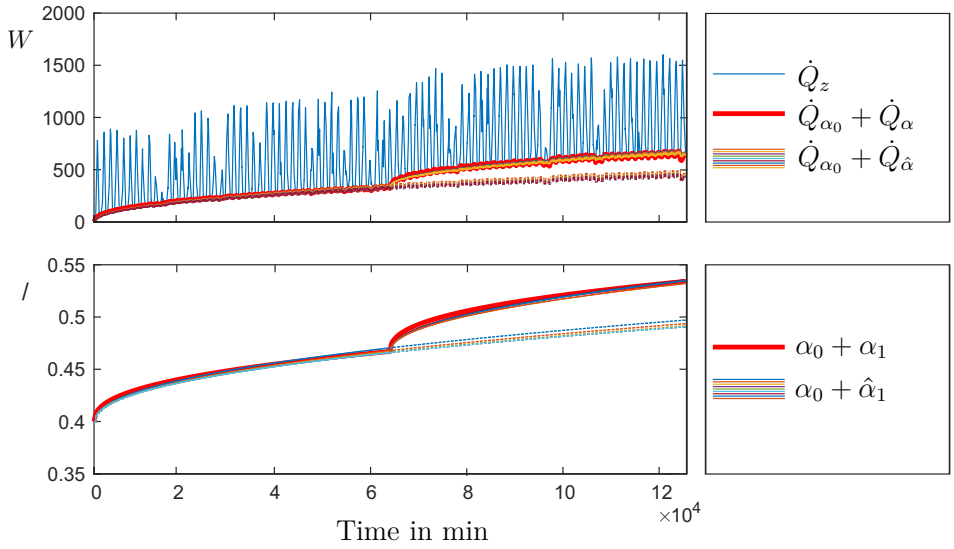

Figure 5.15: First plot: actual $\dot{Q}_{\alpha_0} + \dot{Q}_\alpha$ and all estimated $\dot{Q}_{\alpha_0} + \dot{Q}_{\hat{\alpha}}$, second plot: $\alpha_0 + \alpha_1$ and all estimated $\alpha_0 + \hat{\alpha}_1$, dashed lines: predicted output of the model before the change in α_1 occurs.

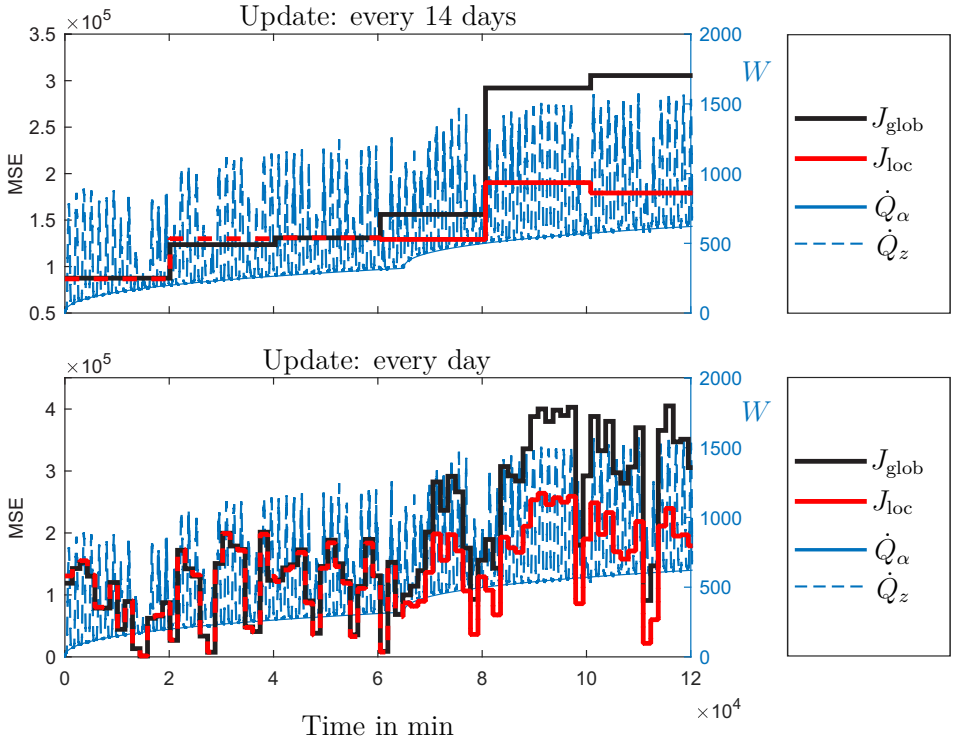

Figure 5.16: Comparison of J_{glob} and J_{loc}. After the change in α occurs the performance of the global model deteriorates, and the local model must be considered valid.

days after t_0	$J_{\text{glob}} \cdot 10^5$	$J_{\text{loc}} \cdot 10^5$	F-value
14	0.87	0.87	1.01
28	1.24	1.30	0.95
42	1.31	1.31	1.00
56	1.56	1.29	$1.21^\star$
70	2.92	1.90	$1.54^\star$
84	3.06	1.79	$1.71^\star$

Table 5.6: The MSE values of the global and local model and furthermore the F-value evaluated every 14 days. Values denoted by $\bullet^\star$ indicate $F > F_{\text{crit}}$.

the correct position can be found which in this simulation is at day 46 (sample 66240), see Table 5.7. Note that at day 43 a singular exceedance of the critical F-value occurs.

days after t_0	$J_{\text{glob}} \cdot 10^5$	$J_{\text{loc}} \cdot 10^5$	F-value
42	1.31	1.31	1.00
43	0.09	0.08	$1.15^\star$
44	1.53	1.51	1.01
45	0.68	0.65	1.06
46	1.00	0.87	$1.15^\star$
47	1.14	0.82	$1.39^\star$
48	1.39	0.90	$1.55^\star$
49	2.01	1.36	$1.48^\star$

Table 5.7: The MSE values of the global and local model and furthermore the F-value evaluated every day. Values denoted by $\bullet^\star$ indicate $F > F_{\text{crit}}$.

Assessment of prediction uncertainty

As presented in Section 5.4.2 the uncertainty in the α model also affects the prediction of the end-of-life. Due to the nonlinear model and optimization the probability density function (PDF) of the estimated parameter t_{crit} cannot be computed analytically. Moreover, the type of PDF is unknown and is in general not normal. In order to assess this phenomenon a Monte Carlo simulation is performed to obtain a non-parametric estimate of the resulting PDF.
The simulation assumes that three months after a abrupt change in the aging model parameters the end-of-life (t_{crit}) is predicted. All data stay the same throughout the simulations, only a new and uncorrelated sequence of zero-mean measurement noise with a standard deviation of 0.04 is used in each run. The whole simulation consists of 1000 runs.

In Fig. 5.17 the actual deterioration of α is shown in red and the envelope of all estimated $\hat{\alpha}_1$ of the Monte Carlo simulation is plotted in blue. The value α_{now} denotes the actual value at t_{now} and the corresponding PDF of the α estimate is approximated by the histogram plotted below.
The PDF for the prediction of t_{crit} for reaching the critical value α_{crit} not only exhibits a larger variance but also has a different shape (see top of Fig. 5.17). Note that the PDF for the α estimate at t_{crit} also has a larger variance and an altered shape compared to the current estimate α_{now}. A confidence interval for all the estimates can be obtained from respective 5% and 95% percentiles. In the simulation at hand the median (50% percentile) is obviously a good estimator for the real values of t_{crit} and α_{crit} (plotted as red bars in the histograms).
A Kolmogorov-Smirnov test for normality of the PDFs for t_{crit} and α_{crit} results in highly significant p-values of $4.2 \cdot 10^{-50}$ and $1.82 \cdot 10^{-67}$, respectively, which clearly rejects the normality hypothesis.

5.5 Comparison of both concepts

In Table 5.8 the differences between the two proposed concepts are shown:

	Concept 1: Disturbance compensation with Luenberger observer	Concept 2: Full state observer with nonlinear estimation
Observer	standard Luenberger	current observer
Observer output	$\hat{\dot{Q}}_z$	$\hat{\dot{Q}}_z$, $\hat{\vartheta}_{\text{ICB}}$
$\hat{\dot{Q}}_z$ prediction	none	zero order prediction
estimation model	linear	nonlinear
estimation	24h minima	nonlinear curve fitting
MPC	augmented	offset-free
MPC additional state	integrator	disturbance
Sampling rate	$K \neq k$	$K = k$
noise	none	d_{amb}, d_{ICB}

Table 5.8: Differences of the two concepts: Disturbance compensation with Luenberger observer and full state observer with nonlinear estimation.

In both concepts the observer operates with a fast sampling rate. In the first concept a standard Luenberger observer is used to estimate the unknown disturbance. Because of the structure of the observer a delay of one sample happens. To avoid this in the second concept a current observer which uses the most recent measurements is used. In the first concept the estimated disturbance is directly added to the necessary cooling capacity for the RS. In the second concept the observer estimates the disturbance and

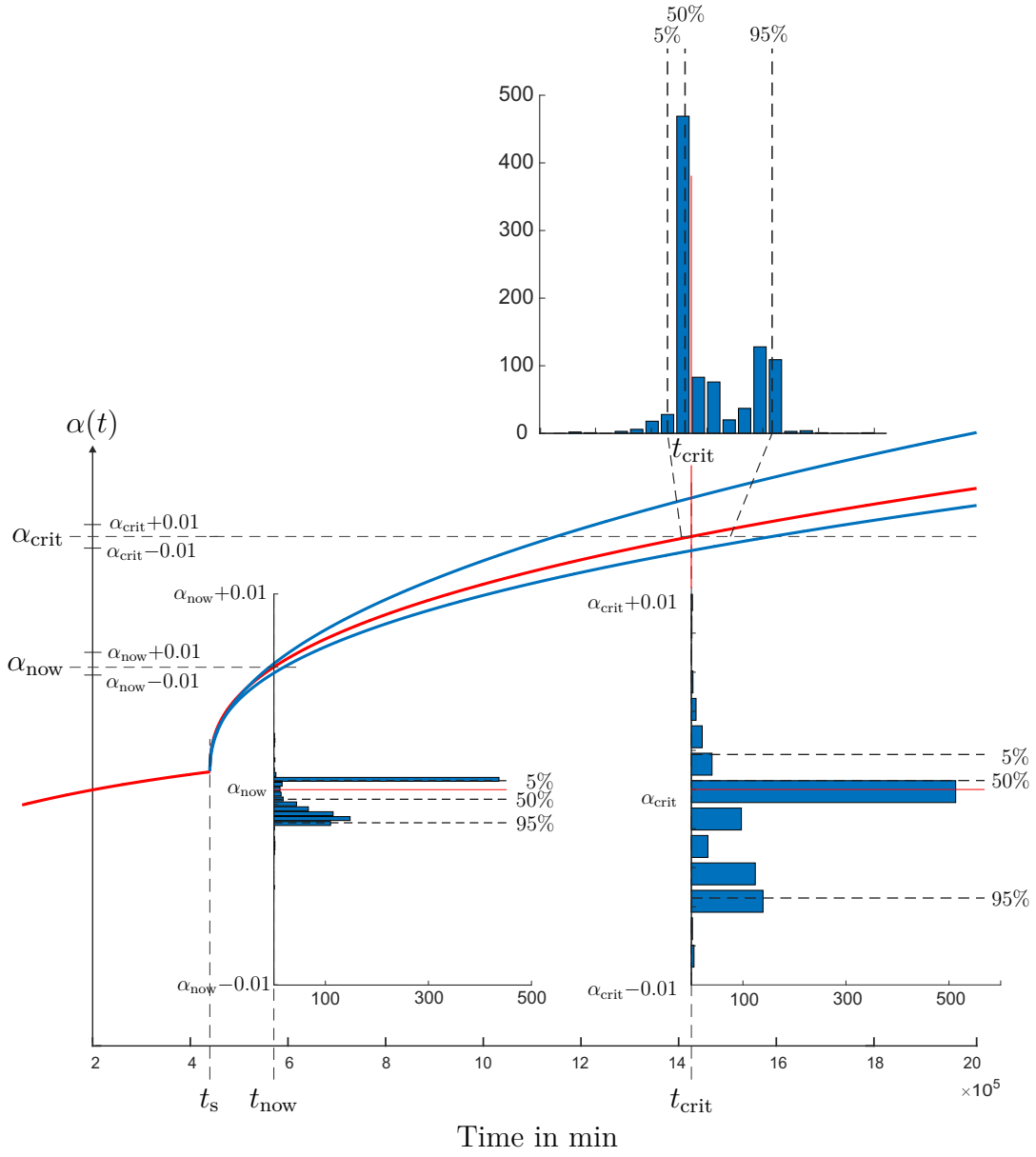

Figure 5.17: Critical time t_{crit} estimate based on data from t_s to t_{now}. Histograms of the α estimates at times t_{now} and t_{crit} as well as the histogram for t_{crit} are plotted enlarged. All histograms contain 5%, 50%, and 95% percentiles (black dashed lines) and the actual values (red solid line).

the ICB temperature. With the estimated disturbance a prediction of the disturbance over the whole MPC horizon is calculated. The predicted disturbance and predicted ICB temperature are used in the MPC to optimize the necessary cooling capacity. For a simple implementation the first concept uses a linear estimation model for the heat transfer coefficient. The minima over 24 hours are used to fit the linear model. Whereas in the second concept a parametric nonlinear model with a nonlinear curve fitting is used. The first concept includes an augmented MPC with a slow sampling rate. The augmented state is a integrator which ensures offset-free control. However, the sampling rate of the observer is faster and therefore reacts before the integrator of the MPC can compensate the disturbance. In the second concept an offset-free MPC with the disturbance as augmented state is implemented. The sampling rate of the MPC is the fast sampling rate. The augmented state can directly be used for a physical interpretation of the disturbance. For robustness of the observer measurement noise is added to the ambient temperature and ICB temperature in the second concept, which can also be easily included in the first concept.

5.6 Summary

The proposed control scheme consists of an model predictive controller, an disturbance observer for unknown heat inputs $\hat{\dot{Q}}_z$ and the estimation of the heat transfer coefficient α which is an indicator for the state of health of the ICB. This structure enables the immediate compensation of solar irradiance as it reacts fast to disturbances. With the hypotheses that α_1 deteriorates slowly over time, a drift in the disturbance estimate provides useful information about the deterioration grade of α. The correct α is an important factor for assessing the state of health of the ICB, and it also ensures a correct model of the MPC which leads to better performance than a predictive control method without α estimation. Simulation results show that both concepts are able to estimate α and $\dot{Q}_{\mathrm{sol}}$.

The concept to use minimal values of the estimated $\hat{\dot{Q}}_z$ calls for additional measures to ensure robustness such as hypothesis tests with the prediction interval or constrained optimization. In the second concept also predictive maintenance and a detailed stability proof is given.

Chapter 6

Discussion and conclusion

6.1 Scientific contributions

The following scientific contributions have been made in the thesis to answer the questions posed in Section 1.4:

1. Computation of an appropriate control allocation of the RS is realized by three different methods. The first method is realized by separating the whole problem formulation in smaller subproblems where the computationally expensive optimization of the continuous decision variables is optimized off-line and stored in look-up tables. The numerically efficient subproblem is optimized on-line. The concept is presented in Chapter 3 and published in [42]. The second method uses a computationally expensive mixed-integer MPC (MI-MPC), which is executed every small sampling time. The third method uses a mixed-integer optimization (MIO), which is only executed once in a large sampling step. Both methods are presented in Chapter 4.

2. Temperature control of the ICB is provided by model predictive control and presented in Chapter 4. An augmented MPC formulation is used for optimal control of the ICB temperature. Constraints are used to ensure that the RCs work in a feasible range. The MPC also defines constraints for the CA. Two methods with different constraint formulations are derived. In the first method the constraint is the necessary cooling capacity, whereas the second method uses the predicted ICB temperature as a constraint. The first concept including the MI-MPC is already published in [45], whereas the second method including the MIO is submitted for a special edition in the Journal of Process Control.

3. Disturbance and parameter estimation is done in two different ways. A simple to implement method has been developed using a disturbance observer which calculates an additional heat impact to the ICB with a linear parameter estimation for the state-of-health of the ICB. An extended MPC formulation with integrated disturbance state and a parametric nonlinear estimation is done in the second

method. Both methods are presented in Chapter 5. The first concept is published in [43], the second concept is published in [44].

6.2 Discussion

In order to speed up the optimization of Chapter 4 the optimal solutions for every initial condition, set-point, and boundary condition could also be calculated off-line and stored in look-up tables, see Chapter 3. In this case the MI-MPC would be implemented as a static feed-forward switching control similar to a pulse width modulator but exhibiting much more complex switching patterns. A disadvantage of this structure is that the dimension of the look-up tables expands exponentially with the number of switching variables and the prediction horizon. The prediction horizon of such a simplified version of the MI-MPC could additionally be cut to one sample of the global MPC. Using this modification no update during the prediction horizon has to be made, and consequently a static feed-forward modulator results. Still, the memory requirements would be large and optimal switching over the large samples would be lost.

A cascade control structure could also be used. It can potentially improve the closed loop disturbance compensation performance for all disturbances acting directly on the RS. The cascade control system consists of the primary control loop with the global MPC and nested within the primary control loop is the secondary control loop with the CA and the RS. The secondary control loop reduces the effect of a fault on the RS, like wear of the compressor or fouling of the condenser which affects the actual u. The CA can react before the global MPC is influenced by the faulty. The main drawback is the need for measuring u. Measuring u directly is not possible, indirect measurement using air flow (or a pressure difference) and temperature is expensive and sensitive to faults. Also an analytical stability proof is not possible using the approach in this thesis. If the cascade control is not implemented faults on the RS are compensated by the global MPC.

The presented method in Chapter 5.4 enables offset-free tracking by estimating the unknown disturbance $\dot{Q}_z$. A similar nominal performance can be obtained by an augmented MPC, see Section 5.4.7. However, the additional tuning parameters in the matrix $\boldsymbol{L}$ of the observer enable better tuning in the presence of measurement noise. In principle it would also be possible to apply a Kalman-filter with two additional states (irradiation and α) as a disturbance observer. By tuning the respective entries of the process noise covariance matrix one could hope for a proper estimation result. However, no satisfying results were obtained with such a Kalman-filter, as both a state and a parameter have to be observed simultaneously which renders the observer nonlinear and a nonlinear estimation scheme would become necessary.

Another important issue is the true heat capacity mc_p of the ICB: The exact value is typically not known, nevertheless, the current weight of the load m can be read from

the vehicle data bus, and depending on the freight composition an average value of the specific heat c_p can be used for computing mc_p. Note that a parameter identification of mc_p would be ill conditioned as the measured temperature ϑ_ICB of the ICB is almost constant and the value of mc_p does not affect steady-state behavior. Thus, any estimation algorithm will suffer from the absence of a persistently excited output signal.

Due to aging the parameter $\hat{\alpha}_1$ (describing thermal conductivity of the ICB) is monotonically increasing, and the system matrices defined in Sections 5.4.4 and 5.4.5 are therefore actually also time-varying (updated every 14 days). As stated in Section 5.4.6 stability of the system can nonetheless be guaranteed. Simulation studies have shown that the proposed system is fairly robust with respect to these changes in the system matrices. It could therefore be possible to implement constant matrices as a simplification in a specific application. In a first step the observer and the α estimation will be implemented on the controller hardware; as the MPC requires more computing power it can only be implemented after a hardware upgrade of current RS-controllers.

Possible problems concerning the stability of the nonlinear α estimate can arise from different sources: 1) A suitable model structure, eq. (2.24), is paramount for an effective estimate. Selecting a good model structure will depend on the ICB materials, the operating scheme, the environmental conditions and other factors. Sufficient measurement data are necessary to validate the model structure. 2) Even if the model structure is perfect, the parameters of the model could be continuously time-varying. In this case the F-test, see Section 5.4.7, would indicate step-wise changes of the model parameters which is just a rough approximation of the true parameters. 3) In the unlikely case that the system is only operated around noon, the nonlinear estimate would be biased as no night time measurements would be available.

6.3 Conclusion

The refrigeration systems (RSs) of food transporters which are widely used in the world consume a substantial amount of energy. A robust and effective control of the temperature inside an insulated cool box (ICB) is necessary to prevent degeneration of perishable goods. In order to obtain low maintenance and energy costs and to maximize the availability of the system, ICBs can be equipped with redundant refrigeration circuits (RC) each utilizing one or more compressors. These systems include a multitude of both switched (compressor on/off state) and continuous (expansion valve, fan speed) control variables, calling for a mixed-integer optimization (MIO). Therefore, in this thesis, an ICB with redundant refrigeration circuits (RCs) each with various compressors was proposed.

First a method to optimize the provision of the required cooling capacity in redundant RCs with respect to several conflicting goals is introduced. The proposed method is

presented for a refrigeration system with redundant refrigeration circuits and multiple compressors. Both discrete (compressor switching) and continuous (variable speed drives, valve settings) decision variables are integrated in the optimization. Each mode is characterized by the respective active components and the values of the individual continuous control variables. The resulting degrees of freedom can be utilized to optimize additional goals such as energy consumption, wear, etc. The optimal process operation is thus formulated as a optimization problem for a hybrid system. The framework is very general, comprising different numbers of RCs and compressors respectively, accepting compressors with both identical or different capacity within one RC, and even incorporating the strongly nonlinear nature of an internal combustion engine as a primary energy source for the RCs can be considered. An important highlight of the proposed method is the computational efficiency, which allows the implementation in an inexpensive micro-controller.

Second model predictive control (MPC) was introduced. Due to the different time constants and complex mixed-integer optimization a hierarchical control structure is used. Because of the slow dynamics of the ICB the global MPC can operate at a large sampling time with a large prediction horizon. The computational expensive underlying control allocation (CA) provides a multi-objective optimization which defines the actual control action and is operating at a high sampling frequency and a small prediction horizon (only the first few samples of the linear MPC). Main contributions of this work are the formulation of a specific equality constraint for the MIO in the second concept and the overall stability of the control scheme. It was shown, that especially for setpoints where the required stationary cooling capacity is smaller than the minimum one a limit cycle results.

Third, a method for model predictive temperature control with estimation of aging of the ICB's insulation and heat transfer due to the sun's irradiation has been proposed. The estimation is performed by a custom disturbance observer which first estimates the combined heat loss of both effects and a nonlinear parameter estimation of a suitable aging model. The observer together with a suitable MPC formulation guarantees offset-free tracking of the set-temperature, effective compensation of irradiation, good noise attenuation properties, and also predictive maintenance of the ICB. The last feature is achieved by using the aging model as a predictor for estimating the end-of-life for the ICB. In order to detect and react to sudden changes in the ICB's operating state, a detection of changes and a parameter update has also been proposed. Furthermore, each subsystem (observer, MPC, α-estimation) runs at a specific sampling time to facilitate effective operation.

Bibliography

[1] Alhelou, H. H., Golshan, M. H., and Askari-Marnani, J. (2018). Robust sensor fault detection and isolation scheme for interconnected smart power systems in presence of RER and EVs using unknown input observer. *International Journal of Electrical Power & Energy Systems*, 99:682–694.

[2] Arguello-Serrano, B. and Velez-Reyes, M. (1995). Design of a nonlinear HVAC control system with thermal load estimation. In *Control Applications, 1995., Proceedings of the 4th IEEE Conference on*, pages 33–39. IEEE.

[3] Baetens, R., Jelle, B. P., Thue, J. V., Tenpierik, M. J., Grynning, S., Uvsløkk, S., and Gustavsen, A. (2010). Vacuum insulation panels for building applications: A review and beyond. *Energy and Buildings*, 42(2):147–172.

[4] Barcelliy, D., Bemporadz, A., and Ripaccioliy, G. (2010). Hierarchical multi-rate control design for constrained linear systems. In *49th IEEE Conference on Decision and Control (CDC)*, pages 5216–5221. IEEE.

[5] Bejarano, G., Alfaya, J. A., Ortega, M. G., and Vargas, M. (2017a). On the difficulty of globally optimally controlling refrigeration systems. *Applied Thermal Engineering*, 111:1143–1157.

[6] Bejarano, G., Vivas, C., Ortega, M. G., and Vargas, M. (2017b). Suboptimal hierarchical control strategy to improve energy efficiency of vapour-compression refrigeration systems. *Applied Thermal Engineering*, 125:165–184.

[7] Bemporad, A. and Morari, M. (1999). Control of systems integrating logic, dynamics, and constraints. *Automatica*, 35(3):407–427.

[8] Bendapudi, S., Braun, J. E., and Groll, E. A. (2008). A comparison of moving-boundary and finite-volume formulations for transients in centrifugal chillers. *International Journal of Refrigeration*, 31(8):1437–1452.

[9] Bertsekas, D. P. (2014). *Constrained optimization and Lagrange multiplier methods*. Academic press.

[10] Camacho, E. F. and Alba, C. B. (2013). *Model predictive control*. Springer Science & Business Media.

[11] Camacho, E. F., Ramírez, D. R., Limón, D., De La Peña, D. M., and Alamo, T. (2010). Model predictive control techniques for hybrid systems. *Annual reviews in control*, 34(1):21–31.

[12] Chen, J., Patton, R. J., and Zhang, H.-Y. (1996). Design of unknown input observers and robust fault detection filters. *International Journal of control*, 63(1):85–105.

[13] Choudhary, M., Karki, K., and Patankar, S. (2004). Mathematical modeling of heat transfer, condensation, and capillary flow in porous insulation on a cold pipe. *International Journal of Heat and Mass Transfer*, 47(26):5629–5638.

[14] Deng, H., Larsen, L., Stoustrup, J., and Rasmussen, H. (2009). Control of systems with costs related to switching: applications to air-condition systems. In *Control Applications,(CCA) & Intelligent Control,(ISIC), 2009 IEEE*, pages 554–559. IEEE.

[15] Dong, W., Kun, L., and Yi, W. (2017). Model predictive control of a large temperature difference refrigerating station with ice cold thermal energy storage. In *Chinese Automation Congress (CAC), 2017*, pages 7340–7345. IEEE.

[16] Dullinger, C., Struckl, W., and Kozek, M. (2018). A general approach for mixed-integer predictive control of HVAC systems using MILP. *Applied Thermal Engineering*, 128:1646–1659.

[17] Ekren, O., Sahin, S., and Isler, Y. (2010). Comparison of different controllers for variable speed compressor and electronic expansion valve. *International Journal of Refrigeration*, 33(6):1161–1168.

[18] Ertunc, H. M. and Hosoz, M. (2006). Artificial neural network analysis of a refrigeration system with an evaporative condenser. *Applied Thermal Engineering*, 26(5-6):627–635.

[19] Gurobi (2017). Gurobi optimizer. `http://www.gurobi.com`. Accessed: 27-09-2017.

[20] Hamid, N. H. A., Kamal, M. M., and Yahaya, F. H. (2009). Application of PID controller in controlling refrigerator temperature. In *Signal Processing & Its Applications, 2009. CSPA 2009. 5th International Colloquium on*, pages 378–384. IEEE.

[21] Hamilton, F. C., Colaço, M. J., Carvalho, R. N., and Leiroz, A. J. (2014). Heat transfer coefficient estimation of an internal combustion engine using particle filters. *Inverse Problems in Science and Engineering*, 22(3):483–506.

[22] Handbook, A. F. (2009). American society of heating, refrigerating and air-conditioning engineers. *Inc.: Atlanta, GA, USA*.

[23] He, H., Jia, H., Sun, C., and Sun, F. (2018). Stochastic model predictive control of air conditioning system for electric vehicles: Sensitivity study, comparison and improvement. *IEEE Transactions on Industrial Informatics*.

[24] Hofstädter, R. N., Zero, T., Dullinger, C., Richter, G., and Kozek, M. (2017). Heat capacity and heat transfer coefficient estimation for a dynamic thermal model of rail vehicles. *Mathematical and Computer Modelling of Dynamical Systems*, 23(5):439–452.

[25] Huang, K.-Y., Yang, H.-T., and Huang, C.-L. (1997). A new thermal unit commitment approach using constraint logic programming. In *Power Industry Computer Applications., 1997. 20th International Conference on*, pages 176–185. IEEE.

[26] Huang, Y., Khajepour, A., Bagheri, F., and Bahrami, M. (2016). Optimal energy-efficient predictive controllers in automotive air-conditioning/refrigeration systems. *Applied energy*, 184:605–618.

[27] Jain, N. (2013). *Thermodynamics-based optimization and control of integrated energy systems*. PhD thesis, University of Illinois at Urbana-Champaign.

[28] James, S., James, C., and Evans, J. (2006). Modelling of food transportation systems – a review. *International Journal of Refrigeration*, 29(6):947 – 957.

[29] Jelle, B. P. (2011). Traditional, state-of-the-art and future thermal building insulation materials and solutions-properties, requirements and possibilities. *Energy and Buildings*, 43(10):2549–2563.

[30] Jian, W.-L. and Zaheeruddin, M. (1998). Sub-optimal on-off switching control strategies for chilled water cooling systems with storage. *Applied Thermal Engineering*, 18(6):369–386.

[31] Kitanoski, F. and Hofer, A. (2010). Energy optimal control of a cooling system-limits of performance. In *Proceedings of the International Conference on Modelling, Identification and Control (MIC 2010)*, pages 116–121.

[32] Larsen, L. F., Geyer, T., and Morari, M. (2005). Hybrid model predictive control in supermarket refrigeration systems. In *IFAC world congress*, volume 16, pages 313–318. Citeseer.

[33] Lee, J.-W., Kwon, W. H., and Choi, J. (1997). On stability of constrained receding horizon control with finite terminal weighting matrix. In *Control Conference (ECC), 1997 European*, pages 313–318. IEEE.

[34] Li, B., Otten, R., Chandan, V., Mohs, W. F., Berge, J., and Alleyne, A. G. (2010). Optimal on-off control of refrigerated transport systems. *Control Engineering Practice*, 18(12):1406–1417.

[35] Li, H., Jeong, S.-K., and You, S.-S. (2009). Feedforward control of capacity and superheat for a variable speed refrigeration system. *Applied Thermal Engineering*, 29(5):1067–1074.

[36] Liang, N., Shao, S., Tian, C., and Yan, Y. (2010). Dynamic simulation of variable capacity refrigeration systems under abnormal conditions. *Applied Thermal Engineering*, 30(10):1205–1214.

[37] Lin, H. and Antsaklis, P. J. (2009). Stability and stabilizability of switched linear systems: a survey of recent results. *IEEE Transactions on Automatic control*, 54(2):308–322.

[38] Liu, J., Wang, L., Jia, L., Li, Z., and Zhao, H. (2017). A control oriental model for combined compression-ejector refrigeration system. *Energy Conversion and Management*, 138:538–546.

[39] Liu, X., Paritosh, P., Awalgaonkar, N. M., Bilionis, I., and Karava, P. (2018). Model predictive control under forecast uncertainty for optimal operation of buildings with integrated solar systems. *Solar Energy*, 171:953–970.

[40] Lofberg, J. (2004). YALMIP: A toolbox for modeling and optimization in MATLAB. In *Computer Aided Control Systems Design, 2004 IEEE International Symposium on*, pages 284–289. IEEE.

[41] Long, Y., Liu, S., Xie, L., and Johansson, K. (2016). A hierarchical distributed MPC for HVAC systems. In *American Control Conference (ACC), 2016*, pages 2385–2390. American Automatic Control Council (AACC).

[42] Luchini, E., Kitanoski, F., and Kozek, M. (2017a). Multi-objective optimization of the operational modes for redundant refrigeration circuits. *Applied Thermal Engineering*, 122:409–419.

[43] Luchini, E. and Kozek, M. (2018). Disturbance observer and ageing estimation for a temperature controlled food transporter. In *Control Systems (SICE ISCS), 2018 SICE International Symposium on*. IEEE.

[44] Luchini, E., Radler, D., Ritzberger, D., Jakubek, S., and Kozek, M. (2018). Model predictive temperature control and ageing estimation for an insulated cool box. *Applied Thermal Engineering*.

[45] Luchini, E., Schirrer, A., and Kozek, M. (2017b). A hierarchical MPC for multi-objective mixed-integer optimisation applied to redundant refrigeration circuits. *IFAC-PapersOnLine*, 50:9058–9064.

[46] Luenberger, D. (1971). An introduction to observers. *IEEE Transactions on automatic control*, 16(6):596–602.

[47] Maeder, U., Borrelli, F., and Morari, M. (2009). Linear offset-free model predictive control. *Automatica*, 45(10):2214–2222.

[48] Marruedo, D. L., Alamo, T., and Camacho, E. (2002). Stability analysis of systems with bounded additive uncertainties based on invariant sets: Stability and feasibility of MPC. In *Proceedings of the 2002 American Control Conference (IEEE Cat. No. CH37301)*, volume 1, pages 364–369. IEEE.

[49] Mayer, B., Killian, M., and Kozek, M. (2014). Cooperative and hierarchical fuzzy MPC for building heating control. In *2014 IEEE International Conference on Fuzzy Systems (FUZZY-IEEE)*, pages 1054–1059. IEEE.

[50] Mayer, B., Killian, M., and Kozek, M. (2016). A branch and bound approach for building cooling supply control with hybrid model predictive control. *Energy and Buildings*, 128:553–566.

[51] Mayne, D. Q., Rawlings, J. B., Rao, C. V., and Scokaert, P. O. (2000). Constrained model predictive control: Stability and optimality. *Automatica*, 36(6):789–814.

[52] Mei, J., Xia, X., and Song, M. (2018). An autonomous hierarchical control for improving indoor comfort and energy efficiency of a direct expansion air conditioning system. *Applied Energy*, 221:450–463.

[53] Mei, J., Zhu, B., and Xia, X. (2015). Predictive control for thermal comfort and energy efficiency in a direct expansion air conditioning system. In *Chinese Automation Congress (CAC), 2015*, pages 264–269. IEEE.

[54] Mendes, P. R., Maestre, J. M., Bordons, C., and Normey-Rico, J. E. (2017). A practical approach for hybrid distributed MPC. *Journal of Process Control*, 55:30–41.

[55] Mignone, D., Ferrari-Trecate, G., and Morari, M. (2000). Stability and stabilization of piecewise affine and hybrid systems: An LMI approach. In *Decision and Control, 2000. Proceedings of the 39th IEEE Conference on*, volume 1, pages 504–509. IEEE.

[56] Moroşan, P.-D., Bourdais, R., Dumur, D., and Buisson, J. (2011). A distributed MPC strategy based on benders' decomposition applied to multi-source multi-zone temperature regulation. *Journal of Process Control*, 21(5):729–737.

[57] Na, J., Chen, A. S., Herrmann, G., Burke, R., and Brace, C. (2018). Vehicle engine torque estimation via unknown input observer and adaptive parameter estimation. *IEEE Transactions on Vehicular Technology*, 67(1):409–422.

[58] Naeem, O. and Huesman, A. E. (2014). Multivariate hammerstein structures: A qualitative accuracy comparison to new input-state block structure. In *Computer Aided Chemical Engineering*, volume 33, pages 1771–1776. Elsevier.

[59] NASA (2017). Aeronet solar radiation network. `https://solrad-net.gsfc.nasa.gov`. Accessed: 07-11-2017.

[60] Nasution, H. and Hassan, M. N. W. (2006). Potential electricity savings by variable speed control of compressor for air conditioning systems. *Clean Technologies and Environmental Policy*, 8(2):105–111.

[61] O'Dwyer, E., Cychowski, M., Kouramas, K., and Lightbody, G. (2013). A hierarchical model-based predictive control strategy for building heating systems. In *Irish Signals & Systems Conference 2014 and 2014 China-Ireland International Conference on Information and Communications Technologies (ISSC 2014/CIICT 2014). 25th IET*, pages 298–303. IET.

[62] O'Neill, Z., Narayanan, S., and Brahme, R. (2010). Model-based thermal load estimation in buildings. *IBPSA-USA Journal*, 4(1):474–481.

[63] Oppenheim, A. V. and Schafer, R. W. (2010). *Discrete-time signal processing*. Pearson Higher Education.

[64] Overman, J. and Calton, D. (1983). Multiple compressor refrigeration system and controller thereof.

[65] Pedersen, R., Schwensen, J., Biegel, B., Green, T., and Stoustrup, J. (2017a). Improving demand response potential of a supermarket refrigeration system: A food temperature estimation approach. *IEEE Transactions on Control Systems Technology*, 25(3):855–863.

[66] Pedersen, T. S., Nielsen, K. M., Hindsborg, J., Reichwald, P., Vinther, K., and Izadi-Zamanabadi, R. (2017b). Predictive functional control of superheat in a refrigeration system using a neural network model. *IFAC-PapersOnLine*, 50(1):43–48.

[67] Pfafferott, T. and Schmitz, G. (2004). Modelling and transient simulation of CO2-refrigeration systems with modelica. *International Journal of Refrigeration*, 27(1):42–52.

[68] Phillips, C. L., Nagle, H. T., and Chakrabortty, A. (2015). *Digital Control System Analysis & Design*. Pearson Prentice Hall.

[69] Picasso, B., Zhang, X., and Scattolini, R. (2016). Hierarchical model predictive control of independent systems with joint constraints. *Automatica*, 74:99–106.

[70] Qureshi, T. and Tassou, S. (1996). Variable-speed capacity control in refrigeration systems. *Applied Thermal Engineering*, 16(2):103–113.

[71] Radecki, P. and Hencey, B. (2012). Online building thermal parameter estimation via unscented kalman filtering. In *American Control Conference (ACC), 2012*, pages 3056–3062. IEEE.

[72] Rajan, C. C. A. and Mohan, M. (2004). An evolutionary programming-based tabu search method for solving the unit commitment problem. *IEEE Transactions on Power Systems*, 19(1):577–585.

[73] Rasmussen, B. P. Dynamic modeling for vapor compression systems—part I: Literature review. *HVAC&R Research*, 18(5):934–955.

[74] Rasmussen, B. P. and Shenoy, B. (2012). Dynamic modeling for vapor compression systems—part II: Simulation tutorial. *HVAC&R Research*, 18(5):956–973.

[75] Rawlings, J. and Mayne, D. (2009). *Model Predictive Control: Theory and Design*. Nob Hill Pub., Llc.

[76] Ríos, H. and Teel, A. R. (2018). A hybrid fixed-time observer for state estimation of linear systems. *Automatica*, 87:103–112.

[77] Romero, J., Navarro-Esbrí, J., and Belman-Flores, J. (2011). A simplified black-box model oriented to chilled water temperature control in a variable speed vapour compression system. *Applied Thermal Engineering*, 31(2-3):329–335.

[78] Roque, L. A., Fontes, D. B., and Fontes, F. A. (2011). A biased random key genetic algorithm approach for unit commitment problem. In *International Symposium on Experimental Algorithms*, pages 327–339. Springer.

[79] Roque, L. A., Fontes, D. B., and Fontes, F. A. (2014). A hybrid biased random key genetic algorithm approach for the unit commitment problem. *Journal of Combinatorial Optimization*, 28(1):140–166.

[80] Scattolini, R. (2009). Architectures for distributed and hierarchical model predictive control-a review. *Journal of process control*, 19(5):723–731.

[81] Scattolini, R. and Colaneri, P. (2007). Hierarchical model predictive control. In *Decision and Control, 2007 46th IEEE Conference on*, pages 4803–4808. IEEE.

[82] Schurt, L. C., Hermes, C. J., and Neto, A. T. (2010). Assessment of the controlling envelope of a model-based multivariable controller for vapor compression refrigeration systems. *Applied Thermal Engineering*, 30(13):1538–1546.

[83] Senjyu, T., Shimabukuro, K., Uezato, K., and Funabashi, T. (2003). A fast technique for unit commitment problem by extended priority list. *Power Systems, IEEE Transactions on*, 18(2):882–888.

[84] Serale, G., Fiorentini, M., Capozzoli, A., Bernardini, D., and Bemporad, A. (2018). Model predictive control (MPC) for enhancing building and HVAC system energy efficiency: Problem formulation, applications and opportunities. *Energies*, 11(3):631.

[85] Shafiei, S. E. and Alleyne, A. (2015). Model predictive control of hybrid thermal energy systems in transport refrigeration. *Applied Thermal Engineering*, 82:264–280.

[86] Simopoulos, D. N., Kavatza, S. D., and Vournas, C. D. (2006). Unit commitment by an enhanced simulated annealing algorithm. *IEEE Transactions on Power Systems*, 21(1):68–76.

[87] Slupphaug, O., Vada, J., and Foss, B. A. (1997). MPC in systems with continuous and discrete control inputs. In *American Control Conference, 1997. Proceedings of the 1997*, volume 5, pages 3495–3499. IEEE.

[88] Snyder, W. L., Powell, H. D., and Rayburn, J. C. (1987). Dynamic programming approach to unit commitment. *IEEE Transactions on Power Systems*, 2(2):339–348.

[89] Sonntag, C., Devanathan, A., Engell, S., and Stursberg, O. (2007). Hybrid nonlinear model-predictive control of a supermarket refrigeration system. In *Control Applications, 2007. CCA 2007. IEEE International Conference on*, pages 1432–1437. IEEE.

[90] Tahersima, F., Stoustrup, J., and Rasmussen, H. (2011). Optimal power consumption in a central heating system with geothermal heat pump. *IFAC Proceedings Volumes*, 44(1):3102–3107.

[91] Takriti, S. and Birge, J. R. (2000). Using integer programming to refine lagrangian-based unit commitment solutions. *IEEE Transactions on power systems*, 15(1):151–156.

[92] Tassou, S., De-Lille, G., and Ge, Y. (2009). Food transport refrigeration-approaches to reduce energy consumption and environmental impacts of road transport. *Applied Thermal Engineering*, 29(8):1467–1477.

[93] Tassou, S., Lewis, J., Ge, Y., Hadawey, A., and Chaer, I. (2010). A review of emerging technologies for food refrigeration applications. *Applied Thermal Engineering*, 30(4):263–276.

[94] Wang, L. (2009). *Model predictive control system design and implementation using MATLAB*. Springer Science & Business Media.

[95] Wang, X., Castellazzi, A., and Zanchetta, P. (2014). Observer based temperature control for reduced thermal cycling in power electronic cooling. *Applied Thermal Engineering*, 64(1-2):10–18.

[96] Wen, J. and Smith, T. F. (2003). Development and validation of online parameter estimation for HVAC systems. *Journal of solar energy engineering*, 125(3):324–330.

[97] Widell, K. N. and Eikevik, T. (2010). Reducing power consumption in multi-compressor refrigeration systems. *International Journal of Refrigeration*, 33(1):88–94.

[98] Xia, Y. and Deng, S. (2016). The influences of the operating characteristics of an electronic expansion valve (EEV) on the operational stability of an EEV controlled direct expansion air conditioning system. *International Journal of Refrigeration*, 69:394–406.

[99] Yang, Z., Rasmussen, K. B., Kieu, A. T., and Izadi-Zamanabadi, R. (2011a). Fault detection and isolation for a supermarket refrigeration system-part one: Kalman-filter-based methods. *IFAC Proceedings Volumes*, 44(1):13233–13238.

[100] Yang, Z., Rasmussen, K. B., Kieu, A. T., and Izadi-Zamanabadi, R. (2011b). Fault detection and isolation for a supermarket refrigeration system-part two: Unknown-input-observer method and its extension. *IFAC Proceedings Volumes*, 44(1):4238–4243.

[101] Yarahmadi, N., Vega, A., and Jakubowicz, I. (2017). Determination of essential parameters influencing service life time of polyurethane insulation in district heating pipes. *Energy Procedia*, 116:320–323.

[102] Zavala, V. M. (2016). New architectures for hierarchical predictive control. *IFAC-PapersOnLine*, 49(7):43 – 48. 11th {IFAC} Symposium on Dynamics and Control of Process SystemsIncluding Biosystems DYCOPS-CAB 2016Trondheim, Norway, 6—8 June 2016.

[103] Zhang, F., Wu, X., and Shen, J. (2017). Extended state observer based fuzzy model predictive control for ultra-supercritical boiler-turbine unit. *Applied Thermal Engineering*, 118:90–100.

[104] Zhao, B., Guo, C., Bai, B., and Cao, Y. (2006). An improved particle swarm optimization algorithm for unit commitment. *International Journal of Electrical Power & Energy Systems*, 28(7):482–490.

[105] Zhao, D., Zhang, X., and Zhong, M. (2015). Variable evaporating temperature control strategy for VRV system under part load conditions in cooling mode. *Energy and Buildings*, 91:180–186.

[106] Zhonghai, M., Shaoping, W., Jian, S., Tongyang, L., and Xingjian, W. (2018). Fault diagnosis of an intelligent hydraulic pump based on a nonlinear unknown input observer. *Chinese Journal of Aeronautics*, 31(2):385–394.

Appendix A

Intersample bound

A conservative bound for the inter-sample deviation of each state variable $|\boldsymbol{x}_j(t) - \boldsymbol{x}_j(K)|$ can be computed by considering at the worst case: Eq. (4.40) can be evaluated for only one large input $\tilde{u}_0(m)$ at the small sampling interval m such that $u_0(k+i) = 0, \forall i \neq m$. The solution of the continuous-time state trajectory $\boldsymbol{x}(t)$ is thus given by (initial condition $\boldsymbol{x}(t_0) = \boldsymbol{x}(K)$, $t_0 \leq t < \lambda t_s$)

$$\boldsymbol{x}(k+\lambda) = \boldsymbol{\Phi}^{\lambda}\boldsymbol{x}(K) + \boldsymbol{\Gamma}_m \tilde{u}_0(k+m) + \boldsymbol{M}_{\Sigma}\boldsymbol{z}(K),$$

The constraint requires $\boldsymbol{x}(K+1) = \boldsymbol{x}(k+\lambda)$ to hold:

$$\boldsymbol{x}(K+1) = \boldsymbol{\Phi}^{\lambda}\boldsymbol{x}(K) + \boldsymbol{\Gamma}_m \tilde{u}_0(k+m) + \boldsymbol{M}_{\Sigma}\boldsymbol{z}(K),$$

and solving for $\tilde{u}_0$ yields

$$\tilde{u}_0 = \boldsymbol{\Gamma}_m^{-1}\left[\boldsymbol{x}(K+1) - \boldsymbol{\Phi}^{\lambda}\boldsymbol{x}(K) - \boldsymbol{M}_{\Sigma}\boldsymbol{z}(K)\right]. \tag{A.1}$$

Hence, (4.47) can be computed and the vector $\boldsymbol{x}_{\min}$ of extremal values of $\boldsymbol{x}(t)$ is given by element-wise evaluation of

$$\boldsymbol{x}_{j,\min} = \min \boldsymbol{x}_j(t), \quad t_0 \leq t < \lambda t_s, \tag{A.2}$$

and $\boldsymbol{\Delta}_{j,\max} = \boldsymbol{x}_j(K) - \boldsymbol{x}_{j,\min}$ is well defined. For all control sequences $u_0(k)$ of the MI-opimiser the state trajectory $\boldsymbol{x}(t)$ will stay inside the bounding box defined by $\boldsymbol{\Delta}_{j,\max}$.

Curriculum Vitae

Personal Information

Name	Dipl.-Ing. Elisabeth Luchini
Date of birth	22th of December, 1988
Birthplace	Villach (Carinthia)
Citizenship	Austria
Gender	Female
Adress	Liechtensteinstraße 121/21 1090 Vienna

Education

01/2015 - Present	Vienna University of Technology Doctoral studies in Mechanical Engineering
10/2008 - 12/2014	Vienna University of Technology Diploma studies in Mechanical Engineering Specialization in Control and Process Automation Final examination passed on December 17th, 2014
09/2003 - 06/2008	HTL Villach (secondary school) Information Technology and Network Engineering
09/1999 - 07/2003	HS 5 Landskron
09/1995 - 07/1999	VS 8 Landskron

Diploma Thesis

Title	Adaptive macroscopic traffic model with parameter identification
Supervisor	Univ.Prof. Dipl.-Ing. Dr.techn. Stefan Jakubek

Work Experience

01/2015 - Present	Project assistant at Vienna University of Technology Institute of Mechanics and Mechatronics Division of Control and Process Automation
10/2014 – 12/2014	Student assistant at Vienna University of Technology Institute of Mechanics and Mechatronics Division of Control and Process Automation
03/2014 – 07/2014	Tutor at Vienna University of Technology Institute of Mechanics and Mechatronics Division of Measurement and Actuator Technology
03/2010 – 07/2013	Tutor at Vienna University of Technology Institute of Mechanics and Mechatronics Division of Engineering Design and Logistics Engineering
02/2011, 07/2011	3M (Rappold Winterthur Technology Group) Engineering Office
07/2007 - 09/2008	Carinthia University of Applied Sciences Division of Systems Engineering
07/2006 - 09/2006	Villach State Hospital, IT department
07/2005 - 08/2005	Villach State Hospital, Secretariat Gynecology

Computer skills

Systems	Windows, macOS, Linux
Programming	Matlab/Simulink, Java, Phyton, C/C++
Office	MS Office, Latex
Networks	Cisco CCNA 1-4, CCNA Wireless

Languages

German	native language
English	fluent in written and spoken

Other education

Sports	snowsport instructor

Leisure Interests

Sports	roadbike, climbing, mountain climbing, ski touring, running

List of scientific publications

International journals

1. Jakubek, S., Luchini, E., Oberhummer, A., and Pfister, F. (2016). A model-based interfacing concept for accurate power hardware-in-the-loop systems. Mathematical and Computer Modelling of Dynamical Systems, 22(1), 1-20.

2. Thonhofer, E., Luchini, E., and Jakubek, S. (2017). A flexible, adaptive traffic network simulation with parameter estimation. Journal of Intelligent Transportation Systems, 21(1), 63-77.

3. Luchini, E., Kitanoski, F., and Kozek, M. (2017a). Multi-objective optimization of the operational modes for redundant refrigeration circuits. Applied Thermal Engineering, 122:409–419.

4. Luchini, E., Radler, D., Ritzberger, D., Jakubek, S., and Kozek, M. (2018). Model predictive temperature control and ageing estimation for an insulated cool box. Applied Thermal Engineering.

5. Luchini, E., Schirrer, A., Jakubek, S., and Kozek, M. (2018). Model predictive multirate control for mixed-integer optimisation of redundant refigeration circuits. Manuscript submitted to Journal of Process Control.

Talks and presentations on international conferences

1. Thonhofer, E., Luchini, E., Kuhn, A., and Jakubek, S. (2014). Online parameter estimation for a flexible, adaptive traffic network simulation. In Connected Vehicles and Expo (ICCVE), 2014 International Conference on (pp. 937-938). IEEE.

2. Luchini, E., Schirrer, A., and Kozek, M. (2017b). A hierarchical MPC for multiobjective mixed-integer optimisation applied to redundant refrigeration circuits. IFAC-PapersOnLine, 50:9058–9064.

3. Luchini, E. and Kozek, M. (2018). Disturbance observer and ageing estimation for a temperature controlled food transporter. In Control Systems (SICE ISCS), 2018 SICE International Symposium on. IEEE.

Patents

1. E. Luchini, M. Kozek, F. Kitanoski, F. Schilling: "Verfahren zur Regelung eines Kühlaggregats mit mehreren Kompressoren und Kühlaggregat"; Patent: Deutschland, Nr. DE102015016852; eingereicht: 23.12.2015.

2. D. Radler, F. Kitanoski, F. Schilling, F. Nittaus, A. Tonchev, E. Luchini: "Verfahren zum Regeln eines Kühlsystems"; Patent: Deutschland, Nr. DE102016005981; eingereicht: 13.05.2016.